University of Southampton Research Repository

ePrints Soton

Copyright © and Moral Rights for this thesis are retained by the author and/or other copyright owners. A copy can be downloaded for personal non-commercial research or study, without prior permission or charge. This thesis cannot be reproduced or quoted extensively from without first obtaining permission in writing from the copyright holder/s. The content must not be changed in any way or sold commercially in any format or medium without the formal permission of the copyright holders.

When referring to this work, full bibliographic details including the author, title, awarding institution and date of the thesis must be given e.g.

AUTHOR (year of submission) "Full thesis title", University of Southampton, name of the University School or Department, PhD Thesis, pagination

http://eprints.soton.ac.uk

UNIVERSITY OF SOUTHAMPTON

FACULTY OF PHYSICAL AND APPLIED SCIENCES
Optoelectronics Research Centre

Nonlinear Properties of Silicon Core Optical Fibres

by

Priyanth Mehta

Thesis for the degree of Doctor of Philosophy

April 2013

UNIVERSITY OF SOUTHAMPTON

ABSTRACT

FACULTY OF PHYSICAL AND APPLIED SCIENCES
Optoelectronics Research Centre

Doctor of Philosophy

NONLINEAR PROPERTIES OF SILICON CORE OPTICAL FIBRES

by Priyanth Mehta

Silica optical fibres are renowned for the framework they have set in modern communications systems, sensors, and biotechnology. One particular trend in current research aims to investigate materials with enhanced optical functionality, high optical efficiency, robustness, and a small device footprint. Amongst the many material choices, semiconductors are emerging as a promising route. In this work, optical fibres and semiconductors are elegantly unified to create a hybrid structure with the potential of seamless integration into current fibre infrastructures. Silica capillaries form the fibre templates in which amorphous semiconductor materials such as silicon and/or germanium are impregnated. This thesis will present the first comprehensive description of the fabrication, characterisation, and the implementation of silicon optical fibres for all-optical signal processing. The fibres are fabricated via a novel high pressure chemical deposition procedure. Each fibre is analysed to determine the exact material composition, uniformity, and more importantly the optical quality. Linear and nonlinear optical characterisations are performed experimentally and supported by intensive numerical studies to validate the results.

The high nonlinearity of silicon is exploited for all-optical signal processing. Several investigations have been performed to determine key nonlinear coefficients that were previously unknown in these fibres. Nonlinear absorption experiments allowed for the determination of the degenerate and non-degenerate two-photon absorption coefficients, free carrier cross sections, and free carrier lifetimes of a number of silicon fibres. Nonlinear refraction investigations were then used to establish the Kerr nonlinearity. The strength of this parameter allowed for demonstration of strong self-phase and cross-phase modulation effects. With the insight gained in nonlinear absorption and refraction in silicon optical fibres, all-optical amplitude modulation and wavelength switching was demonstrated at ultrafast sub-picosecond speeds.

Contents

Declaration of Authorship **xv**

Acknowledgements **xvii**

Nomenclature **xix**

1 Introduction **1**
- 1.0.1 Outline and Contributions of Thesis . . . 3

2 Background **5**
- 2.1 Introduction . . . 5
- 2.2 Wave Propagation in Optical Fibres . . . 5
  - 2.2.1 Optical Pulses . . . 6
  - 2.2.2 Modal Properties . . . 7
  - 2.2.3 Dispersion . . . 8
    - 2.2.3.1 Material Dispersion . . . 9
    - 2.2.3.2 Waveguide Dispersion . . . 10
    - 2.2.3.3 Walk-Off . . . 10
  - 2.2.4 Linear Losses . . . 11
    - 2.2.4.1 Material Absorption . . . 12
    - 2.2.4.2 Rayleigh Scattering . . . 13
- 2.3 Nonlinear Propagation . . . 13
  - 2.3.1 Nonlinear Refraction . . . 14
    - 2.3.1.1 Self-phase Modulation . . . 14
    - 2.3.1.2 Cross-phase Modulation . . . 15
  - 2.3.2 Two-Photon Absorption . . . 15
    - 2.3.2.1 Degenerate TPA . . . 17
    - 2.3.2.2 Non-Degenerate TPA . . . 18
  - 2.3.3 Free Carrier Density . . . 21
  - 2.3.4 Free Carrier Absorption . . . 21
- 2.4 Generalized Nonlinear Schrödinger Equation . . . 23

3 Semiconductor Fibre Fabrication **27**
- 3.1 Introduction . . . 27
- 3.2 History . . . 27
- 3.3 Confined High Pressure Chemical Deposition . . . 29
- 3.4 Semiconductor Fibre Preparation . . . 30
- 3.5 Material Characterisation . . . 31

3.5.1 Scanning Electron Microscopy (SEM) . . . 32
3.5.2 Raman Spectroscopy . . . 33
3.5.2.1 Polycrystalline Silicon (p-Si) . . . 34
3.5.2.2 Pure Amorphous Silicon (a-Si) . . . 34
3.5.2.3 Hydrogenated Amorphous Silicon (a-Si:H) . . . 34
3.5.3 Optical Transmission Characterisation . . . 36
3.5.3.1 Experimental Technique . . . 38
3.5.3.2 p-Si . . . 39
3.5.3.3 a-Si . . . 40
3.5.3.4 a-Si:H . . . 40
3.6 Conclusion . . . 43

4 Nonlinear Absorption and Modulation in Silicon Fibres 45
4.1 Introduction . . . 45
4.2 Nonlinear Absorption Mechanisms . . . 45
4.3 Carrier Lifetimes . . . 47
4.3.1 Dynamics . . . 47
4.3.2 Measurements . . . 49
4.4 Simplified Coupled-Mode Equations . . . 53
4.5 Nonlinear Absorption Strength and Cross-Sections . . . 54
4.6 All-Optical Modulation . . . 59
4.6.1 Continuous Wave Cross-Absorption Modulation (CW XAM) . . . 60
4.6.2 Pump-Probe Technique . . . 61
4.6.3 Non-Degenerate XAM . . . 65
4.7 Conclusion . . . 68

5 Nonlinear Refraction in Silicon Fibres 69
5.1 Introduction . . . 69
5.2 Self-Phase Modulation . . . 69
5.2.1 Characterising n_2 . . . 71
5.2.1.1 Technique . . . 71
5.2.1.2 Measurements . . . 73
5.2.2 Figure of Merit . . . 77
5.3 Cross-Phase Modulation . . . 78
5.3.1 Coupled-Mode Extended NLSE . . . 79
5.3.2 Long Pulse Regime . . . 81
5.3.2.1 Spectral Modulation . . . 82
5.3.3 Short Pulse Regime . . . 84
5.3.3.1 Frequency Shifting . . . 86
5.3.3.2 Frequency Depletion . . . 88
5.4 Conclusion . . . 89

6 Towards Mid-Infrared Applications 91
6.1 Introduction . . . 91
6.2 Motivation . . . 91
6.2.1 Silicon . . . 92
6.2.2 Germanium . . . 93

6.3 Silicon Optical Fibres . . . 95
6.4 Germanium Optical Fibres . . . 96
    6.4.1 Fabrication . . . 96
    6.4.2 Material Characterisation . . . 97
    6.4.3 Mid-Infrared Transmission . . . 97
6.5 Conclusion . . . 100

7 Conclusions 101

A Non-Degenerate TPA Solution 105

B Free Carrier Density Rate Equation 107

List of Publications 109

References 111

List of Figures

1.1 Illustration of a semiconductor-core silica-cladding optical fibre as an integrable nonlinear component. 2

2.1 Cross-section of a step-index optical fibre. 6
2.2 (a) Dispersion contributions for a 400nm core silicon fibre. (b) Effect of dispersion on core diameter in a silicon fibre. 11
2.3 Density of states for (a) single crystal and (b) amorphous semiconductors from [29]. 12
2.4 (a) Two-photon absorption. (b) Free carrier absorption. 16
2.5 (a) Effects of optical limiting due to degenerate TPA. (b) Degenerate TPA on a 700 fs pulse. 18
2.6 (a) Effects of a CW pump on a CW signal wave through non-degenerate TPA showing gradual depletion of the signal's output power. (b) Non-degenerate TPA with a 700 fs pump pulse on a CW signal as a function of interaction length. The signal depletes with a trend following the pump pulse. 20
2.7 (a) Nonlinear absorption on a CW field. (b) Temporal effects of FCA and TPA on a 700 fs Gaussian pulse. Dashed line indicates the drift in the pulse centre due to pulse shaping through TPA and FCA. 22

3.1 Cross-sectional view of deposition procedure. 29
3.2 Influence of furnace temperature on the deposited semiconductor's material phase and deposition time for complete filling of a 6 μm core. 30
3.3 (Left) Transverse plane cross-section of a mounted semiconductor fibre; scale bar is 100 μm. (Right) Longitudinal plane of fibre. 31
3.4 Evolution of deposition filling of a 6 μm core silicon fibre as a function of temperature taken for the same deposition time. Imaged using an SEM. . 32
3.5 Terminology for vibrational displacements of atoms used in Raman spectroscopy from [94]. 33
3.6 (a) Raman spectra of p-Si at different annealing temperatures from [99]. (b) Raman spectra of a-Si. 35
3.7 (a) Raman spectra of Si-H (black at 390 °C) and inclusion of Si-H_2 (blue at 340 °C) stretch modes in a-Si:H fibres. (b) Evolution of Si-H modes with deposition temperature. 36
3.8 (a) Fundamental loss contributions to semiconductor fibres. Hatched region represents wavelengths over which defect based absorption (such as dangling bonds) affect the most. (b) CCD image of defected core material taken using a downward facing infrared camera onto the sample. 37

3.9 (a) Schematic for loss measurements. (b) Variables of the cut-back technique. . . . 39
3.10 (a) Cut-back loss performed on three p-Si fibres from [99]. (b) Cut-back measurement of a p-Si fibre annealed for a shorter duration. . . . 39
3.11 Deposition furnace's temperature profiles constructed at Pennsylvania State University. . . . 41
3.12 (a) Evolution of a-Si:H fibre losses since the start of this work. (b) Comparison of two low loss a-Si:H fibres obeying an Urbach and Rayleigh trend. . . . 42

4.1 (a) Energy level diagrams for degenerate TPA, non-degenerate TPA, FCA, and MPA (b) Predicted nonlinear absorption strength of TPA and FCA. . . . 46
4.2 Energy-momentum band diagrams showing carrier dynamics. CB is conduction band, VB is valence band. (a) Photo-excitation of a carrier. (b) Thermalisation. (c) Auger recombination. (d) Shockley-Read-Hall recombination. . . . 48
4.3 Modulation experiment employed by Won *et al.* [122] . . . 50
4.4 (a) XAM experiment for the measurements of the carrier lifetimes. (b) Free carrier absorbed probe pulses as viewed on an oscilloscope. . . . 51
4.5 Measured carrier lifetimes for fibres described by their *Sample-Type/Carrier Core-Diameter Max-Deposition-Temperature*: (a) a-Si/He 6 μm 500 °C, (b) a-Si:H/He 6 μm 400 °C, (c) a-Si:H/H_2 6 μm 384 °C, (d) a-Si:H/H_2 2 μm 372 °C. (e) Lifetimes and fibre loss relation. . . . 52
4.6 (a) Raw spectrogram of pump source. (b) Recovered temporal pulse and phase of pump. . . . 55
4.7 Fibre A. (a) Nonlinear absorption. (b) Carrier density. . . . 57
4.8 Nonlinear absorption in (a) Fibre B and (b) Fibre C. . . . 58
4.9 Fibre D. (a) Nonlinear absorption. (b) Carrier density. . . . 58
4.10 (a) Pump and probe pulses from the first XAM experiment. (b) Variation of probe modulation as a function of pump power showing a nonlinear decrease. . . . 61
4.11 (a) Autocorrelation simulation of two secant hyperbolic pulses. (b) Experimental autocorrelation traces of the two secant hyperbolic pulses. . . . 62
4.12 (a) Pump-probe experiment for degenerate TPA based modulation. (ODL) Optical delay line, (CH) chopper, (AC) autocorrelator, (OSC) oscilloscope, (PD) photodetector, (LA) lock-in amplifier, (FD) frequency driver. (b) Recorded absorption on pump (circles) with numerical fit (solid line) from pre-established parameters. . . . 63
4.13 (a) Probe pulse drift and decoupling with decreasing temperature. (b) Probe pulse drift after 10 mins in a regulated temperature environment. (c) Probe pulse after 30 mins in a thermally isolated container. . . . 66
4.14 (a) Continuum produced from the HNLF. (b) Filtered probe pulse using a bandwidth-tunable variable filter. . . . 67
4.15 (a) Non-degenerate pump-probe XAM experiment layout. (b) Probe modulation as a function of pump power. . . . 67

5.1 (a) Nonlinear phase shift for three sech^2 pulses. (b) Induced frequency change as a result of the nonlinear phase. . . . 70

5.2 (a) Effective index of circularly symmetric modes and respective group delay. (b) Multimode (blue) and Fabry-Perot (red) interference in a a-Si:H fibre. . . . 72
5.3 Power dependent SPM spectra of fibres A, B, and C (green) with numerical fits (blue). . . . 74
5.4 Power dependent SPM spectra of fibre D (green) with numerical fit (blue). 75
5.5 Highest power SPM spectra showing numerical fits (red) in the absence of FCA only. . . . 76
5.6 (a) XPM induced nonlinear phase shift on pump $\phi_{NL,1}$ at 1540 nm and probe $\phi_{NL,2}$ at 1590 nm. (b) XPM-induced frequency change as a result of the induced nonlinear phases. . . . 79
5.7 (a) Experiment for the observation of XPM in the long pulse regime. Solid lines are optical paths, broken lines are electronic cables. $\Delta\mathrm{t} = \tau_d$ is the delay between the pulse centres. (b) Recovered FROG trace of the probe pulse's intensity and phase profile. Inset shows the recorded spectrogram. 81
5.8 Experimental temporal evolution of XPM on the 3 ps probe pulse (red) together with the simulation results (blue). A peak pump power of 300 W was used, and the probe power was limited to 1 W. Fibre parameters are in Table 5.4. . . . 82
5.9 (a) Experimentally measured spectrogram of the XPM process on the probe pulse recorded over a 12 ps time window. (b) Trace of peak wavelength through the spectrogram indicating no shift in the central wavelength. 83
5.10 (a) Experiment for the observation of XPM using femtosecond probe pulses. The BPF has a 12 nm bandwidth ensuring sub-picosecond pulses from the HNLF. $\Delta\mathrm{t}$ is again represented as τ_d. (b) Recovered FROG trace from 1587 nm filtered HNLF showing the intensity (blue) and phase (green) profile of the probe. Spectrogram from FROG shown as an inset. 84
5.11 Temporal evolution from negative to positive time delays of the XPM process using an 800 fs probe pulse. Spectral modulation and wavelength shifting is significantly more pronounced. . . . 85
5.12 (a) Recorded spectrogram of the short pulse XPM process. (b) Measured (blue) and numerically fitted (red) peak wavelength shift of the sub-picosecond probe pulse. . . . 86
5.13 (a) Integral of the frequency change to obtain the nonlinear phase shift. (b) Contributions of the Kerr and free carrier induced refractive index changes. . . . 88
5.14 (a) Probe spectrum at the output of the a-Si:H fibre in the absence of the pump pulse (i.e., no XPM). (b) Largest red and blue shifts observed from the XPM process. Grey line indicates original centre of probe pulse. Extinction ratios are calculated with respect to the original probe's centre wavelength. . . . 89

6.1 (a) Transmission profiles of silicon, germanium, and silica. (b) Material nonlinearities from [11]. . . . 92
6.2 Dispersion of nonlinearities in single crystal silicon by Q. Lin *et al.* [116]. The blue squares are experimental measurements and the solid blacks lines are theoretical trends. (a) TPA dispersion. (b) Kerr nonlinearity dispersion. (c) FOM_{NL} dispersion. . . . 93

6.3 Dispersion of nonlinearities in single crystal germanium. (a) TPA dispersion from [185, 188]. (b) Kerr nonlinearity dispersion gathered from [185, 189–191]. (c) Theoretical FOM$_{NL}$ dispersion. 94

6.4 a-Si:H MIR loss results and measured output mode images. Green lines represent Rayleigh fitting to the NIR and MIR loss measurements. 96

6.5 (a) SEM of a 6 μm germanium core; scale bar is 2 μm. (b) Microscope images of a 6 μm and 30 μm (inset) germanium core; both scale bars are 20 μm. (c) Raman spectra of a-Ge:H 97

6.6 Experimental layout for transmission measurements of the germanium core fibre. Output mode image has a scale bar of 4 μm. (Source) is either a CO_2 laser, HeNe laser, or the Radiantis OPIUM OPO, (FD) Frequency driver, (CH) chopper, (CAM) camera, (PD) photodetector. 98

6.7 Linear transmission loss for (a) 6 μm core diameter a-Ge:H fibre, and (b) 30 μm core diameter a-Ge:H fibre. 99

List of Tables

2.1 Sellmeier coefficients for crystalline silicon from [24, 26]. 10
2.2 Sellmeier coefficients for crystalline germanium from [24, 26]. 10

3.1 Fabricated 6 μm core a-Si:H fibres 41
3.2 Fabricated 2 μm core a-Si:H fibres 42

4.1 a-Si:H fibre specifications. 56
4.2 Nonlinear absorption coefficients measured for the a-Si:H fibres. 59
4.3 Highly nonlinear fibre properties characterised at 1550 nm. 65

5.1 a-Si:H fibres characterised for Kerr nonlinearity. 73
5.2 Kerr coefficients for several a-Si:H fibres characterised at $\lambda = 1.54\,\mu$m using numerical fitting of the experimental SPM spectra. 75
5.3 Comparison of FOM$_{NL}$ for different materials. 78
5.4 Simulation parameters used in the coupled-mode equations to obtain the closest spectral modulation of XPM to the picosecond probe pulses. The time frame is normalised to the pump (p) so that the dispersion term $\Delta\beta_1 = \beta_{1s} - \beta_{1p}$. 83
5.5 Simulation parameters used in the coupled-mode equations to obtain the closest XPM-induced frequency shift relative to the experimentally measured shift. 87

Declaration of Authorship

I, Priyanth Mehta , declare that the thesis entitled *Nonlinear Properties of Silicon Core Optical Fibres* and the work presented in the thesis are both my own, and have been generated by me as the result of my own original research. I confirm that:

- this work was done wholly or mainly while in candidature for a research degree at this University;
- where any part of this thesis has previously been submitted for a degree or any other qualification at this University or any other institution, this has been clearly stated;
- where I have consulted the published work of others, this is always clearly attributed;
- where I have quoted from the work of others, the source is always given. With the exception of such quotations, this thesis is entirely my own work;
- I have acknowledged all main sources of help;
- where the thesis is based on work done by myself jointly with others, I have made clear exactly what was done by others and what I have contributed myself;
- parts of this work have been published as: [See List of Publications]

Signed:...

Date:...

Acknowledgements

To the invaluable contributions of,

Anna Peacock
Pier Sazio
Peter Horak
Alex Heidt
James Gates
Simon Butler
Natasha Vukovic
Luis Vazquez-Zuniga
Víctor Rancaño
Justin Sparks
Neil Baril
Noel Healy
Radan Slavík
Shaif-ul Alam
Regan Watts
Francesca Parmigiani
Jamie Cook
Li Shen
Jae Daniel
Todd Day
Mahesh Krishnamurthi
John Badding

Thank you.

Priyanth Mehta
April 2013
Southampton
United Kingdom.

Nomenclature

a-Si	Amorphous Silicon
a-Si:H	Hydrogenated Amorphous Silicon
c-Si	Crystalline Silicon
p-Si	Poly-Crystalline Silicon
CW	Continuous Wave
FCA	Free Carrier Absorption
FCD	Free Carrier Dispersion
FOM	Figure of Merit
FROG	Frequency-Resolved Optical Gating
FWHM	Full-Width at Half Maximum
GNLSE	Generalized Nonlinear Schrödinger Equation
GVD	Group-Velocity Dispersion
HNLF	Highly Nonlinear Fibre
HPCD	High Pressure Chemical Deposition
LA	Lock-In Amplifier
MIR	Mid-Infrared
MMI	Multimode Interference
MPA	Multiphoton Absorption
NIR	Near-Infrared
NLSE	Nonlinear Schrödinger Equation
ODL	Optical Delay Line
OPO	Optical Parametric Oscillator
OSA	Optical Spectrum Analyser
OSC	Oscilloscope
PCF	Photonic Crystal Fibre
PD	Photodetector
PECVD	Plasma Enhanced Chemical Vapour Deposition
PhC	Photonic Crystal
RF	Radio Frequency
RMS	Root Mean Square
RSA	Reverse Saturable Absorption
SEM	Scanning Electron Microscope

SMF	Single-Mode Fibre
SPM	Self-Phase Modulation
SRH	Shockley-Read-Hall
TBP	Time-Bandwidth Product
TPA	Two-Photon Absorption
XAM	Cross-Absorption Modulation
XPM	Cross-Phase Modulation
ZDW	Zero-Dispersion Wavelength

Chapter 1

Introduction

Exotic Fibres

Optical fibres have experienced significant advancements in their performance since the 1950s. After the first commercial and industrial implementation of solid silica fibres in 1975 [1], transmission was employed over long and short distances, revolutionising communications, remote sensing, imaging, laser development, and many more disciplines. Despite this success, limitations in conventional silica fibres began to appear. In recent years, considerable attention has been focussed on expanding the functionality of optical fibres beyond what is offered by conventional silica fibres. The development of fibre compositions to include more exotic materials such as soft glasses [2, 3], polymers [4], gases [5], liquid crystals [6], metals [7], and semiconductors [8] have inspired a new generation of research. The design of such novel fibres can lead to an unprecedented level of control in their dispersion, birefringence, number of guided modes, nonlinearity and many other properties. Consequently, fundamental characterisations of such novel fibres must be performed to determine their potential as well as to rank them against competing technologies.

The past decade has witnessed a particular design emerging in optical fibres. Hybridised structures that exploit the excellent mechanical properties of the silica material as a cladding in which to encapsulate a uniquely different core material, thus providing an elegant route at unifying current optical fibres with novel materials. The prospect of such a platform is largely motivated by the effects it has on optical pulse propagation. Much of this research is motivated by the desire for enhanced nonlinear optical effects. Nonlinear optics has been an active area of research for over 40 years. It is well known by the telecommunication industry as a system impairment, however, it has richly contributed to many fields of physics, medicine, biology, and chemistry. While fundamental nonlinear interactions have been well characterised in many materials, there is a persistent trend to search for materials with an enhanced nonlinearity.

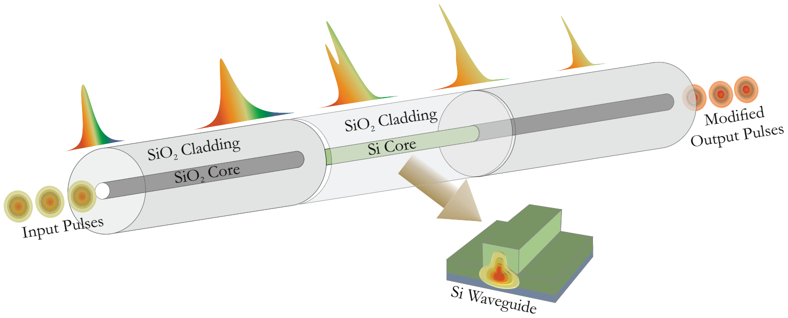

Figure 1.1: Illustration of a semiconductor-core silica-cladding optical fibre as an integrable nonlinear component.

Ultrafast Effects

Nonlinear optics in silica fibres received a large stimulus after the work of Stolen *et al.* at Bell Laboratories from the 1970s [9]. Its importance is largely motivated by the ability of the nonlinearity to manipulate light and hence the information carried by it. Due to the fast electronic response of materials, the speed at which this manipulation occurs is well beyond any electronics. However, employing this enormous bandwidth turns into a problem if conventional electronics is required to interface with this optical processing, as the electronic bandwidths are typically no better than $\sim 10^{11}$ Hz. Since the practical utilisation of nonlinear processes in most cases relies on high intensity light, it is most often investigated through the use of short pulse propagation due to their high peak powers.

Unlike bulk materials, fibres allow light to remain confined in the core due to waveguiding, providing a relatively long length over which high intensity light can be maintained. By utilising a medium in which the optical nonlinearity is far higher than silica, it is possible to use low power continuous wave or pulsed sources over shorter fibre lengths. Of the many materials listed earlier, semiconductors are well known to possess some of the highest nonlinear strengths [10, 11]. Silicon has emerged as a popular semiconductor photonics material as it has rich electrical and optical functionality and is compatible with the deeply embedded CMOS industry [12], which is also interested in combining new optical functionalities. Over the past few years silicon waveguides have been extensively investigated on planar substrates where their nonlinear applicability for all-optical modulation, switching, regeneration, amplification, pulse compression, and wavelength conversion have been demonstrated [13]. This diverse range of applications could potentially be conducted in silicon-core silica-cladding fibres. Thus, these two independent subjects of nonlinear fibre optics and nonlinear silicon photonics can be unified as depicted in Figure 1.1, to introduce a nascent route of an unexplored territory in nonlinear optical effects. A novel fabrication method is required to synthesize such a hybrid structure and accordingly requires a thorough investigation of its material composition, purity, optical characteristics, and nonlinear optical properties. Features such as this reveal a standard of measure of the silicon fibre relative to the more conventional planar silicon photonic platform. The integration of silicon as a core material encased by a silica capillary and the aforementioned characterisations is the focus of this research. This work represents the first comprehensive study of the linear and nonlinear optical properties of the silicon fibre. Linear measurements were performed at near-infrared and mid-infrared wavelengths, while the nonlinear coefficients were established at a high accuracy and justified by device applications.

1.0.1 Outline and Contributions of Thesis

Chapter 2 is a brief description of the basic properties of optical fibres. It begins by developing the theory of mode propagation for optical pulses, with particular emphasis on dispersion. The theory is then extended to fibres where the core is comprised of a semiconductor material, accounting for effects of free carrier losses and nonlinear two-photon losses. In addition, the foundation of nonlinear pulse propagation is introduced stating the primary coefficients and equations used throughout this work.
Simulations of the dispersion curves and nonlinear absorption mechanisms were performed on codes I had developed based on the theory in this background chapter.

Chapter 3 describes the chemical deposition technique used to fabricate the semiconductor fibres. The different phases of silicon: polycrystalline, amorphous, and amorphous hydrogenated, were characterised with a variety of instruments. Scanning electron microscopes and Raman spectroscopy measurements were performed on a number of samples to reveal the deposition uniformity and composition. The optical quality of several semiconductor fibres were measured and compared against the different deposited phases. Particular emphasis is placed on hydrogenated amorphous silicon core fibres.
Fabrication of the semiconductor fibres, scanning electron microscope images, Raman measurements of the Si-H stretch modes, and furnace temperature profiles in this chapter were performed at Pennsylvania State University by Todd Day and Justin Sparks. The optical microscope images, the amorphous hydrogenated silicon Raman measurements, and optical transmission measurements were performed by myself. Parts of the polycrystalline Raman measurements and transmission measurements were performed by Noel Healy and Laura Lagonigro.

Chapter 4 provides comprehensive numerical and experimental detail of the nonlinear absorption in silicon optical fibres. The chapter begins with an experimental investigation of the free carrier lifetimes. Rate equations that define the generation and recombination of these free carriers are simulated in conjunction with pulse propagation to show optical limiting. Through numerical fitting of these equations with the experimentally fitted data, the nonlinear absorption coefficients are evaluated.
In this chapter, I had redeveloped the carrier lifetime experiment based on a previous implementation by our group. Design of the experiments and the measurements of

the carrier lifetimes, FROG traces, nonlinear absorption curves, autocorrelations, oscilloscope traces, and cross-absorption modulation measurements were performed by me with the assistance of Noel Healy. Simulations of the simplified coupled-mode equations were coded by me including the evaluation of the nonlinear absorption coefficients.

Chapter 5 is dedicated to the nonlinear refraction in silicon fibres. It begins by describing how the nonlinear induced phase shift leads to frequency generation about the input pulse spectrum with a simple analytical formulation, and then shows how the Kerr nonlinearity is determined from the self-phase modulated spectrum. Cross-phase modulation is also investigated and shown to produce large frequency shifting through the interaction of ultrashort optical pulses.

Measurements of the multimode interference spectrum, self-phase modulation spectra, FROG traces, and cross-phase modulation spectra were measured by myself. I had designed the cross-phase modulation experiments based on previous literature on the subject. The computer programs written to allow for automation of the experiment was also developed by myself. Numerical analysis of the effective refractive indices and nonlinear refraction experiments were jointly done by Anna Peacock and I. The MATLAB code of the generalized nonlinear Schrödinger equations were written by Anna Peacock.

Chapter 6 extends the characterisation of the semiconductor fibres into the mid-infrared. Silicon and germanium fibres are optically characterised at these wavelengths to reveal their linear transmission losses. Emphasis is directed towards the fabrication and material characterisation of the germanium core optical fibre for future work at larger wavelengths.

The mid-infrared measurements in the hydrogenated amorphous silicon fibres were done by me with the assistance of Noel Healy. Fabrication, scanning electron microscope images, Raman spectra, and transmission measurements above a wavelength of 3 μm in the hydrogenated amorphous germanium fibres were done by Mahesh Krishnamurthi, Neil Baril, and Justin Sparks at Pennsylvania State University. The remaining experimental setups and measurements (unless otherwise stated) were designed and performed by me.

Chapter 7 concludes the results achieved in this thesis. Semiconductor fibre fabrication, linear optical characterisations, nonlinear absorption measurements, and nonlinear refraction measurements were the key topics discussed. Their relevance in device based applications is mentioned with suggested improvements still required in certain areas.

Chapter 2

Background

2.1 Introduction

In this chapter, a review of wave propagation in optical fibres is discussed. Light propagation in waveguides is strongly influenced by their geometry and material composition. A theoretical foundation and description of these properties is discussed for semiconductor core fibres, with an emphasis on silicon as a core material. Optical pulses are described for weak and strong optical intensities. In the regime of weak optical intensities, propagation of waves involve effects such as dispersion and attenuation. However, for higher optical intensities it will be shown that a number of effects arise, producing a complex model requiring numerical methods for the calculation of the output field's properties. The chapter concludes with a brief description of numerically evaluating the output optical field of a fibre using a model accounting for both weak and strong input intensity regimes.

2.2 Wave Propagation in Optical Fibres

Conventional optical fibres consist of a cylindrical core, a surrounding cladding, and jacket layers. The core has a higher refractive index than the cladding to ensure light can be guided in the core via total internal reflection. The cladding is encased by an acrylate polymer (the jacket) to blanket the surface from external particle contamination, moisture, and provide general mechanical protection. Figure 2.1 shows a schematic of a *stepped-index* optical fibre cross-section and the corresponding refractive index profile, illustrating the different layers and parameters used to quantify properties of the structure. The two dimensionless quantities n_1 and n_2 in Figure 2.1 are the refractive indices of the core and cladding and are used to characterise the light-gathering capacity

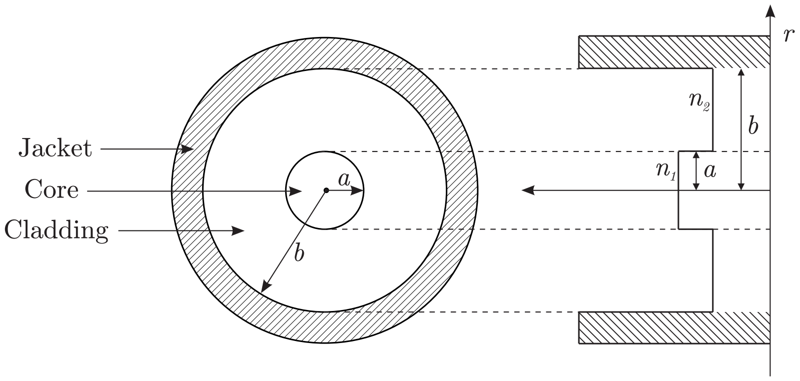

Figure 2.1: Cross-section of a step-index optical fibre.

of an optical fibre, known as the *Numerical Aperture NA*:

$$NA = \sqrt{n_1^2 - n_2^2}. \tag{2.1}$$

Large NA fibres have a higher acceptance cone in which several light rays can be captured within the core. These rays form a group of electromagnetic field distributions known as fibre modes, the number of allowable modes is determined by the V parameter or normalised frequency:

$$V = \frac{2\pi}{\lambda} a \left(n_1^2 - n_2^2\right)^{\frac{1}{2}}. \tag{2.2}$$

For step-index fibres with $V < 2.405$ [14] the energy of an input ray within the area of spatial acceptance is confined to a single-mode. Typically the core's dimension or refractive index is modified for this condition to be satisfied at a particular set of wavelengths.

2.2.1 Optical Pulses

When pulsed light enters an optical fibre a number of physical mechanisms affect its propagation. To understand these effects, a description of optical pulses is required. The scalar approach is a simplified treatment of the electric field vector by only considering a single polarization component along the fibre. This approximation holds valid for fibres whereby each polarization experiences a near similar refractive index, e.g. when the core and cladding refractive have a low index contrast [14]. The associated description of the field $\Psi(\mathbf{r}, t)$ [W$^{1/2}$] (normalised such that $|\Psi(\mathbf{r}, t)|^2$ is the optical power) can be represented as:

$$\Psi(\mathbf{r}, t) = \frac{1}{2}\hat{x}\left[\psi(\mathbf{r}, t)\exp(-i\omega_0 t) + \text{c.c.}\right], \tag{2.3}$$

$\hat{x}$ is the polarization unit vector, $\psi(\mathbf{r}, t)$ is the complex envelope, ω_0 [rads^{-1}] is the carrier frequency, and c.c. denotes the complex conjugate. The optical field is defined within the complex field envelope decomposed into an amplitude and phase component:

$$\psi(\mathbf{r}, t) = F(x, y)A(z, t)\exp[i\beta(\omega_0)z]. \tag{2.4}$$

$F(x,y)$ is the transverse mode distribution; it is an m^{th}-order Bessel solution of the wave equation [15,16] and consists of n guided mode solutions depending on fibre dimensions, geometry, and refractive indices. $A(z,t)$ [$\mathrm{W}^{1/2}$] is the slowly varying temporal pulse envelope, its solution as a function of fibre propagation distance z [m] is solved through the pulse propagation equation introduced later in Section 2.4. The exponential term represents the phase component of the optical pulse with $\beta(\omega_0)$ [m^{-1}] the momentum wavenumber solved for the modes of $F(x,y)$.

Typical forms of the optical field $A(z,t)$ may be expressed as a Gaussian envelope with phase $\phi(t)$ [rad]:

$$A(z,t) = \sqrt{P_0(z)}\exp\left(-\frac{t^2}{2T_0^2}\right)\exp[i\phi(t)], \tag{2.5}$$

where $P_0(z)$ [W] is the peak optical power and the full width half maximum (FWHM) pulse is related by $T_{\text{FWHM}} \sim 1.665T_0$ [s]. Alternatively, $A(z,t)$ may also be expressed as a hyperbolic secant:

$$A(z,t) = \sqrt{P_0(z)}\,\mathrm{sech}\left(\frac{t}{T_0}\right)\exp[i\phi(t)], \tag{2.6}$$

with $T_{\text{FWHM}} \sim 1.763T_0$. For Gaussian and hyperbolic secant pulses, the time dependence of the phase implies an instantaneous frequency change Ω across the optical pulse and is defined as $\Omega = -d\phi/dt$. The temporal optical field can also conveniently be expressed in the frequency domain through the Fourier transform $\mathcal{F}\{A(z,t)\}$:

$$\tilde{A}(z,\omega) = \int_{-\infty}^{\infty} A(z,t)\exp(i\omega t)dt. \tag{2.7}$$

When both temporal amplitude and phase of the optical pulse is known, the Fourier transform presents an accurate representation of the optical spectrum. The field can similarly be transformed back to the time domain through the inverse Fourier transform $\mathcal{F}^{-1}\left\{\tilde{A}(z,\omega)\right\}$:

$$A(z,t) = \frac{1}{2\pi}\int_{-\infty}^{\infty} \tilde{A}(z,\omega)\exp(-i\omega t)d\omega. \tag{2.8}$$

2.2.2 Modal Properties

Large values of V resulting from high index contrasts, short wavelengths, or large cores, lead to several propagating modes [17]. Each mode has a unique set of propagation properties defined by their effective refractive index and mode area. The effective index is defined as:

$$n_{\text{eff}} = \frac{\beta_{mn}(\omega_0)}{k_0}, \tag{2.9}$$

where the momentum wavenumber $\beta_{mn}(\omega_0)$ [m^{-1}] is $\beta(\omega_0)$ solved for the different modes $F(x,y)$, and $k_0 = 2\pi/\lambda_0$, with λ_0 the wavelength in vacuum. The effective mode area is defined as:

$$A_{\text{eff}} = \frac{\left[\int\int_{-\infty}^{\infty} |F(x,y)|^2 dxdy\right]^2}{\int\int_{-\infty}^{\infty} |F(x,y)|^4 dxdy}. \tag{2.10}$$

Fibre modes are characterised by the dominance of either electric EH_{mn} or magnetic field HE_{mn} components. When the index contrast $\Delta = n_1 - n_2$ is sufficiently low ($\Delta < 10^{-3}$ [18]) as is the case for conventional silica fibres, sets of these modes have degenerate effective indices and can thus be linearly combined with a superposition of EH and HE modes. The resulting linearly polarised LP_{mn} modes have degenerate polarizations states. In silicon optical fibres of the same physical dimensions as the silica fibres, Δ is greater than one and only the HE_{1n} modes exist with degenerate polarization states, thereby resembling LP_{0n} modes [19]. It is thus common to express certain high order modes as their LP_{0n} counterparts. However, for fibre dimensions with a reduced core size and $\Delta > 1$, degeneracy in the polarization states is no longer true and a full vectorial interpretation is required [20, 21] for the propagating modes.

Low Δ fibres are typically single-moded ($V < 2.405$). The fundamental mode that propagates is known as the HE_{11} or LP_{01}. High Δ fibres such as the silicon optical fibre, has a normalised frequency $V > 60$ supporting multiple EH and HE modes. Each mode propagates with a different velocity causing intermodal interference effects and a disparity in arrival time of the individual modes.

2.2.3 Dispersion

During the propagation of electromagnetic waves through waveguides or bulk media, the wave experiences a frequency-dependent phase shift manifested through the refractive index $n(\omega)$. This frequency dependence becomes significant in temporally short pulses as their frequency components travel at different velocities, causing pulse broadening, signal degradation, and bandwidth reduction. For optical pulses, the overall dispersion is known as the group velocity dispersion (GVD). In single-mode fibres (SMF) the GVD is comprised of material dispersion where the wavelength dependence on the refractive index is largely influenced by the fibre's core composition, and waveguide dispersion, where the effective refractive index is determined by the fibre's geometry and dimensions [22].

Mathematically, a mode's wavenumber $\beta(\omega_0)$ may be expressed as a Taylor Series expansion about the carrier ω_0 provided $\Delta\omega \ll \omega_0$, where $\Delta\omega$ is the spectral width. This is the quasi-monochromatic approximation [15]. The expansion is:

$$\beta(\omega_0) = \beta_0 + (\omega - \omega_0)\beta_1 + \frac{1}{2}(\omega - \omega_0)^2\beta_2 + \frac{1}{6}(\omega - \omega_0)^3\beta_3 + \dots \tag{2.11}$$

where

$$\beta_m = \left(\frac{d^m\beta}{d\omega^m}\right)_{\omega=\omega_0} \quad (m = 0, 1, 2, \ldots). \tag{2.12}$$

From this expansion, the first β_1 [s/m] and second order β_2 [s^2/m] dispersion coefficients are sufficient for calculating the total dispersion of small $\Delta\omega$ pulses:

$$\beta_1 = \frac{1}{v_g} = \frac{1}{c}\left(n + \omega\frac{dn}{d\omega}\right), \tag{2.13}$$

$$\beta_2 = \frac{1}{c}\left(2\frac{dn}{d\omega} + \omega^2\frac{d^2n}{d\omega^2}\right). \tag{2.14}$$

The velocity at which the envelope of the pulse propagates is known as the group velocity v_g. Since β_1 is related to v_g, the different spectral components of a pulse propagate at different velocities, causing the pulse to spread in time. Thus the refractive index a pulse experiences is the group index ($n_g = c/v_g$) and the inverse rate at which the pulse spreads (or disperses) is referred to as the GVD parameter β_2. If $\beta_2 < 0$ then blue-shifted wavelengths travel faster than red-shifted wavelengths. This is the anomalous dispersion regime. Similarly red-shifted wavelengths travel faster than blue-shifted wavelengths when $\beta_2 > 0$. This is the normal dispersion regime [23]. When $\beta_2 = 0$ this is the *zero-dispersion wavelength* (ZDW) and higher order terms from the Taylor expansion (e.g. $m = 3$ and 4) are required to calculate the exact dispersion at this point.

2.2.3.1 Material Dispersion

The material based contribution to dispersion can be accurately determined by its wavelength dependent refractive index through the Sellmeier equation [24]:

$$n^2(\lambda, T) - 1 = \sum_{i=1}^{m} \frac{S_i(T)\lambda^2}{\lambda^2 - \lambda_i^2(T)}, \tag{2.15}$$

where

$$S_i(T) = \sum_{j=0}^{4} S_{ij}T^j, \tag{2.16}$$

$$\lambda_i(T) = \sum_{j=0}^{4} \lambda_{ij}T^j. \tag{2.17}$$

Parameters $S_i(T)$ and $\lambda_i(T)$ are obtained by fitting experimentally measured refractive indices at different wavelengths λ [μm] and temperatures T [K]. The first two parameters (S_i and λ_i) represent the oscillation strength (dimensionless) and resonant frequency of the material, respectively [25]. The Sellmeier formulism provides all the information required to establish the wavelength dependent refractive index of a material. The

Parameter	S_1	S_2	S_3	λ_1	λ_2	λ_3
T_0	10.4907	-1346.61	4.42827×10^{7}	0.299713	-3.51710×10^{3}	1.714×10^{6}
T_1	-2.0802×10^{-4}	29.1664	-1.76213×10^{6}	-1.14234×10^{-5}	42.3892	-1.44984×10^{5}
T_2	4.21694×10^{-6}	-0.278724	-7.61575×10^{4}	1.67134×10^{-7}	-0.357957	-6.90744×10^{3}
T_3	-5.82298×10^{-9}	1.05939×10^{-3}	678.414	-2.51049×10^{-10}	1.17504×10^{-3}	-39.3699
T_4	3.44688×10^{-12}	-1.35089×10^{-6}	103.243	2.32484×10^{-14}	-1.13212×10^{-6}	23.5770

Table 2.1: Sellmeier coefficients for crystalline silicon from [24, 26].

Parameter	S_1	S_2	S_3	λ_1	λ_2	λ_3
T_0	13.9723	0.452096	751.447	0.386367	1.08843	-2893.19
T_1	2.52809×10^{-3}	-3.09197×10^{-3}	-14.2843	2.01871×10^{-4}	1.16510×10^{-3}	-0.967948
T_2	-5.02195×10^{-6}	2.16895×10^{-5}	-0.238093	-5.93448×10^{-7}	-4.97284×10^{-6}	-0.527016
T_3	2.22604×10^{-8}	-6.02290×10^{-8}	2.96047×10^{-3}	-2.27923×10^{-10}	1.12357×10^{-8}	6.49364×10^{-3}
T_4	-4.86238×10^{-12}	4.12038×10^{-11}	-7.73454×10^{-6}	5.37423×10^{-12}	9.40201×10^{-12}	-1.95162×10^{-5}

Table 2.2: Sellmeier coefficients for crystalline germanium from [24, 26].

corresponding coefficients for the two semiconductors that are dealt with in this thesis (silicon and germanium) are presented in Table 2.1 and 2.2.

2.2.3.2 Waveguide Dispersion

In step-index fibres, smaller wavelengths of arbitrary transverse distribution will be more tightly confined in the core. Larger wavelengths will have a broadened distribution and thus be less confined. This dependence of field distribution on wavelength leads to a perturbation in the effective refractive index, thereby modifying β.

Exact calculations of β are determined by numerically solving the spatial solution to Maxwell's equations. This solution is known as the eigenvalue equation [16]. The eigenvalue equation relates β to an optical fibre's dimensions and refractive indices at any wavelength, for any mn mode. By subtracting the contribution of the material's GVD from β, an accurate solution of the waveguide dispersion is established. As an example, Figure 2.2(a) shows the total GVD profile (blue) of the LP_{01} mode, for a single crystal silicon optical fibre with a 400nm core diameter, calculated using the eigenvalue equation. The material contribution to the GVD (green) is calculated with Equation 2.15. Subtracting the two quantities reveals the exact waveguide dispersion (red). To illustrate how the waveguide geometry affects the GVD of a high index material such as silicon, Figure 2.2(b) shows the variation in the total dispersion for a variety of core diameters. Above a diameter of 4000nm, the light essentially only experiences material GVD within this wavelength region. Manipulation of waveguide dimensions provides a large degree of freedom for dispersion tailoring with significant implications in telecommunications.

2.2.3.3 Walk-Off

Dispersion is an important quantity in all optical processes particularly for pulse propagation. As already described, a pulse at wavelength λ_1 will propagate with a different

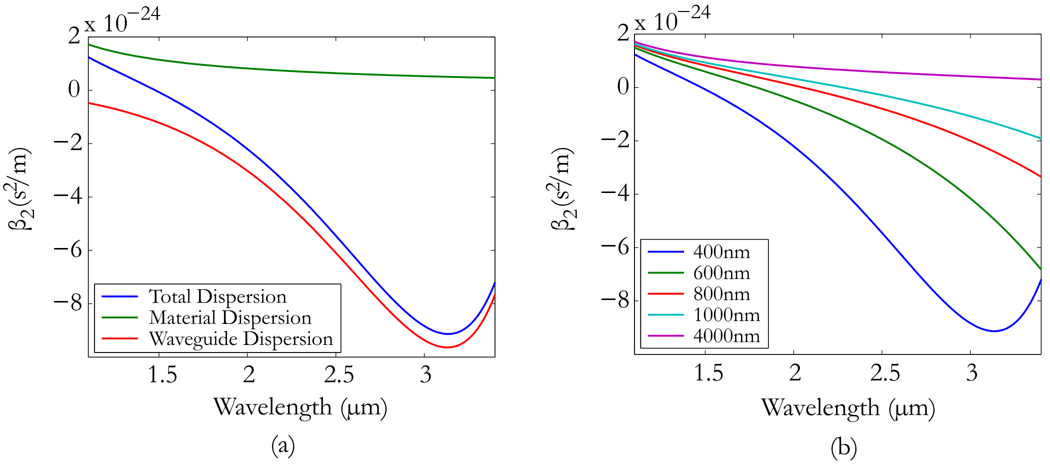

(a) (b)

Figure 2.2: (a) Dispersion contributions for a 400nm core silicon fibre. (b) Effect of dispersion on core diameter in a silicon fibre.

velocity to a pulse at wavelength λ_2. For pulses with a temporal width T_0, their temporal separation length or *walk-off* length L_w [m] is:

$$L_w = \frac{T_0}{\beta_1(\lambda_1) - \beta_1(\lambda_2)}. \tag{2.18}$$

This equation can also be used to estimate the walk-off between pulses of the same wavelength λ_1, but for different transverse optical modes of a waveguide. In this scenario the denominator would be replaced by $\beta_{1,ij}(\lambda_1) - \beta_{1,mp}(\lambda_1)$ where ij and mp are the mode orders.

2.2.4 Linear Losses

When light propagates through a medium it experiences attenuation based on the material's properties. In semiconductors this attenuation can be primarily attributed to electronic absorption or scattering, both of which are wavelength dependent. The total linear transmission loss is represented by α_l [m^{-1}]. The incident optical power P_i [W] attenuates as a function of fibre length L [m], so that the transmitted power P_t [W] can be expressed by the Beer-Lambert law:

$$P_t = P_i \exp(-\alpha_l L). \tag{2.19}$$

Typically α_l is expressed in decibels per unit length [dB/m] through the relationship,

$$\alpha_{\mathrm{dB}} = -\frac{10}{L}\log\left(\frac{P_t}{P_i}\right). \tag{2.20}$$

Due to the base-e base-10 logarithmic conversion, it can be easily shown that the two attenuation coefficients are related by $\alpha_{\mathrm{dB}} = 4.343\alpha_l$. The contribution to the two

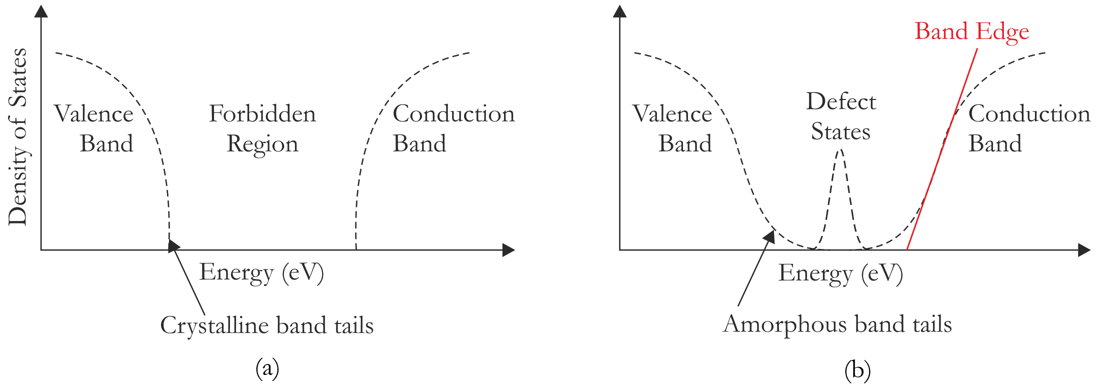

Figure 2.3: Density of states for (a) single crystal and (b) amorphous semiconductors from [29].

dominant linear attenuation mechanisms affecting transmission in semiconductors are described in the following.

2.2.4.1 Material Absorption

The lowest absorption window for a semiconductor is determined by its band gap or band edge energy. The structural order of semiconductors whether crystalline, polycrystalline, or amorphous contribute to the band gap energy of the material. Crystalline materials have sharply defined transitions between the conduction and valence band as shown in Figure 2.3(a). No electronic states exist between these bands. In crystalline silicon (c-Si), the band gap energy (1.1 eV) appears as a transition at $\lambda_{\mathrm{bg}} \sim 1130\,\mathrm{nm}$ in the optical transmission spectrum [27]. In contrast, amorphous materials have extended tails so that the band edges are approximated with a linear fit [28] as illustrated in Figure 2.3(b). From this approximation, the band edge for amorphous silicon (a-Si) is commonly estimated at $\lambda_{\mathrm{bg}} \sim 730\,\mathrm{nm}$ (1.7 eV) [29]. Furthermore, the disordered network of an amorphous matrix reduces the ability for an atom to bond to its neighbour resulting in coordination defects. These defects manifest as electronic states shown in Figure 2.3(b). Wavelengths red-shifted to the band edges typically demonstrate clear transmission. Incident photon energies higher than the band gap energy are strongly absorbed by the material due to a direct electronic transition from the ground state to the conduction state [30], the process is known as interband, band gap, or band edge absorption. Consequently, excited state electrons called *free carriers* dramatically increase the absorption of the material due to intraband electronic transitions.

Intraband or free carrier absorption (FCA) is described by the Drude-Lorenz equation [31]:

$$\Delta\alpha_{\mathrm{FCA}} = \frac{e^3\lambda_0^2}{4\pi^2 c^3 \varepsilon_0 n}\left[\frac{N_e}{\mu_e(0.26m_0)^2} + \frac{N_h}{\mu_h(0.39m_0)^2}\right], \tag{2.21}$$

where e [C] is the electronic charge, λ_0 [m] the vacuum wavelength, c [ms^{-1}] the speed of light, ε_0 [Fm^{-1}] the permittivity of free space, n the refractive index, $N_{e,h}$ [m^{-3}] the electron and hole densities, $\mu_{e,h}$ [m^{2}V^{-1}s^{-1}] the electron and hole mobilities, and m_0 [g] the free electron rest mass [32, 33]. Efforts to decrease the magnitude of additional absorption caused by FCA involve reducing the lifetime for which free carriers remain in an excited state.

The carrier lifetime (τ) quantifies the average time a typical free carrier takes to lose its energy and return to a ground state, the process is known as recombination. Recombination can occur in many forms. Indirect band gap semiconductors like silicon and germanium, recombination is primarily mediated through phonons, defect traps, or thermalisation (intraband transitions). Among the various schemes in carrier lifetime reduction, the most notable approaches are based on carrier depletion [34–36], material modification through ion implantation [37], surface state modification [38], and lastly cryogenic cooling [39].

2.2.4.2 Rayleigh Scattering

Rayleigh scattering is an elastic scattering of light whereby scattered photons have the same wavelength as the input photons. It is strongly wavelength dependent and varies inversely with the fourth power of the wavelength λ^{-4} [40]. In optical fibres, Rayleigh scattering arises as a result of density or compositional fluctuations in the refractive index of the core and cladding, naturally occurring in disordered amorphous materials. For this reason, single crystal optical fibres in principle may have a very low theoretical loss [41] due to the ordered lattice structure. Rayleigh scattering sets the minimal achievable loss for any optical fibre as it relies on the purity of the fabrication process.

2.3 Nonlinear Propagation

Dipoles in the presence of a low intensity electric field $\mathbf{E}$ [Vm^{-1}] can be accurately modeled as a harmonic oscillator [42]. When a propagating electromagnetic field is strong enough, the optical properties of the surrounding material are modified by the presence of that field. Nonlinearities arise when the response of the material depends in a nonlinear manner upon the strength of the applied field, requiring treatment of the anharmonic oscillator model [43].

The optical response can be generalized by expanding the dipole moment per unit volume, or polarization $\mathbf{P}$ [Cm^{-2}] as a power series in the field strength $\mathbf{E}$ [11]:

$$\mathbf{P_i} = \varepsilon_0 \left[\sum_j \chi^{(\mathbf{1})}_{\mathbf{ij}} \mathbf{E_j} + \sum_{jk} \chi^{(\mathbf{2})}_{\mathbf{ijk}} \mathbf{E_j E_k} + \sum_{jkl} \chi^{(\mathbf{3})}_{\mathbf{ijkl}} \mathbf{E_j E_k E_l} + \cdots \right] \tag{2.22}$$

where the polarization of the i^{th} field depends on input fields j, k and l. $\chi^{(n)}$ is the n^{th} order of the tensor susceptibility. The dominant contribution to $\mathbf{P_i}$ is the linear $\chi^{(1)}$ term. The harmonic oscillator approach relates $\chi^{(1)}$ to the refractive index n and the attenuation coefficient α_l by the relations:

$$n(\omega) = 1 + \frac{1}{2}\Re\left[\chi^{(1)}(\omega)\right], \tag{2.23}$$

$$\alpha_l(\omega) = \frac{\omega}{nc}\Im\left[\chi^{(1)}(\omega)\right]. \tag{2.24}$$

These equations relate the frequency dependence of n to the real part ($\Re$) of $\chi^{(1)}$, and the imaginary part ($\Im$) of $\chi^{(1)}$ to the material loss α_l.

Higher order susceptibilities ($\chi^{(2)}, \chi^{(3)} \dots$) are proportional to the products of the input electric fields [44], resulting in n^{th}-generation of frequency harmonics. For example $\chi^{(2)}$ produces frequency doubling or *second harmonic generation* [45]. The generation of these harmonics, whether even or odd, depend on the external symmetry of a medium. Centro-symmetric media ($\chi^{(3)}$) prohibits even ordered nonlinearities since a reversal in electric field $\mathbf{E}(t)^{2n}$ does not imply reversal of the induced polarization $\mathbf{P}(t)$ [11]. Typically, the presence of field interactions in a $\chi^{(3)}$ medium leads to nonlinear effects such as self-phase modulation and four-wave mixing [46]. Frequency mixing and harmonic generation require certain conditions to satisfy phase matching, which is generally difficult to achieve. Thus, high intensity effects are dominated by nonlinear refraction and absorption.

2.3.1 Nonlinear Refraction

The nonlinear index change due to the third order susceptibility is known as the optical Kerr effect. It is responsible for a number of nonlinear effects. The key nonlinearities discussed here will include the effects of a high intensity pulse at one wavelength leading to self-phase modulation (SPM), and the effects of a high intensity pulse on a pulse at another wavelength (or polarisation) known as cross-phase modulation (XPM). In the presence of excessive free carriers, the refractive index can likewise be perturbed according to the Drude-Lorenz model [32].

2.3.1.1 Self-phase Modulation

The refractive index of a material changes in response to an optical field. The induced index change has a quadratic dependence on the applied optical field amplitude. The final index can be written as:

$$\widetilde{n}(\omega, t) = n(\omega) + n_2 I(t). \tag{2.25}$$

The nonlinear Kerr coefficient n_2 [m^{2}W^{-1}] for $\chi^{(3)}$ materials is related to the third order susceptibility by [47]:

$$n_2 = \frac{3}{4\varepsilon_0 c n^2} \Re \left[\chi^{(3)} \right]. \tag{2.26}$$

Due to the intensity dependence of the refractive index, an input beam induces a refractive index variation within the material, with a larger index at the center than the wings of the beam profile. Since the phase of an optical wave is proportional to $\widetilde{n}(\omega, t)$ and thus the field's intensity $I(t)$, nonlinear modulation effects arise in the phase of the input field. The change in phase of the optical pulse from nonlinearity is called SPM. Assuming a medium responds instantaneously to the pulses intensity, we may express the total phase $\phi(\omega, t)$ as:

$$\begin{aligned} \phi(\omega, t) &= \omega_0 t + \left[n(\omega) + n_2 I(t) \right] k_0 z \\ &= \omega_0 t + \phi_L(\omega) + \phi_{NL}(t), \end{aligned} \tag{2.27}$$

where $\phi_L(\omega) = n(\omega) k_0 z$ is the linear shift in phase and $\phi_{NL}(t) = n_2 I(t) k_0 z$ is the nonlinear time varying phase shift due to SPM and is responsible for spectral broadening. Since the nonlinear phase shift is linearly dependent on the input optical intensity, applications requiring high nonlinearity commonly utilise fibre geometries with small effective mode areas to enhance the intensity and hence nonlinear phase shift.

2.3.1.2 Cross-phase Modulation

When multiple channels of light co-propagate through an optical fibre with sufficient power, each one will induce its own nonlinear phase shift. Subsequently, the optical waves see a modified refractive index not only due to its own intensity but also due to the co-propagating pulse intensities. This influence of refractive index coupling leads to an alternate form of phase modulation called XPM where each pulse induces a frequency dependent phase shift on the other [48]. The nonlinear phase shift can be found by expansion of the third order polarizability when considering an electric field $\mathbf{E}(\mathbf{r}, t)$ containing two beams at ω_1 and ω_2. The XPM induced nonlinear phase may be expressed as:

$$\phi_{NL} = n_2 k_0 L \left[I_1(t) + 2 I_2(t) \right]. \tag{2.28}$$

This phase shift indicates that both SPM and XPM occur together. For equally intense fields, XPM dominates SPM by a factor of 2. Thus, consideration of XPM is vital for systems incorporating two or more co-propagating beams.

2.3.2 Two-Photon Absorption

High intensity laser radiation can cause the transmissivity in semiconductors to dramatically reduce. This increase in attenuation is primarily a consequence of simultaneous

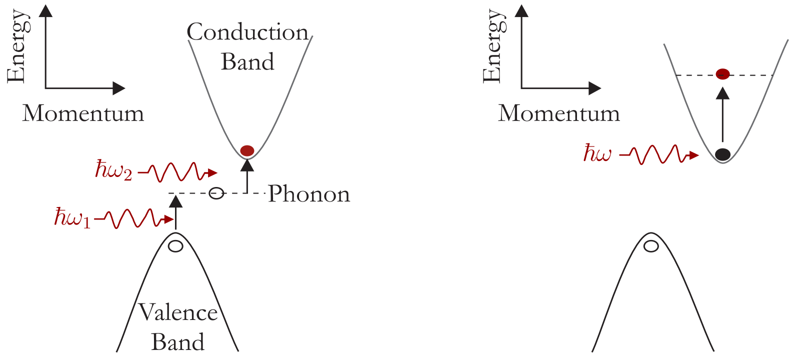

(a) (b)

Figure 2.4: (a) Two-photon absorption. (b) Free carrier absorption.

absorption of multiple photons. For short pulse propagation in silicon, two-photon absorption (TPA) is the dominant mechanism for nonlinear absorption. Thus, for a strongly absorbing nonlinear optical material the effective interaction length can be much shorter than the physical length of the nonlinear medium. TPA however, does have the advantages of low absorption for a weak signal, fast temporal response, and it does not alter the beam quality. For these reasons, TPA has been used for optical intensity stabilization [49], temporal pulse reshaping [50], and spatial field reshaping [51]. Silicon is well suited to these applications as it has a large TPA coefficient and high damage threshold. The incorporation of silicon into a fibre geometry is advantageous as it enables long lengths and cross-sectional tunability through its dimensions.

For the case of indirect band gap semiconductors (like silicon), the TPA process is best illustrated by an energy-momentum diagram. In Figure 2.4(a), carriers in the valence band (ground state) are transitioned to an excited state (conduction band) through simultaneous absorption of two incident photons. Their absorption is assisted through phonon transitions allowing carriers to bridge the forbidden region. Consequently, the presence of carriers in the conduction band result in FCA as shown in Figure 2.4(b). This process of TPA-induced FCA will be discussed in Section 2.3.3.

The depletion of optical power as a result of TPA depends on the TPA coefficient β_{TPA} [mW^{-1}], which can be described through the $\chi^{(3)}$ nonlinearity [47]:

$$\beta_{\mathrm{TPA}} = \frac{3\omega}{2\varepsilon_0 c^2 n^2} \Im\left[\chi^{(3)}(\omega)\right]. \tag{2.29}$$

β_{TPA} can be minimized (or eliminated entirely for single crystals) by choosing the incident photon frequencies for which their total energy $2\hbar(\omega_1+\omega_2)$ lies below the band gap energy of the material. The frequency of the input photon can also influence the type of TPA that occurs. In the following, an analytical description for the case of degenerate ($\omega_1 = \omega_2$) TPA, and non-degenerate ($\omega_1 \neq \omega_2$) TPA is discussed.

2.3.2.1 Degenerate TPA

Ignoring the generation of free carriers, the degenerate TPA intensity-dependent attenuation can be expressed by [52]:

$$\frac{dI}{dz} = -\beta_{\mathrm{TPA}} I^2(z,t). \tag{2.30}$$

Where the optical intensity is related to the amplitude of the optical pulse $A(z,t)$, described in Equation 2.5 or Equation 2.6, via:

$$I(z,t) = |A(z,t)|^2 / A_{\mathrm{eff}}. \tag{2.31}$$

Equation 2.30 can be solved analytically through the separation of variables method:

$$I(z,t) = \frac{1}{\beta_{\mathrm{TPA}} z - C(t)} \tag{2.32}$$

where $C(t)$ is the integration constant. By introducing the condition that $I(z=0,t) = I_0(t)$ where the optical intensity at the interface of the fibre $(z=0)$ is $I_0(t)$ then,

$$C = -\frac{1}{I_0(t)} \tag{2.33}$$

so that the output intensity is now:

$$I(z,t) = \frac{I_0(t)}{I_0(t)\beta_{\mathrm{TPA}} z + 1}. \tag{2.34}$$

From this equation it can be concluded that when $I_0(t) \ll 1$, the output optical intensity $I(z,t)$ scales linearly with $I_0(t)$. That is, in the absence of all other attenuation mechanisms:

$$\lim_{I_0(t)\to 0} I(z,t) = I_0(t). \tag{2.35}$$

This suggests that TPA only affects high intensity optical fields. In this scenario, it is important to realise that the extent of absorption due to TPA is not infinitely high but the output intensity will asymptotically approach a finite value. This value is related to the magnitude of β_{TPA} and propagation distance z by:

$$\lim_{I_0(t)\to \infty} I(z,t) = \frac{1}{\beta_{\mathrm{TPA}} z}. \tag{2.36}$$

These limiting features of the TPA process on a continuous wave (CW) can be seen in Figure 2.5(a). In this figure, Equation 2.34 is simulated using an input peak power of 400 W, $\beta_{\mathrm{TPA}} = 7 \times 10^{-12}$ m/W (c-Si), and a fibre interaction length of $z = 3$ cm. For a 6 μm core diameter c-Si optical fibre, the strong refractive index contrast between the core and cladding requires a numerical method of calculation of the fundamental mode's effective mode area. COMSOL was used as a tool in obtaining this calculation

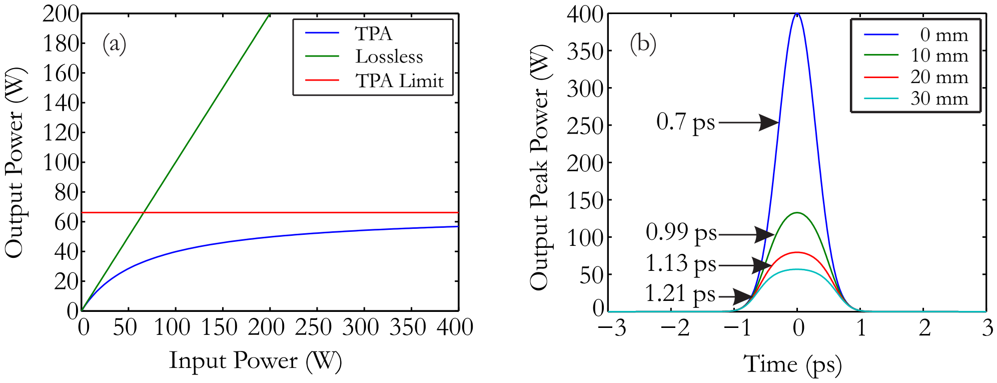

Figure 2.5: (a) Effects of optical limiting due to degenerate TPA. (b) Degenerate TPA on a 700 fs pulse.

revealing $A_{\mathrm{eff}} = 13.9 \times 10^{-12}\,\mathrm{m}^2$. It is also important to note that the TPA coefficient β_{TPA} is a wavelength dependent parameter and the value chosen represents that of c-Si at $\lambda = 1.5\,\mu$m. The figure emphasizes the nonlinearity in TPA relative to the lossless transmission. For very low input powers there is a linear approximation to the loss as expected, though for higher powers the limit approaches $1/\beta_{\mathrm{TPA}}z \sim 66\,\mathrm{W}$.

In Figure 2.5(b), a Gaussian optical pulse with full width at half maximum (FWHM) of 700 fs is simulated as a function of propagation distance. Since TPA affects the highest intensity components of the pulse, it appears to modify the pulse shape into a super-Gaussian like function for larger interaction lengths. Consequently, this creates the perception of dispersion-like pulse broadening with the indicated FWHM varying from 700 fs to 1.2 ps. Though unlike dispersion, the wings of the pulse remain unchanged within its time window, and TPA has simply caused depletion of the peak. If the input pulse had an extremely high optical intensity (such that $I_0(t) \rightarrow \infty$) then propagation after each segment would cause the peak of the pulse to flatten at $1/\beta_{\mathrm{TPA}}z$ producing larger widths. It is next considered how the TPA process would be affected by the presence of an additional optical pulse at a different wavelength.

2.3.2.2 Non-Degenerate TPA

In many circumstances it is common to propagate optical pulses with different wavelengths simultaneously inside an optical fibre. Assuming two distinct wavelength pulses (a pump and a signal) of arbitrary intensities, a probability exists that two-photons may simultaneously be absorbed by the pump pulse ($\beta_{\mathrm{TPA}p,p}$), by the signal pulse ($\beta_{\mathrm{TPA}s,s}$), by the pump then the signal ($\beta_{\mathrm{TPA}p,s}$), and lastly by the signal then the pump ($\beta_{\mathrm{TPA}s,p}$). The last two forms of TPA are known as cross-absorption. It is found that:

$$\frac{\beta_{\mathrm{TPA}p,s}}{\omega_p} = \frac{\beta_{\mathrm{TPA}s,p}}{\omega_s}, \tag{2.37}$$

irrespective of the pump and signal frequencies [53]. In many of the situations encountered in this thesis, the presence of a strong pump co-propagating with a weak signal is considered where both ω_p and ω_s are closely spaced. This leads to two approximations. The first implies that degenerate TPA from the signal is negligible ($\beta_{\mathrm{TPA}s,s} = 0$) since the signal intensity is not sufficient to create TPA. The second approximation states that $\beta_{\mathrm{TPA}p,s} \approx \beta_{\mathrm{TPA}s,p}$, since the optical frequencies are very similar. Thus we assume a similar effective mode area for the pump and signal waves. With these approximations, it is possible to produce a set of simplified coupled-mode equations describing cross-TPA.

From Equation 2.5 and Equation 2.6, the optical pulse comprises of a real amplitude and a complex phase component, hence the pump pulse's full form may be expressed as $A_p(z,t)\exp(i\phi)$. From this it can easily be shown that:

$$|A(z,t)|^2 = A_p^2(z,t). \tag{2.38}$$

Substitution of Equation 2.31 and Equation 2.38 into Equation 2.30 gives,

$$\frac{d}{dz}A_p^2(z,t) = -\beta_{\mathrm{TPA}p,p}\frac{A_p^4(z,t)}{A_{\mathrm{eff}}}. \tag{2.39}$$

The left hand derivative is simplified using a special case of the chain rule, also known as the product rule. This gives:

$$\begin{aligned}\frac{dA_p(z,t)}{dz} &= -\frac{\beta_{\mathrm{TPA}p,p}}{2}\frac{A_p^3(z,t)}{A_{\mathrm{eff}}}\\ &= -\frac{\beta_{\mathrm{TPA}p,p}}{2}I_p(z,t)A_p(z,t).\end{aligned} \tag{2.40}$$

Inclusion of the signal pulse is represented by [54]:

$$\frac{dA_s(z,t)}{dz} = -\beta_{\mathrm{TPA}p,s}I_p(z,t)A_s(z,t). \tag{2.41}$$

Equation 2.40 and Equation 2.41 form a pair of coupled-mode equations describing the influence of TPA on both pump and signal fields. The pair of equations can likewise be solved analytically using a similar procedure as done on Equation 2.30 and evaluating the integration constant. A detailed derivation can be found in Appendix A, where the solution to Equation 2.41 is stated here as:

$$I_s(z,t) = \frac{I_{0s}(t)}{\left[I_{0p}(t)\beta_{\mathrm{TPA}p,p}z + 1\right]^{\frac{2\beta_{\mathrm{TPA}p,s}}{\beta_{\mathrm{TPA}p,p}}}}, \tag{2.42}$$

and $I_{0s}(t)$ is the initial signal pulse amplitude. The solution for a weak CW signal in the presence of a strong CW pump is shown in Figure 2.6(a) as a function of pump power and propagation length. Most variables are simulated with the parameters used in Section 2.3.2.1. The pump power was varied from $0 - 400\,\mathrm{W}$, with a $1\,\mathrm{W}$ signal, and

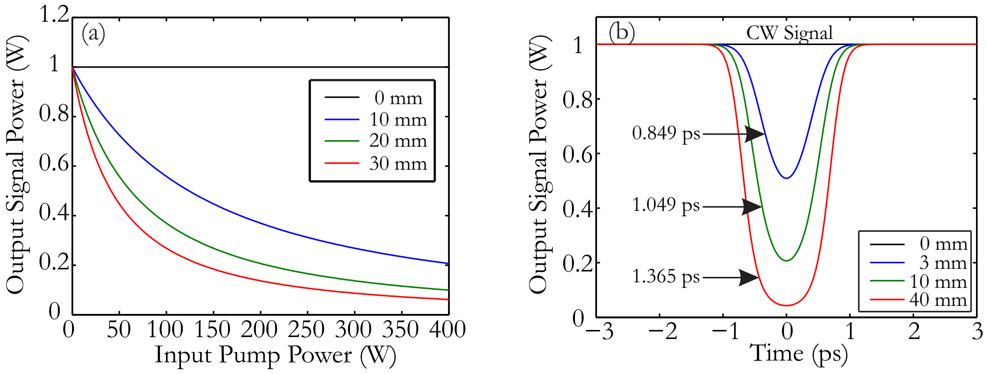

Figure 2.6: (a) Effects of a CW pump on a CW signal wave through non-degenerate TPA showing gradual depletion of the signal's output power. (b) Non-degenerate TPA with a 700 fs pump pulse on a CW signal as a function of interaction length. The signal depletes with a trend following the pump pulse.

a $\beta_{\mathrm{TPA}p,s} \sim 5 \times 10^{-12}$ m/W. The non-degenerate TPA coefficient used is an estimate for silicon at a signal wavelength of 1.57 μm. The figure shows that as the pump power (or intensity) increases, the absorption due to cross-TPA increases. Hence the output signal power drops as the pump power increases. For larger interaction lengths the same is true, but the magnitude of absorption is stronger. The result is different to that of the degenerate TPA figures where an asymptotic value was approached. From Equation 2.42 it can be identified that in the limit to which the term $I_{0p}(t)\beta_{\mathrm{TPA}p,p}z \to \infty$, the output signal still depends on the initial signal power, pump power, TPA coefficients, and the interaction length, suggesting that this non-degenerate process is non-limiting in the absence of pump depletion.

For a 700 fs pump pulse in the presence of a CW signal, Figure 2.6(b) shows how non-degenerate TPA can be used to produce amplitude modulation on the signal. The original CW signal at 1 W is the solid black line just at the interface of the fibre. After 3 mm, the signal (and hence pump) experiences TPA following the envelope of the pump. The depletion causes a perturbation in the signal power forming a dark pulse. More importantly, for short interaction lengths (or equivalently low pump powers) the process produces dark pulses with a FWHM similar to the ultrashort pump pulses. Though, for longer interaction lengths (or stronger pump powers), the strength of the absorption extends into a larger window due to the change of the pump pulse width causing the dark pulse to also broaden.

This characteristic of TPA based amplitude modulation also resembles an optical equivalent of a logical NOT-gate, where an optical *on* in the pump causes an optical *off* on the probe. While the simplicity of the process implies a novel optical device, in reality, silicon does not possess perfect two-photon behaviour as outlined here. As mentioned in Section 2.3.2, the simultaneous absorption of two-photons is almost always followed by the generation of a free carrier. Free carriers cause absorption which in turn modifies the shape of the dark pulses, the relaxation time (rise time for dark pulses), and the rate of absorption [55]. It is therefore necessary to consider how the free carrier density $N_{e,h}(z,t)$ evolves as a function of time (t) and propagation distance (z).

2.3.3 Free Carrier Density

Free carriers in a semiconductor vary in concentration depending on the input optical intensity. As mentioned in Section 2.2.4.1, their presence leads to optical absorption. This type of absorption is due to optical transitions between electronic states in the same band, it is therefore necessary to understand the dynamics of the carrier density since their concentrations are heavily influenced by the input optical pulses. When free carriers are generated, lateral diffusion (along x,y,z directions) and recombination will impact the total free carrier density. In the two-band approximation it is valid to assume equal densities of electron and hole carriers such that $N_e = N_h = N$ [56]. For a pulsed input, Equation 2.21 can now be simplified to [57]:

$$\begin{aligned}\Delta\alpha_{\text{FCA}} &= \frac{e^3\lambda_0^2}{4\pi^2 c^3\varepsilon_0 n}\left[\frac{1}{\mu_e(0.26m_0)^2} + \frac{1}{\mu_h(0.39m_0)^2}\right] N(z,t) && (2.43)\\ &= \sigma_{\text{FCA}} N(z,t) && (2.44)\end{aligned}$$

where σ_{FCA} [m^2] is the FCA cross-section and the simplest method of calculating $N(z,t)$ is by the rate equation [52, 58]:

$$\frac{dN}{dt} = \frac{\beta_{\text{TPA}}}{2\hbar\omega} I^2(z,t) - \frac{N(z,t)}{\tau}. \tag{2.45}$$

A derivation to Equation 2.45 can be found in Appendix B. Though this would not apply to direct band gap semiconductors as the effects of radiative recombination would need to be accounted for [59–61]. While the lifetime τ is usually quoted with a single numerical value, it is important to realise that this quantity is a weighted average of the carrier's behaviour due to the influence of random perturbations such as surface states, interface impurities, and other defects [62]. That is, an electron-hole pair ceases to exist after a mean time τ, which typically varies between picoseconds to nanoseconds depending on the defect density in the material. Recombination mechanisms will be discussed in Section 4.3.

2.3.4 Free Carrier Absorption

FCA is also referred to as intraband absorption. A photon's energy is absorbed by an electron already in the conduction band, raising it to a higher state of energy. The relationship governing FCA was introduced in Section 2.3.3 in Equation 2.44. The Drude-Lorenz model that defines this equation is derived by classical electromagnetic theory whereby an electron in the presence of an electric field is treated as a harmonic oscillator. The derivation assumes that the damping constant is wavelength independent, realistically this is not entirely true since damping mechanisms such as optical phonons and impurities are wavelength dependent [63]. Hence, the quadratic dependence of λ_0 in Equation 2.44 represents the ideal case of a semiconductor. The wavelength dependence of the carrier cross-section σ_{FCA} will not be presented here, though its role in FCA will be discussed.

Excluding doped semiconductors, FCA is not an independent quantity. It is often assisted by TPA. The equation describing the intensity of an optical pulse after propagation through a semiconductor waveguide is now:

$$\frac{dI}{dz} = -\beta_{\text{TPA}} I^2(z,t) - \sigma_{\text{FCA}} N(z,t) I(z,t), \tag{2.46}$$

and is coupled with Equation 2.45. To demonstrate the magnitude of absorption due to FCA and TPA, Figure 2.7(a) shows the variation of output power as a function of an input CW field. The parameters used here are similar to that in Section 2.3.2.1. The carrier cross-section and carrier lifetime are based on the Drude-Lorenz model and values from the literature for c-Si, where $\sigma_{\text{FCA}} = 1.6 \times 10^{-20}\,\text{m}^2$ and $\tau = 10\,\text{ns}$. The TPA behaves as already described for the degenerate case. For CW signals, the carrier density stabilizes at the point for which $dN/dt = 0$. This suggests that the carrier density $N(z)$ will tend to $\tau\beta_{\text{TPA}} I^2(z)/(2\hbar\omega)$. From this steady state solution of $N(z,t)$, it is clear that when substituted back into dI/dz the absorption due to FCA is a cubic function of the input intensity. Hence, a maximum is present in the transmission of the CW field. After this point, the material reaches carrier saturation where the population of recombined carriers is negligible. Dramatic attenuation then occurs for all powers beyond this maximum. It should be noted that hundreds of watts of CW input power is an impractical level when compared to the optical damage threshold for silicon

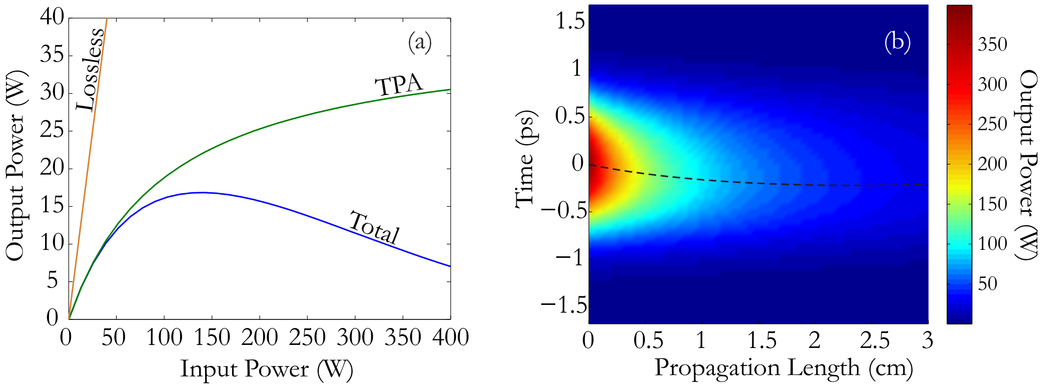

Figure 2.7: (a) Nonlinear absorption on a CW field. (b) Temporal effects of FCA and TPA on a 700 fs Gaussian pulse. Dashed line indicates the drift in the pulse centre due to pulse shaping through TPA and FCA.

($1-4\,\mathrm{GW/cm^2}$ [64]). Hence the values were chosen simply for illustrative purposes. Although pulsed sources can easily reach these power limits, typically a significant number of carriers will recombine between each pulse so that the maximum seen here is usually not observed experimentally.

For a Gaussian pulse propagating a total length of 3 cm, pulse shaping due to FCA begins to occur as TPA continually attenuates the leading edge (negative t) and peak. Figure 2.7(b) is a surface plot of the Gaussian pulse originally centred at $t = 0$, the front end of the pulse is attenuated by TPA and hence free carriers will start to accumulate. Since the carrier lifetime is significantly larger than the optical pulse width, photons present in the medium will suffer FCA. Consequently, the trailing edges of the pulse (positive time) are absorbed causing the centre to shift towards the leading edge. The dashed black line traces the peak of the pulses along a silicon fibre. For consecutive pulses with a temporal spacing less than τ, the latter pulse will also experience the carriers excited by the former pulse as they will not have entirely recombined. This effect can accumulate over time causing significant impairment to a pulsed sequence. This transient behaviour of free carrier concentration has been demonstrated in applications such as pulse compression and mode-locking [50]. From a nonlinear signal processing point of view, it is preferable to obtain short carrier lifetimes, allowing the shape and magnitude of absorption due to FCA to be negligible. The ability to realise such requirements are discussed in Section 4.3.

While the imaginary components of the $\chi^{(3)}$ susceptibility define the nonlinear absorption, the real components of $\chi^{(3)}$ create a perturbation in the refractive index. This nonlinear induced refractive index change causes a material's index to be intensity dependent.

2.4 Generalized Nonlinear Schrödinger Equation

Pulse propagation effects such as dispersion, losses, and nonlinearities can be combined into an equation describing the evolution of a pulse envelope $A(z,t)$ as a function of fibre length. The Nonlinear Schrödinger Equation (NLSE) is generalized (GNLSE) in this case to account for TPA, FCA, free carrier dispersion (FCD), and the evolution of carrier generation. The GNLSE is given by [53]:

$$\frac{\partial A(z,t)}{\partial z} = -i\frac{\beta_2}{2}\frac{\partial^2 A(z,t)}{\partial t^2} + i\gamma|A(z,t)|^2 A(z,t) - \frac{1}{2}(\sigma+\alpha_l)A(z,t). \tag{2.47}$$

The temporal reference t is normalised to the group velocity dispersion β_1 so that the pulse is always centred at the origin. The nonlinear coefficient γ [$\mathrm{W^{-1}m^{-1}}$] defines the strength of a fibre's nonlinearity and is described by:

$$\gamma = \frac{k_0 n_2}{A_{\text{eff}}} + i\frac{\beta_{\text{TPA}}}{2A_{\text{eff}}}. \tag{2.48}$$

The free carrier contribution term is $\sigma = \sigma_{\text{FCA}}(1+i\mu)N(z,t)$ where μ governs the FCD. As described in [65], the relation $\mu = 2k_c k_o/\sigma_{\text{FCA}}$ with $k_c = 1.35 \times 10^{-27}\,\text{m}^3$, is a good estimation related to the change in refractive index associated with free carrier effects, thereby accounting for FCD. Since σ depends on $N(z,t)$, Equation 2.47 is solved in conjunction with Equation 2.45:

$$\frac{dN}{dt} = \frac{\beta_{\text{TPA}}}{2\hbar\omega} I^2(z,t) - \frac{N(z,t)}{\tau}. \tag{2.49}$$

Two important quantities that determine the threshold of the fibre propagation distance z for which dispersion (D) and nonlinearity (NL) contribute significantly to pulse evolution are determined by:

$$L_D = \frac{T_0^2}{\beta_2} \qquad \text{and} \qquad L_{NL} = \frac{1}{\gamma P_0}. \tag{2.50}$$

When $z << L_D$ the effects of dispersion may be ignored. Similarly, the effects of nonlinearity may be ignored when $z << L_{NL}$.

Equation 2.47 and Equation 2.45 represent a pair of nonlinear partial differential equations that can be solved via a numerical approach. Several techniques may be used, though the most extensively employed is the split-step Fourier method. This technique approaches the problem by independently solving the linear and nonlinear contributions to the optical pulse in frequency and time domains respectively. Separation of linear and nonlinear terms are accordingly substituted with the operators $\hat{D}$ and $\hat{N}$. To avoid the complexity of incorporating $dN(z,t)/dt$ a first-order ordinary differential equation in an operator, a solution is initially approximated using Euler's method [66]. Basic numerical integration procedures such as Euler's method suffer from cumulative solution errors with progressing step sizes. However, due to the fixed incremental nature and evolving initial conditions of the split-step method, $N(z,t)$ can be very accurately estimated. This solution and the associated transmission losses are then included in the linear operator. Equation 2.47 written in this form is:

$$\frac{\partial A(z,t)}{\partial z} = (\hat{D} + \hat{N})A(z,t), \tag{2.51}$$

where the corresponding operators are:

$$\hat{D} = -i\frac{\beta_2}{2}\frac{\partial^2}{\partial t^2} - \frac{1}{2}\sigma - \frac{1}{2}\alpha_l, \tag{2.52}$$

$$\hat{N} = i\gamma|A|^2. \tag{2.53}$$

Equation 2.51 is solved as a function of z by repeatedly incrementing the D and N operators by steps of h where $h \ll z$. In this evolution, the optical pulse can be approximated by

$$A(z+h,t) \approx \exp(h\hat{D})\exp(h\hat{N})A(z,t). \tag{2.54}$$

The nonlinear step is performed on the initial pulse in the time domain by:

$$B(z+h,t) \approx \exp(h\hat{N})A(z,t). \tag{2.55}$$

Propagation of $B(z+h,t)$ with the dispersion and loss terms is performed in the frequency domain:

$$\tilde{B}(z+h,\omega) \approx \mathcal{F}\left\{B(z+h,t)\right\}, \tag{2.56}$$

$$\tilde{A}(z+h,\omega) \approx \exp[h\hat{D}(i\omega)]\tilde{B}(z+h,\omega) \tag{2.57}$$

where $\hat{D}(i\omega)$ is the linear operator in the frequency (or Fourier) domain. The time domain solution is calculated by the inverse Fourier transform $\mathcal{F}^{-1}\left\{\tilde{B}(z+h,\omega)\right\}$. Repeatedly iterating the operators in their respective domains over the propagation length provides a good approximation to the final solution. Simulation of this equation is of vital importance to the work performed in this thesis and forms the basis of understanding the nonlinearity in silicon optical fibres.

Chapter 3

Semiconductor Fibre Fabrication

3.1 Introduction

Optical fibre platforms are developing in functionality to encompass a number of new properties such as alternative transmission windows [67], compact fibre devices [63], and flexibility in optical guidance [68]. Examples include the modification of core or cladding materials to include metals, polymers, semiconductors, and fluids [69–72]. In particular, fibres with a semiconductor core in a silica cladding have generated significant interest due to their wider transmission windows and higher nonlinearity. In the past few years, several groups have demonstrated the fabrication of semiconductor fibres extending to both doped and undoped silicon (Si), germanium (Ge), zinc selenide (ZnSe), and indium antimonide (InSb) core optical fibres. This chapter begins with a brief summary of the most notable research in semiconductor fibres and describes the high pressure chemical deposition process developed by Pennsylvania State University and the University of Southampton. Particular emphasis will be placed on the development of silicon optical fibres whose material and linear optical properties are characterised.

3.2 History

The first report of semiconductors deposited within the pores of a silica capillary template was demonstrated in 2006 through a collaboration between researchers at the University of Southampton and the Pennsylvania State University [8]. This early report demonstrated the capability of microstructured silica fibres to withstand very high pressures ($> 10\,\mathrm{MPa}$) of chemical precursors. It also demonstrated the flexibility of incorporating a wide range of materials in a variety of silica templates and dimensions through this high pressure technique. Soon after, the realisation for hybrid silica-semiconductor fibres sparked the interest of other research groups. Contributions include novel fabrication methods from the Max-Planck Research Group, Clemson University, and the Virginia Polytechnic Institute.

Developments in selectively filled germanium photonic crystal fibres (PCFs) were reported in 2008 by Russell *et al.* [73] (Max-Planck), using a pressure assisted filling technique. The purpose was to demonstrate a strongly birefringent fibre by infiltrating selected voids of a PCF with germanium. A polarization extinction of $\sim 30\,\mathrm{dB}$ between x and y components was demonstrated at the output of a silica core. The transmission loss at $1.5\,\mu\mathrm{m}$ for the x-polarization was $\sim 375\,\mathrm{dB/cm}$, and $\sim 156\,\mathrm{dB/cm}$ for the y-polarization.

Soon after, Ballato *et al.* [74–76] (Clemson) reported on the method of sleeving a single crystal silicon rod into a silica preform. This preform was drawn using a conventional fibre draw tower. Long lengths of fibre were fabricated with core diameters of $\sim 60\,\mu\mathrm{m}$ and cladding diameters of 2.3 mm. Reduced core dimensions at this stage have not been reported due to limitations imposed by strong diffusion of oxygen into the silicon core material ($> 60\%$) during the fabrication process. Transmission at $1.53\,\mu\mathrm{m}$ was reported to be 2.7 dB/cm. The same group demonstrated a single crystal germanium core fibre with a core diameter of $300\mu\mathrm{m}$ and an outer diameter of 3mm. Propagation losses were reported to be 0.7 dB/cm at $3.39\,\mu\mathrm{m}$. A polycrystalline InSb core fibre was also fabricated using the generalized molten core approach, in which crystalline wafer fragments of InSb are sleeved into a phosphate glass tube and drawn at moderate ($\sim 700\,^{\circ}\mathrm{C}$) temperatures. However, the strong mismatch in the thermal properties of the semiconductor core and glass cladding materials likewise caused strong diffusion of oxygen into the core in addition to scattering defects and absorption centres. This contamination rendered the optical transmission to be inconclusive. Current pursuits of the group include adapting chalcogenide based claddings to compensate for oxidation effects by minimising the thermal mismatch [77]. Regardless of the obstacles faced, the group's persistence in fabricating semiconductor core fibres via this draw-tower method has gained interest in the scientific community [78, 79].

Lastly, in 2009, Pickrell *et al.* [80,81] (Virginia Tech) demonstrated an n-type silicon core optical fibre by grinding doped silicon wafers into a fine powder and densely packing it into the capillary of a silica preform. The filled preform was then drawn using a customised translation stage over a hydrogen-oxygen flame torch. Large defects at the silicon-silica boundaries were formed during the cooling process due to the thermal mismatch between the materials. Fibres could be fabricated with core diameters from 10 to $100\,\mu\mathrm{m}$, cladding diameters from 40 to $240\,\mu\mathrm{m}$, and lengths from 5 to 12 cm. However, transmission losses were in excess of 250 dB/cm at 1550 nm due to the defected interfaces.

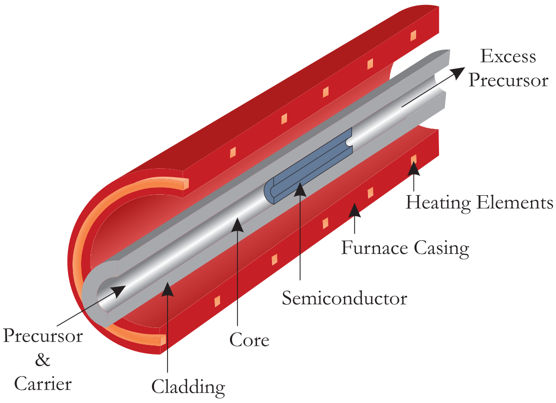

Figure 3.1: Cross-sectional view of deposition procedure.

3.3 Confined High Pressure Chemical Deposition

Optical fibre capillaries fabricated with a conventional 125 μm outer cladding diameter, and a hollow 6 μm (or 2 μm) core form the templates into which semiconductors are deposited. High pressure chemical deposition (HPCD) is a process whereby a gaseous precursor initially pressurises the interior void of this silica capillary. The precursor comprises of a semiconductor compound. For the deposition of silicon, the desired precursor is silane (SiH_4) while for germanium, it is germane (GeH_4). To assist the infiltration of the precursor into high aspect ratio geometries such as a micron-sized capillary, the precursor is diluted in an inert gas (the carrier). Typically this is highly pressurised ($\sim$ 40 MPa) helium or hydrogen [8, 82] with a precursor:carrier ratio of approximately 1 : 19. The pressurised fibre is then steadily heated within a 15 cm tube furnace set above the thermochemical decomposition temperature of the precursor. A cross-sectional schematic of this process is illustrated in Figure 3.1, where annular growth of the desired semiconductor accumulates within the void over time to form the core. Silicon can be deposited in three distinct phases; polycrystalline (p-Si), amorphous (a-Si), or amorphous hydrogenated (a-Si:H). Figure 3.2 illustrates the influence of the furnace temperature on the material's phase and the time required to completely fill a section of fibre with a 6 μm core diameter. For the deposition of polycrystalline silicon, the peak temperature is set beyond the nucleation temperature 550 °C for silicon [83, 84]. Localized clusters of amorphous silicon begin to grow and arrange in a pattern characteristic of a crystalline solid, forming sites (crystallites) upon which additional particles deposit and grow to create polycrystalline silicon. The size of the crystallites can be increased through thermal annealing (temporary exposure to high temperatures) represented by the hatched region above 700 °C in Figure 3.2. For the deposition of pure amorphous silicon however, the peak temperature is kept below the nucleation temperature, but yet still high enough to result in the complete dissociation of silicon and hydrogen from silane. Furnace temperatures below the silicon-hydrogen diffusion threshold of $\sim$ 400 °C [85, 86], minimizes the decomposition of hydrogen elements allowing for higher concentrations of SiH and SiH_2 to grow in the capillary. However very low furnace temperatures can only yield

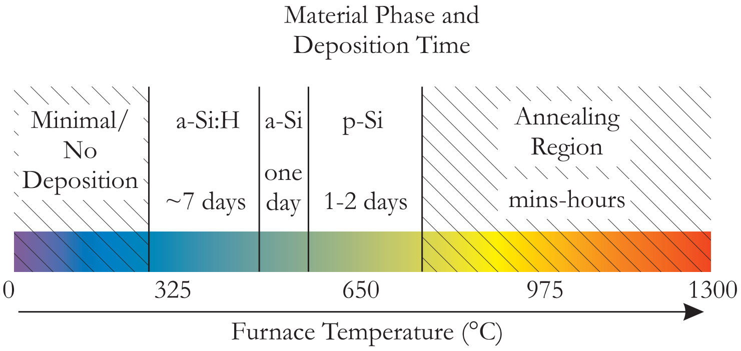

Figure 3.2: Influence of furnace temperature on the deposited semiconductor's material phase and deposition time for complete filling of a 6 μm core.

deposition of nanometer thick films, if any deposition at all, as shown in Figure 3.2 below 325 °C. This deposition process for hydrogenated-silicon is unique to the HPCD method as planar technologies require a complex plasma-enhanced chemical vapour deposition (PECVD) process to incorporate hydrogen in the substrates.

The HPCD method is the first method of its kind to demonstrate the ability to infiltrate optical fibre capillaries with a variety of semiconductors and semiconductor compounds. Aside from the group IV materials already mentioned, II-VI compounds have also been demonstrated in step-index and microstructured optical fibre templates [87,88]. Furthermore, the flexibility of the process allows for conformal layering, selective filling [89,90], and semiconductor heterojunctions with optoelectronic functionality [91]. In this thesis, deposition conditions are typically restricted to temperatures where a-Si:H is deposited due to the excellent optical properties of this material, as will be discussed in Section 3.5.3.4. However, a description of each phase (a-Si:H, a-Si, and p-Si) will be given in this chapter to highlight their properties. Before the material characterisations are performed, the semiconductor fibre is prepared to facilitate imaging and input/output optical coupling.

3.4 Semiconductor Fibre Preparation

The differences in the mechanical properties of the semiconductor compared to silica render standard cleaving techniques to be impractical since micro-fractures scribed on the cladding do not create a smooth cleavage plane across the semiconductor core. Instead, following deposition, completely filled sections of the semiconductor fibre are sectioned off and mounted in a thicker silica capillary as shown in Figure 3.3. The capillaries are secured to the semiconductor fibre by one of two adhesives; beeswax or an epoxy resin. Beeswax has a low melting point temperature ($\sim 63\,^{\circ}$C) and is thus used for low optical power applications, or when fibres need to be removed from the capillary after the characterisations are performed. It is melted to form a softened liquid, where capillary action causes the fluid to slowly fill the gaps between the outer capillary and the inserted semiconductor fibre. When the beeswax completely surrounds the semiconductor fibre, the temperature is immediately reduced to room temperature causing it to re-solidify, fixing the fibre securely within the capillary. For higher optical power applications, an Opti-tec 5053 heat-curing epoxy is used to mount the fibre within the capillary as the strength of adhesion does not degrade until a temperature ($\sim 200\,^{\circ}$C) significantly higher than the melting point of beeswax. When the epoxy has completely filled the capillary it is heated to 120 °C for a few minutes, allowing it to harden, permanently fixing the semiconductor fibre into the capillary. The external silica capillary is coated with a polyimide thermoset which performs a similar task to buffers used on standard optical fibres, having good thermal stability, good chemical resistance, and excellent mechanical properties [92], protecting the capillary from harsh environments.

The semiconductor fibre mounted in the thicker capillary has its end faces prepared using a conventional fibre polishing technique. The polishing equipment and accessories are very similar to those used for the telecom industry. Each fibre is polished with three individual lapping films composed of tiny particles of aluminium oxide or silicon carbide glued to the film surface. The mounted fibre is circulated over the film rotating at ~ 200 rpm, excess material from the fibre is removed and the end is polished to a desired grade of smoothness. Different grades of film are used in successive polishing cycles. Each cycle uses a finer grit paper starting with grades of 3 μm, 1 μm and finally 0.3 μm.

Following the polishing procedure, characterisation of the deposited core is routinely performed. Microscopic images of the polished end faces and spectroscopic properties of the core provide important optical attributes to the material such as scattering losses (through surface deviations) and vibrational resonances (through Raman analysis).

3.5 Material Characterisation

Material characterisation of the fibre core involves analysing four primary features; deposition uniformity, presence of additional chemical elements, material quantity, and optical transmission losses. The first feature is identified through end-face imaging by

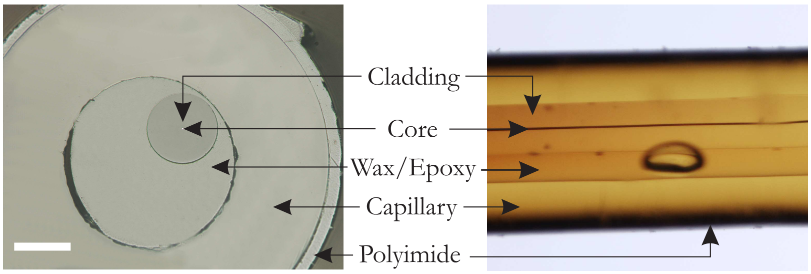

Figure 3.3: (Left) Transverse plane cross-section of a mounted semiconductor fibre; scale bar is 100 μm. (Right) Longitudinal plane of fibre.

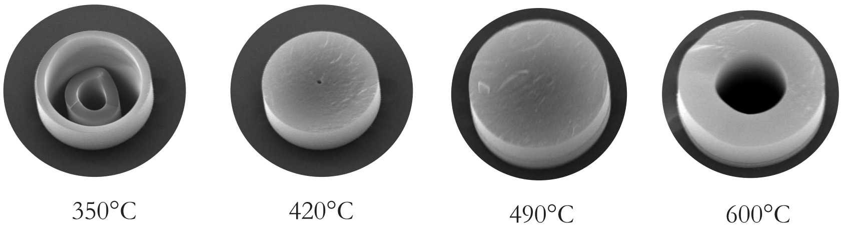

Figure 3.4: Evolution of deposition filling of a 6 μm core silicon fibre as a function of temperature taken for the same deposition time. Imaged using an SEM.

scanning electron microscopy (SEM); the second and third features are analysed through Raman spectroscopy, and lastly, optical transmission losses are measured using a range of laser sources.

3.5.1 Scanning Electron Microscopy (SEM)

SEM images resolve nanoscale features of the deposition uniformity to confirm complete filling. The process involves detecting back scattered electrons from an object which has been sputter-coated in gold (required to prevent charge accumulation due to electron bombardment). High resolution images are obtained by accelerating electrons with a high voltage, and vice versa for low resolution images. However, it should be noted that very high voltages can lead to unclear surface structure (as the electron penetration depth is higher) and risk of surface damage due to excess charge build up, thus careful tuning of the voltage is required to obtain clear images. To facilitate imaging of the inner core surface in semiconductor fibres, the silica cladding is slightly etched back using hydrofluoric (HF) acid, and the acceleration voltage is set to 20 kV. The effect of deposition temperature on the semiconductor core can now be imaged with high detail. Figure 3.4 are cross-sectional SEM images of the etched away silica cladding and exposed semiconductor core. Each image represents deposition performed at a different temperature for the same duration. It can be seen that for low temperatures (a-Si or a-Si:H type material) the rate of deposition is slower and hence requires longer exposure to the furnace in order to develop a void free core, also indicated in Figure 3.2. While increasing the temperature may increase the deposition rate, crystallisation of the amorphous material begins. At 600 °C the amorphous material is consumed by surrounding crystallites forming polycrystalline grains, hence opening the central core region. Crystallites may grow in any orientation and in any size, and their boundaries create imperfections in the material leading to poor optical and mechanical properties of the fibre. These defects, as previously mentioned, can be annealed out by using temperatures of $\sim 1000\,^{\circ}$C [93], though silica's tolerance to prolonged exposure of such high temperatures becomes a limitation. While the images provide a quantitative view of the level of filling in the core, the material's phase and composition indicates the quality of the deposited material.

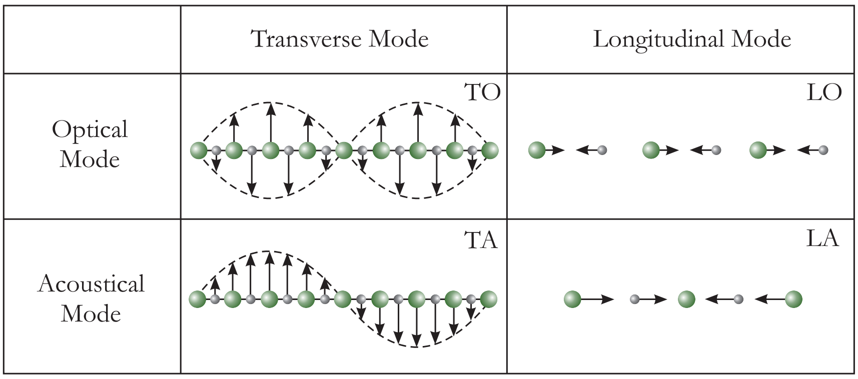

Figure 3.5: Terminology for vibrational displacements of atoms used in Raman spectroscopy from [94].

3.5.2 Raman Spectroscopy

The crystallinity of the core material as well as the presence of additional elements can both be evaluated using Raman spectroscopy. In this process, light is focussed onto the core and the back scattered Raman shifted photons are collected and analysed. The back scattered photons are a consequence of non-elastic scattering where the scattered light is generated through interaction with molecular vibrational modes quantised as *phonons* [94]. Excitation is performed with a Renishaw inVia system with a 633 nm HeNe laser source at 250 μW of optical power. The recorded spectra exhibit resonant peaks specific to the elements in the material and the bonds connecting them, hence related to their vibrational modes. In the one dimensional lattice approximation, atoms may vibrate transversally or longitudinally. Each movement is characterised by either optical or acoustical vibrations depending on the atom's displacement. Figure 3.5 illustrates that optical modes have adjacent atoms with opposing oscillations in transverse (TO) and longitudinal (LO) directions. Acoustical modes of adjacent atoms however, have the same direction of vibration resembling that of an acoustic wave propagating through the material. These also occur in transverse (TA) and longitudinal (LA) directions.

The wavelength shift at which a Raman resonance occurs indicates the elements involved. The strength of the resonance indicates the type of bond connecting these elements e.g. covalent (single/double/triple), ionic, or metallic [95,96]. Though it should be noted that the strength of resonances are typically an ignored quantity in Raman spectroscopy, since elements producing a Raman resonance at a specific wavelength shift have predetermined bond formations established in early literature. The Raman linewidth Γ [Hz] of each resonant peak dictates the level of material order. Very narrow linewidths are associated with highly crystalline material as each resonance is due to a distinct vibrational mode with a very high Raman gain. Broad linewidths however, are due to resonances consisting of a superposition of vibrational modes and are typical of disordered or amorphous materials. The phonon response time τ_{R} [s], defined by the inverse linewidth $1/\Gamma$, governs the fastest time to which an optical pulse can drive a Raman resonance [47,53].

Therefore amorphous materials have smaller phonon response times than single crystal materials.

3.5.2.1 Polycrystalline Silicon (p-Si)

Optical fibres with a p-Si core are composed of many crystalline grains. Their material properties are inherently governed by the grain material, assuming the intergrain regions are significantly smaller than the grain size. The shape, dimension, and orientation of each grain is in most cases strongly related to the fabrication temperature [97]. The average grain size should ideally be as large as possible so that the overall material possess as much similarity to single crystal silicon (c-Si). Research in optimizing the deposition process is still ongoing. Three a-Si fibre samples were fabricated at 500 °C and thermally annealed at different temperatures to produce a p-Si core. Raman spectra were recorded with an acquisition time of $1 - 2$ mins for each anneal and are shown in Figure 3.6(a). As a reference, c-Si is shown with a single narrow peak at 520cm^{-1}, as expected corresponding to the TO mode. The lower temperature anneal results in a broader linewidth and larger shift in the peak wavenumber than the ideal c-Si spectra due to the larger quantity of amorphous material surrounding the crystallites. As the grain sizes are increased through higher temperature annealing, the contribution of amorphous material becomes less, causing the linewidth to become narrower and vibrational resonances to occur with a closer wavenumber to that of c-Si.

3.5.2.2 Pure Amorphous Silicon (a-Si)

a-Si fibres are commonly fabricated at ~ 500 °C. The Raman spectra are acquired for a slightly longer duration (~ 5 mins) as the cross-sectional gain is weaker due to the inverse dependence on Γ [53]. The spectral result in Figure 3.6(b) shows a strong broad peak at 480 cm^{-1} corresponding to the TO mode, with the two weaker subsidiary peaks associated with the LA and LO modes of amorphous silicon [98]. The overlapped modes and hence merged linewidths is a typical characteristic of the amorphous materials. Importantly, the shift of the TO mode with respect to c-Si and p-Si is an important indicator of how much the molecular dynamics in an identical material can change as a result of superimposed vibrational modes, material stresses, and bond disorder.

3.5.2.3 Hydrogenated Amorphous Silicon (a-Si:H)

When semiconductor deposits accumulate in an amorphous state from HPCD, the general disorder of the deposited material results in a high density of defects, which are primarily atomic vacancies. These sites, referred to as *dangling bonds*, are electrically active states in the band gap which can be occupied by any number of electrons (as

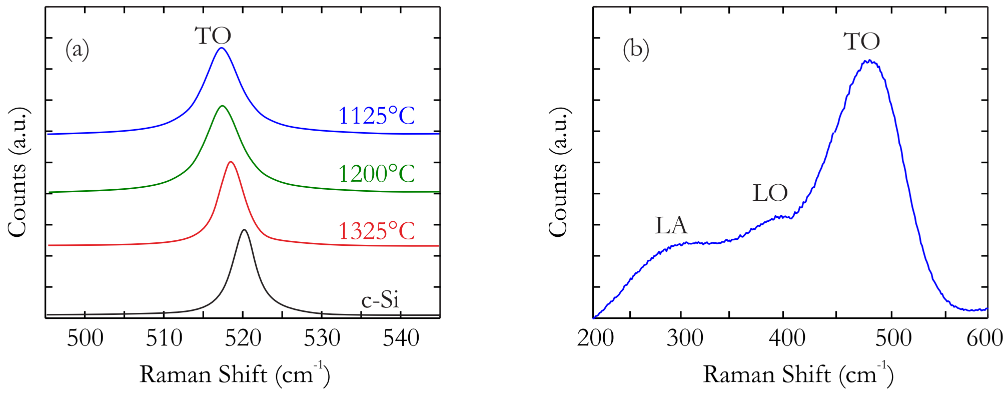

Figure 3.6: (a) Raman spectra of p-Si at different annealing temperatures from [99]. (b) Raman spectra of a-Si.

described in Section 2.2.4.1). The presence of hydrogen in a-Si:H acts to passivate these dangling bond defects in the amorphous material, which in turn alleviates the undesirable optical and electronic features associated with a-Si [82]. Such features include poor optical transmission for photons with energies exceeding the dangling bond defect state, and poor carrier mobility due to the defect states acting as recombination centres for free carriers [100].

The Raman spectra of a-Si:H closely resembles that of a-Si. The presence of hydrogen and hence vibrational mode of Si-H will experience a different Raman resonance due to the different elements and bond structure. The high bond-dissociation energy of Si-H relative to Si-Si (Si-H$\sim$ 314 kJ/mole and Si-Si$\sim$ 218 kJ/mole [101]) in combination with poor passivation, results in a Raman shifted emission for this bond that is consequently very weak, typically requiring tens of minutes worth of high sensitivity acquisition in order to be detected. The unique stretch (S) mode associated with Si-H occurs at a higher detuning of 2000 cm^{-1}. Figure 3.7(a) is the recorded Raman spectra in this vicinity, the black curve confirms the presence of the S mode, a mode which was unobservable in pure a-Si. The presence and detectability of this stretch mode attests to the hydrogenated nature of the material whilst the strength provides some information regarding the concentration. In cases where the hydrogen passivation is high, for example when low temperature depositions are performed or if disilane (Si_2H_6) is used as a precursor, a secondary resonance (Si-H_2) adjacent to the Si-H stretch mode appears ($\sim$ 2100 cm^{-1}), as shown by the blue trace in Figure 3.7(a). Whilst the presence of such high concentrations of silicon hydride may suggest a higher saturation of dangling bond defects, it must be reinforced that low temperature deposition typically does not form a void-free core due to the slow deposition rate. Furthermore, disilane is a highly volatile and costly precursor and is yet to be determined whether the optical or electronic properties are improved with this method. To understand the level of hydrogenation during the fabrication process, Raman spectra were recorded as a function of the deposition temperature. Figure 3.7(b) shows that the S mode steadily increases in strength for the same acquisition time ($\sim$ 20 mins). The lowest temperature of 320 °C resulted in

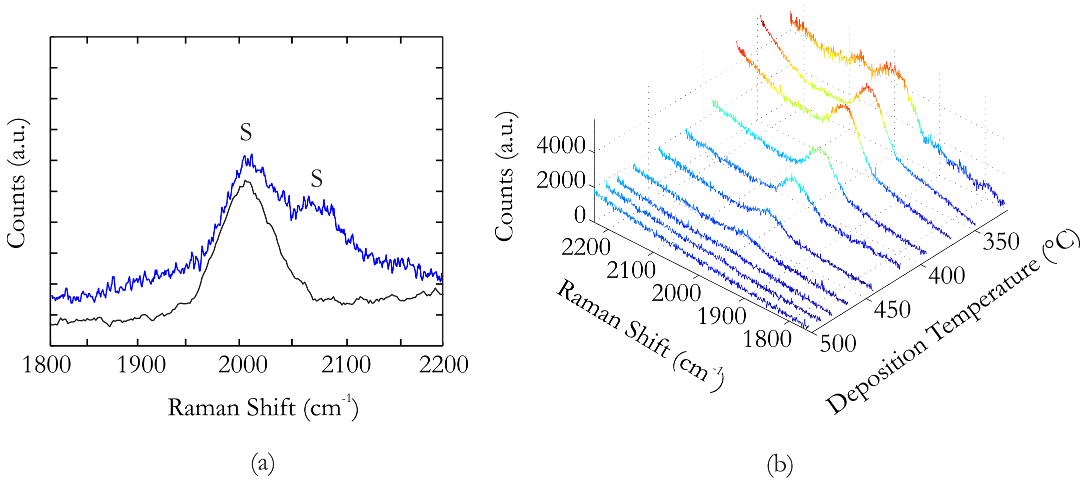

Figure 3.7: (a) Raman spectra of Si-H (black at 390 °C) and inclusion of Si-H_2 (blue at 340 °C) stretch modes in a-Si:H fibres. (b) Evolution of Si-H modes with deposition temperature.

a 380 nm a-Si:H film (observed via SEM) which revealed the two S modes of Si-H and Si-H_2. Extended exposure of the silica capillary to a deposition temperature of 320 °C in order to increase the volume of deposited material did not reveal closure of the core with a-Si:H.

3.5.3 Optical Transmission Characterisation

Optical transmission in semiconductor fibres is strongly influenced by the deposition parameters such as; temperature, partial pressures, precursor concentration, and carrier concentration. The kinematics of the chemistry involved are highly complex and the influence of each parameter is counterintuitive. Educated estimates of the initial parameters are used and optimized based on the SEM characterisations performed. By establishing a fixed set of partial pressures and precursor/carrier concentrations of the system, further material characterisations have helped in determining the optimal temperature for the deposition of p-Si, a-Si, and a-Si:H fibres. When silicon core fibres possess crystallinity, volume uniformity, and composition, close to their bulk counterparts, it indicates that the optical properties should theoretically be of similar standards.

In Section 2.2.4 several mechanisms contributing to the optical attenuation (α_{dB}) in semiconductors were discussed. Semiconductors will have a band gap energy E_g within an exponentially decaying band tail defined by the Urbach energy E_u [102]. For an ideal single crystal semiconductor, $E_u = kT$ where k is Boltzmann's constant and T is the temperature [103]. Amorphous semiconductors (as well as glasses) however, have an Urbach energy correlated to bond angle distortions and fluctuations in the atomic bonding distances [104, 105]. The optical absorption α_u [m^{-1}] due to this tail can be

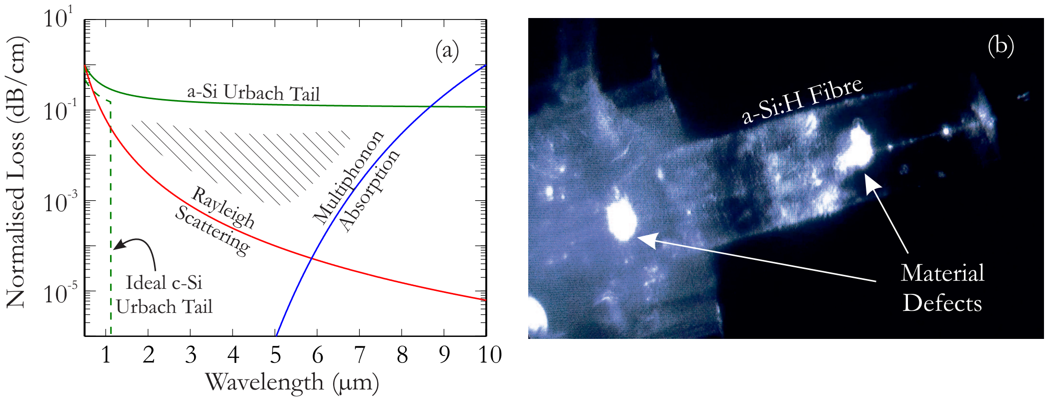

Figure 3.8: (a) Fundamental loss contributions to semiconductor fibres. Hatched region represents wavelengths over which defect based absorption (such as dangling bonds) affect the most. (b) CCD image of defected core material taken using a downward facing infrared camera onto the sample.

approximated by [103]:

$$\alpha_u \sim A\text{exp}\left(\frac{E - E_g}{E_u}\right), \tag{3.1}$$

where A is the absorption scaling factor specific to the material, and E is the energy of the incident photon. As the band tail reduces for photons with smaller E, Rayleigh scattering starts to take over as the fundamental loss mechanism, where the optical absorption α_R is proportional to $1/\lambda^4$. Eventually a material's vibrational harmonics and overtones become prominent in the absorption due to the molecule's resonant frequencies. Photons in this resonant mid- or far- infrared regime experience multiphonon absorption α_m described by [106]:

$$\alpha_m \sim B\text{exp}\left(C\frac{\lambda_{\text{LO}}}{\lambda}\right), \tag{3.2}$$

where B and C are material constants and λ_{LO} represents the maximum longitudinal optical resonant frequency of the material. Figure 3.8(a) plots the relative individual contributions of α_u, α_R, and α_m, over a large region of the optical spectrum for silicon. The ideal c-Si tail is governed by $E_u = kT$, and drops of rapidly in comparison to the pure a-Si Urbach tail. Rayleigh scattering represents the fundamental limit of optical losses for a large range of the spectrum. At 5μm, phonon based absorption steadily begins to dominate. The multiphonon based absorption in this figure is only a theoretical trend, in reality vibrational absorption peaks of varying extinction occur [107].

Figure 3.8(a) depicts an important characteristic for a-Si or a-Si:H. The amorphous nature of the semiconductor results in an optical absorption that is inherently limited by its Urbach tail as seen by its significantly higher magnitude. The hatched region enclosed within the Urbach tail, Rayleigh trend, and multiphoton absorption, represents the absorption from the defect states associated with amorphous material (accounted for by the high E_u). The measured distribution of defects in a-Si:H for example have been identified as dangling bond defects and occur with positive, negative, and neutral charge defect states [104]. Each charge state follows a Gaussian distribution that may be present anywhere within the hatched region. Hydrogenation serves to decrease the corresponding Urbach energy allowing the optical transmission to follow a more Rayleigh influenced trend.

Aside from these known contributions to the optical absorption, physical material defects may occur as a product of non-optimal fabrication or environmental contamination. Clusters of defected material or voids centred within the core cause light to scatter dramatically, degrading the optical transmission. Figure 3.8(b) is an example of a top-down image taken using a sensitive CCD camera with 1.5 μm light incident on a high loss a-Si:H core fibre. The specific origin of these defects are not yet fully understood, though it is also believed that irregularities in the furnace heating elements may cause "hot" or "cold" spots to form in the core, leading to the presence of defected silicon deposits or unfilled regions. This top-down technique of viewing scattered light is a critical step in allowing us to isolate the lowest scattering loss sections of an a-Si:H optical fibre.

3.5.3.1 Experimental Technique

Optical transmission losses are initially measured on all prepared fibres, typically in the near-infrared (NIR). A range of tunable pulsed laser sources at very low peak powers ($\sim$ 10 mW) including a supercontinuum (Fianium SC-400), an optical parametric oscillator (Radiantis OPIUM), and a pulsed erbium fibre laser (Onefive ORIGAMI), were used to access wavelengths from 1.3 μm to 1.8 μm. Figure 3.9(a) shows a typical set up for the optical transmission measurements using these sources. CAM represents the cameras used to image the input and output faces of the fibre with their sensors based on either a CCD or Pyroelectric array depending on the source wavelength. The high Fresnel reflection coefficients of silicon ($\sim$ 0.36 at 1.55 μm) creates a strong contrast difference between the core and the surrounding silica cladding, providing a convenient method such as imaging to ensure the light is launched into the core. O1 and O2 are 0.65 NA/4.6 mm fused silica objectives. PD is the photodetector. Germanium or Indium Gallium Arsenide based photodetectors were used for wavelengths up to 1.8 μm. With this configuration, loss measurements are performed using the cut-back technique [108] where the fibre length is reduced by a few millimeters through polishing. This method isolates an accurate transmission loss of a fibre section provided the same optical elements are used in each measurement. From Figure 3.9(b), the input P_i and transmitted P_t power measured at sample length L_1 and L_2, can be used to calculate the attenuation by:

$$\alpha_{\mathrm{dB\Delta L}} = -\frac{10}{L_1 - L_2} \log \left[\frac{P_{t1}/P_{i1}}{P_{t2}/P_{i2}} \right] \tag{3.3}$$

thus revealing the attenuation of the fibre section $L_1 - L_2$.

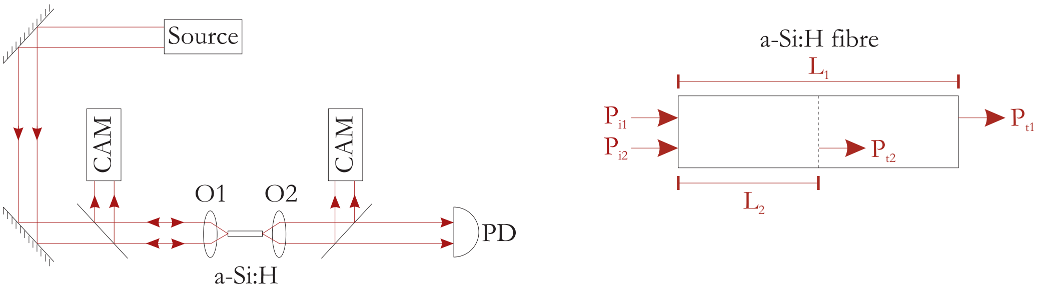

(a) (b)

Figure 3.9: (a) Schematic for loss measurements. (b) Variables of the cut-back technique.

Cut-backs are performed on a number of p-Si, a-Si, and a-Si:H fibres in a wide range of NIR wavelengths. These are discussed in the following sections.

3.5.3.2 p-Si

In the early stages of HPCD fabricated fibres, p-Si core fibres were thought to be the material of choice due to the level of crystallinity (close similarity to c-Si) and potentially useful optical properties. Much effort was focussed on fabricating batches of fibres under different deposition or annealing conditions and correlating this with the optical properties of the p-Si material. The p-Si fibres from Section 3.5.2.1 were characterised using the cut-back technique to establish the transmission loss as a function of wavelength. Figure 3.10(a) shows the corresponding losses for each fibre. Higher annealing temperatures result in larger grain sizes reducing the number of intergrain defect sites, hence the lower loss. Each p-Si fibre exhibits a strong Rayleigh fit shown by the solid lines through the data points indicating the loss is primarily influenced by density fluctuations as expected for a polycrystalline material. An experiment was performed in which a separate a-Si core fibre was thermally annealed for a short duration of 5 mins at

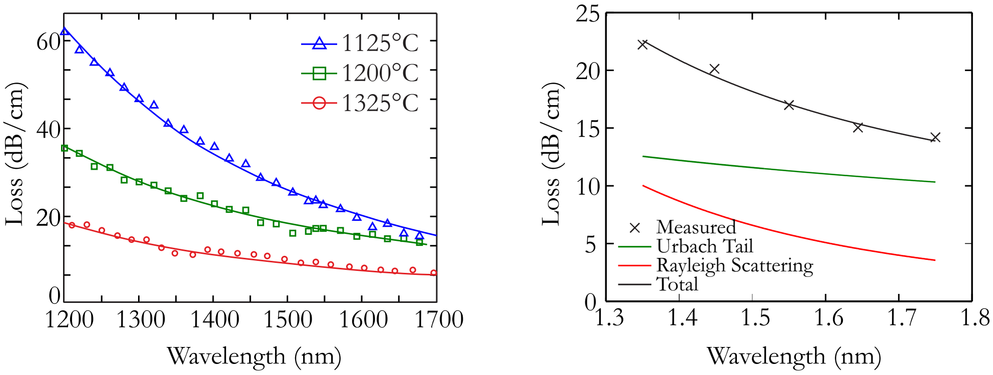

(a) (b)

Figure 3.10: (a) Cut-back loss performed on three p-Si fibres from [99]. (b) Cut-back measurement of a p-Si fibre annealed for a shorter duration.

1300 °C, (as opposed to $10 - 20$ mins) to observe how the optical absorption or scattering changed. Figure 3.10(b) show the losses of this sample for a few points in the NIR spectrum. A Rayleigh trend alone was not sufficient to obtain a good fit such as that in Figure 3.10(a). However, in combination with the Urbach trend where E_u is the only adjustable fitting parameter, a good fit is shown by the solid black line. The band gap energy in theory varies due to the level of material disorder, though it is estimated at 1.1 eV due to the Raman spectra having a similar linewidth to c-Si. Since the Urbach tail appears to dominate the absorption it can be deduced from theory that defect states are a significant factor in this wavelength range.

Transmission losses for p-Si fibres have continued to vary in the range from $7 - 60$ dB/cm rendering the usable physical length to be impractical for nonlinear applications. To achieve lower loss p-Si fibres, larger crystal grains are required or the dangling bond defects between crystal grains need to be passivated [109].

3.5.3.3 a-Si

Pure a-Si fibres are a material that is typically undesirable for optical transmission. The high atomic disorder results in structural defects in the form of distorted bond angles, dangling bonds, and altered atomic bonding coordination, dramatically affecting the density of states and forming absorption centres throughout the material [110]. When comparative investigations are required between fibre core materials, it is usually only then that an a-Si fibre is measured for transmission. Optical losses are frequently in the order of 50 dB/cm at 1550 nm and very rarely follow a definitive Rayleigh trend.

Doping a-Si material may help impede such high transmission losses, with the most commonly employed method (both commercially and academically) being hydrogenation, to form a-Si:H.

3.5.3.4 a-Si:H

In the past decade a-Si:H has gained a scientific attraction due to its advantageous fabrication, optical, and electronic features. Specifically, it can be efficiently fabricated using low deposition temperatures, requiring smaller amounts of raw materials, and it inherently escapes the necessity of achieving a certain level of crystal perfection [111]. a-Si:H has always been a strong candidate for low loss semiconductor waveguides due to almost all dangling bonds being saturated by hydrogen [112]. Low optical losses have been demonstrated in several a-Si:H waveguides in a planar platform in the past few years with values approaching the limit of c-Si [113]. It is for these reasons that a-Si:H is the material of choice for the core of optical fibres investigated in this thesis. The electronic properties of a-Si:H are ideal due to the long carrier lifetimes but its applications are

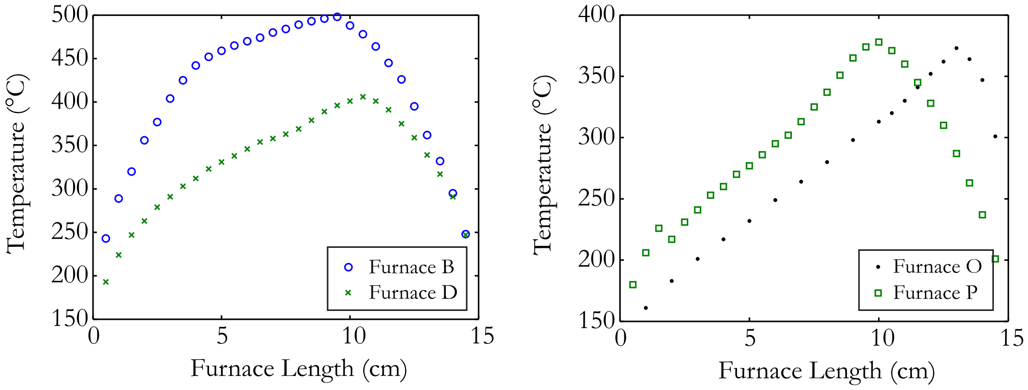

Figure 3.11: Deposition furnace's temperature profiles constructed at Pennsylvania State University.

intended for photoconductive or photovoltaic applications. Carrier lifetimes will be discussed with more detail in Section 4.3.

A large number of a-Si:H fibre were fabricated and optically characterised at 1.54 μm. Four different furnaces labelled 'B', 'D', 'P', and 'O', were handmade at Pennsylvania State University. Each furnace exhibits a different temperature gradient and profile as shown in Figure 3.11. Each fabricated fibre varied in precursor pressure and temperature. When the importance of hydrogen was established, it was suggested to attempt the deposition process with hydrogen as a carrier gas. The consequences on the kinematics of the deposition process were unclear. However, through re-optimisation of the partial pressures, temperatures, and furnace profiles, a number of fibres were investigated with the hydrogen carrier. The deposition details of the 6 μm fibres characterised are shown in Table 3.1 where the switch in carrier gas resulted in many of the lowest loss a-Si:H fibres to date.

Similarly, in the fabrication of 2 μm core fibres, the carrier gas was also replaced. Table 3.2 displays the deposition parameters and loss measurements performed on a batch

Furnace Type	Carrier	SiH_4 Pressure (MPa)	Temperature (°C)	α_{dB} (dB/cm)
B	He	0.979	300 – 500	13.00
B	He	0.100	300 – 400	4.00
D	H_2	1.613	360 – 406	4.00
O	H_2	1.399	315 – 395	3.00
O	H_2	1.310	320 – 395	2.80
O	H_2	3.737	320 – 385	2.60
D	H_2	1.613	360 – 375	2.40
O	H_2	1.206	320 – 394	1.98
O	H_2	1.310	320 – 395	1.75
O	H_2	1.310	320 – 395	1.72
O	H_2	2.647	350 – 360	0.80

Table 3.1: Fabricated 6 μm core a-Si:H fibres

Furnace Type	Carrier	SiH_4 Pressure (MPa)	Temperature (°C)	α_{dB} (dB/cm)
O	He	3.309	350 – 450	60.0
O	He	2.116	300 – 400	44.0
O	H_2	0.276	350 – 375	29.0
O	H_2	2.399	320 – 350	12.0
O	H_2	1.206	100 – 280	9.0
P	H_2	2.427	350 – 380	8.90
B	H_2	0.447	350 – 370	2.90

Table 3.2: Fabricated 2 μm core a-Si:H fibres

of 2 μm core fibres also measured at 1.54 μm. From the fibres fabricated, it is difficult to draw or correlate a relationship between the transmission loss and the deposition conditions due to the multiple variables involved. In the use of high pressure components and vessels, it is very cumbersome to re-pressurise the system in order to keep partial pressures consistent hence allowing for only a few parameters to be analysed. From the fibres characterised, Figure 3.12(a) shows the evolution of the a-Si:H losses in both 6 μm and 2 μm core fibres at 1.54 μm. The small core fibres still possess a higher loss than the frequently fabricated 6 μm core fibres. Fine tuning of the pressures and temperatures will need to be made in order to establish an optimum regime where the fibre-to-fibre loss is consistent to $\sim \pm 2$ dB as is the case for the 6 μm core fibres. In two particular 6 μm core fibres (labeled 'Fibre 1' and 'Fibre 2'), wavelength dependent loss measurements were performed using the cut-back technique. Figure 3.12(b) illustrates the excellent agreement with Rayleigh scattering in the telecom band. With the combined attenuation factors of both the Urbach and Rayleigh mechanisms, the wavelengths closer to the band gap wavelength experience a better fit as predicted by the

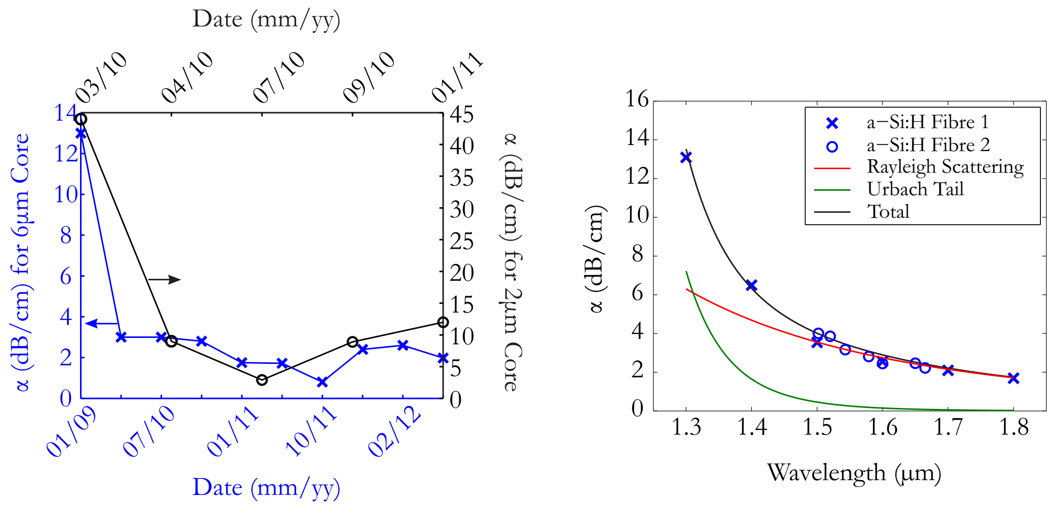

(a)

(b)

Figure 3.12: (a) Evolution of a-Si:H fibre losses since the start of this work. (b) Comparison of two low loss a-Si:H fibres obeying an Urbach and Rayleigh trend.

optical transmission theory described in Section 3.5.3. Interestingly, the fitted Urbach Energy is only a factor of 1.8× larger than the theoretical kT energy, and occurs with less impact than the Rayleigh trend. In contrast to Figure 3.8(a), it is suggestive that these a-Si:H fibres have minimal positive, negative, and neutral charged defect states due to the hydrogenation and that Rayleigh scattering is ultimately what dominates the lowest achievable attenuation.

3.6 Conclusion

A variety of methods exist for the fabrication of semiconductor core, silica cladding fibres. HPCD is a promising tool for the deposition of semiconductors in high aspect ratio capillaries and microstructured templates. The material's phase can be chosen by adjusting the furnace temperature for deposition of amorphous, amorphous-hydrogenated, and polycrystalline semiconductors. The material quality can be controlled by the pressures, precursor concentrations, carrier gas etc. Filled fibres are secured and mounted in thicker capillaries for polishing to prepare them for the optical experiments. a-Si:H is an ideal semiconductor material for optical applications due to the low-cost fabrication process and excellent optical transmission. A number of a-Si:H fibres of two different core diameters have been characterised for linear losses revealing consistency and hence repeatability of the fabrication process.

Chapter 4

Nonlinear Absorption and Modulation in Silicon Fibres

4.1 Introduction

The process of nonlinear absorption refers to an intensity dependent change in a material's optical absorption. This chapter focuses on the photoexcitation of free carriers, in which some fraction of the light incident on silicon is absorbed through two-photon absorption (TPA), creating electron-hole pairs. Photogeneration of carriers causes an additional change in the optical absorption of silicon so that subsequent light is not only attenuated by TPA but also free carrier absorption (FCA). While nonlinear absorption is a material attribute that is commonly perceived as an undesirable effect, it can be exploited to modulate the amplitude of continuous wave (CW) signals using a predefined optical pulse sequence. This process known as cross-absorption modulation (XAM) is presented in the final section of this chapter.

4.2 Nonlinear Absorption Mechanisms

Nonlinear absorption or optical limiting in a material manifests itself as a reduction of its optical transmissivity when the input laser intensity increases. In silicon this should not be confused with saturable absorption but is rather called reverse saturable absorption (RSA) [114]. RSA was the original motivation for developing optical limiters to protect human eyes and optical sensors from high intensity laser radiation [115]. Since the absorption is dynamic and responsive to subpicosecond timescales, it is an efficient technique for high speed optical limitation. The RSA mechanisms of silicon, as already mentioned, are dominated by TPA and in most instances are sequentially followed by FCA.

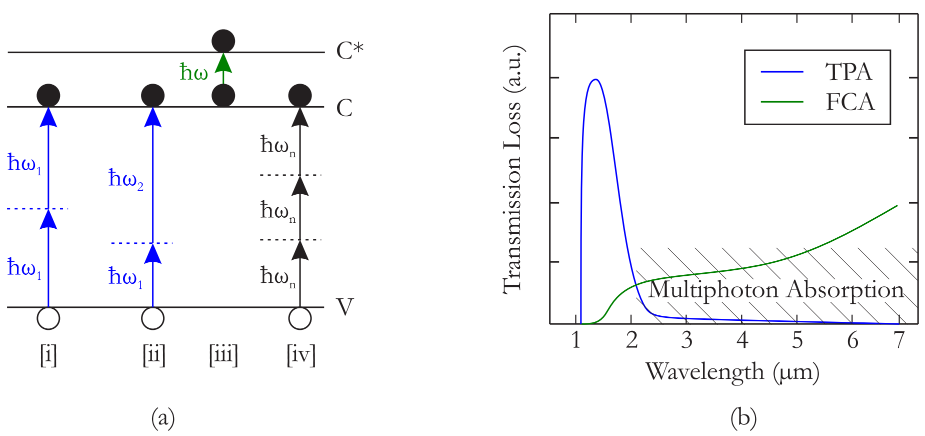

Figure 4.1: (a) Energy level diagrams for degenerate TPA, non-degenerate TPA, FCA, and MPA (b) Predicted nonlinear absorption strength of TPA and FCA.

Figure 4.1(a) is an energy band diagram representing the transitions that carriers undergo when an input photon induces TPA. Process [i] of Figure 4.1(a) shows the degenerate case of TPA. Process [ii] shows non-degenerate TPA occurring with different photon energies whose sum is equal to or higher than the band gap energy of the material. The relative strength of the two-photon based absorption as a function of wavelength is shown in Figure 4.1(b) by the solid blue line. The trend is based on a numerical model for single crystal silicon [116]. As expected, the absorption peaks at wavelengths below half the band gap energy ($\lambda_{\mathrm{bg}/2} = 2.2\,\mu$m) and dramatically reduces thereafter.

Free carriers generated due to TPA exist in a conduction band (C) comprised of a valley of densely spaced energy levels. The separation of the energy levels increases with conduction band energy. Hence, free carriers are more prone to enter a higher unoccupied excited state (C*) with minimal input photon energies since the required excitation energy is so low. This is the underlying reason for the occurrence of FCA and is illustrated by the small excited state transition in process [iii]. By this description, it is expected that FCA is more pronounced at longer wavelengths due to a smaller photon energy. In a separate model of single crystal silicon [33], the trend of FCA with wavelength can also be seen in Figure 4.1(b) where it indeed increases for larger wavelengths. While it may be difficult to induce free carriers via TPA at wavelengths beyond $3\,\mu$m it is possible that multiphoton absorption (MPA) effects may contribute to their generation.

Under certain conditions, MPA may occur through which three or more photons are simultaneously excited to bridge the band gap energy of the material. However, different selection rules exist leading to a probability of occurrence that is highest only in specific wavelength regions. Process [iv] of Figure 4.1(a) represents an example of MPA involving three-photon absorption which can also be of degenerate and non-degenerate forms. Detection methods for MPA typically average a large photon flux, if measuring three-photon based depletion, it can occur in addition to TPA. Hence, for highly sensitive detection methods (such as the Z-scan), care should be taken in calculations of each MPA process to determine whether contributions from other MPA processes have occurred [117].

4.3 Carrier Lifetimes

The recombination lifetime of most electronic devices is not a critical parameter due to the small distances free carriers diffuse over. However, high power components (e.g. transistors), optoelectronic devices, and solar panels require specific control over their carrier lifetimes. The bulky size of these devices can cause carriers to remain mobile for large (nanosecond-microsecond) periods of time, limiting their operating speed and efficiencies. For this reason, industries and many R&D facilities involved in the fabrication of semiconductors use detailed carrier lifetime measurements as a means of process control [118]. Lifetime measurements are ideal for monitoring material performance as they are non-destructive and can reveal deep-level impurities of a semiconductor ingot. These impurities can cause further deterioration and lattice defects as the fabrication process advances. This section focuses on excited state carrier dynamics and investigates the lifetimes of a-Si:H fibres also as a means of process control.

4.3.1 Dynamics

The illustrations presented in Figures 2.4(a), 2.4(b), and 4.1(a), represent an energy band scheme of an ideal semiconductor crystal. Such materials have *delocalized* states of the valence and conduction bands (represented by long solid or dashed lines). Real materials however, have surface defects, bulk impurities, and bond defects, introducing *localized* states which may be populated with carriers. When dealing with an amorphous material like a-Si:H, the structural and bonding defects produce localized states that lie within the band gap energy. States in this region are referred to as *localized gap states* [119]. The carrier lifetime is a sensitive function of the density and distribution of localized gap states. In silicon, several stages of relaxation may occur before a carrier returns to equilibrium. The energy of a carrier may be transferred to other carriers or states and then to the lattice. Different stages entail different time scales at which they occur [120].

Figure 4.2 presents a selected number of carrier excitation and relaxation processes shown in the form of energy-momentum diagrams. The timescales associated with each process are also provided. It is important to be aware of these timescales as they differentiate fast versus slow carrier processes such that a semiconductor can be tailored for specific applications. Figure 4.2(a) shows a simple form of photon absorption producing a free carrier. This may be due to one-photon or multi-photon absorption. It typically takes a carrier $10^{-14} - 10^{-13}$ s to enter an excited state depending on the semiconductor. After photoexcitation, the free carrier can take multiple paths before recombining

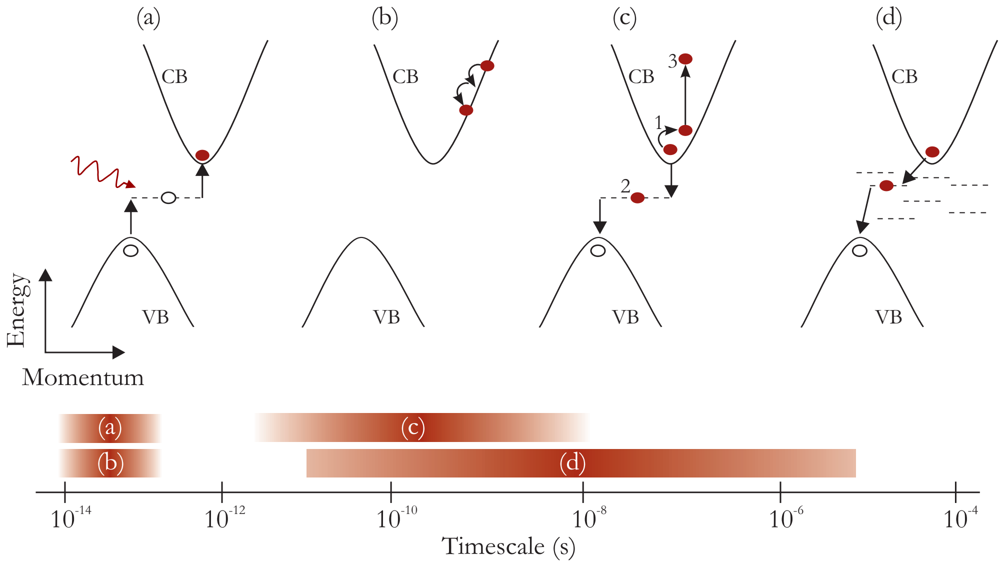

Figure 4.2: Energy-momentum band diagrams showing carrier dynamics. CB is conduction band, VB is valence band. (a) Photo-excitation of a carrier. (b) Thermalisation. (c) Auger recombination. (d) Shockley-Read-Hall recombination.

with its respective hole. In this instance it is possible to neglect radiative recombination since silicon is an indirect band gap material and the crystal momentum mismatch dramatically limits the probability of photon emission.

In Figure 4.2(b), the carrier loses its energy through phonon emission by many transitions within the band in which the energy decrements are small but frequent. This process is referred to as thermalisation and the many inelastic transitions that the carrier undergoes are consequently very rapid with timescales of $10^{-14} - 10^{-13}$ s.

Figure 4.2(c) is known as Auger recombination. It is a 3-step process where the energy of a free carrier is immediately recombined with a hole (2), but rather than emitting its energy by phonon emission it is given to a secondary carrier in the conduction band (1). The second excited carrier (3) may then thermalise back down to the conduction edge. For intrinsic silicon (c-Si) or a-Si:H, Auger recombination is minimal since it is only significant for high carrier concentrations such as heavy doping or intense carrier injection. The multiple steps involved correspondingly result in a slightly larger timescale varying from $10^{-11} - 10^{-8}$ s.

Lastly, Figure 4.2(d) shows Shockley-Read-Hall (SRH) recombination. This form of relaxation occurs more commonly since its relies on impurities and/or material defects. Carriers from the conduction band enter a localized gap state (short dashed lines) where its energy is released in the form of heat. The carrier may then be re-excited to the conduction edge or a hole may enter the same gap state and cause recombination. The rate at which the carrier moves into a gap state depends on the defect energy. Dangling bond defects as described throughout Chapter 3 are an example of the origin of localized states in a-Si:H, and in fact may be beneficial in obtaining faster recombination times. Through SRH it is possible to correlate the optical absorption of a-Si:H to the carrier lifetime assuming process (b) and (c) are minute. Since SRH depends on material purity, recombination times are largely variable with commonly observed durations of $10^{-11} - 10^{-5}$ s.

4.3.2 Measurements

When a material's carrier density is constantly evolving due to non-radiative, radiative, and/or Auger recombination, the optical wave present in the media experiences an optical absorption characteristic of a polynomial relationship [121]. However, in the instance of SRH based recombination the output optical power (P_{out}) decreases at a rate proportional to its input (P_{in}), so that its solution is of the form:

$$P_{\text{out}} = P_{\text{in}} \exp\left(-\frac{t}{\tau}\right), \tag{4.1}$$

where τ is the decay rate or carrier lifetime. To determine the lifetime τ, experiments are designed such that carriers are optically generated in the material and monitored by a secondary optical field called the probe.

The first demonstration of this probe monitoring process in an amorphous silicon optical fibre was performed in 2007 by Won *et al.* [122]. This method used a pulsed pump sequence at a wavelength (532 nm) beyond the band gap energy of silicon, such that each pulse results in the generation of free carriers. The pulses are launched perpendicular to the waveguide's propagation axis to illuminate a large surface area of the core guiding material (a-Si:H). Since each pulse consists of a large number of photons, a similarly large level of carriers is produced. A weak CW probe at 1.55 μm propagates within the core and experiences absorption due to FCA every time carriers are produced. This results in a probe sequence with periodic power depletion. Figure 4.3 is an illustration of this process. The left image shows the a-Si:H fibre being illuminated by a pulsed pump field from the side, while a CW probe enters the core. The three graphs on the right illustrate the pump and probe fields in time and thus the change in carrier density. The carrier density follows a near identical pattern to the pump (assuming the carrier lifetime is equal to or faster than the pump's repetition rate). The regions of FCA correspond to the depletion of power in the probe. The red lines of the probe indicate the exponential tails of the carriers. By fitting this tail to Equation 4.1 an estimate of the carrier lifetime can be established.

In this thesis, lifetime measurements were performed on a number of a-Si:H fibres. However, the experiment implemented differed from the single photon excitation process described in Figure 4.3. Instead, a method of cross-absorption modulation (XAM) was

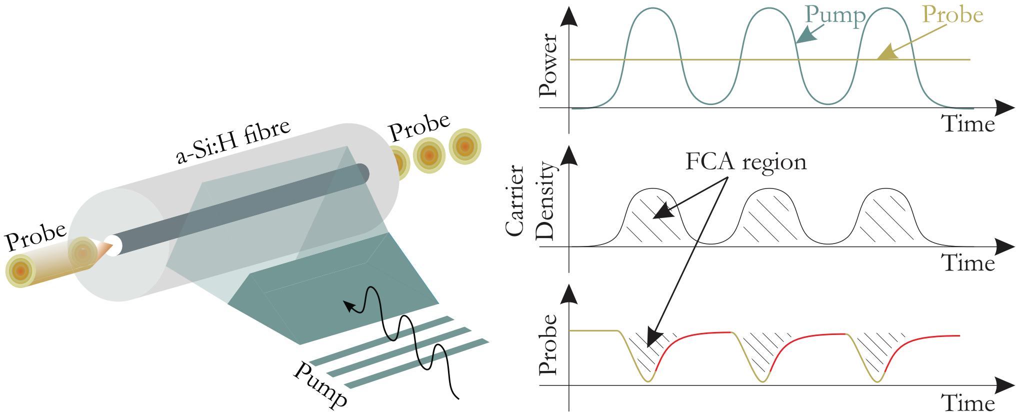

Figure 4.3: Modulation experiment employed by Won *et al.* [122]

used to excite carriers via a two-photon absorption process then the excited state carriers were probed with a CW signal. A detailed outline of the XAM process will be discussed in Section 4.6, though for the purpose of the lifetime measurements only the principles relevant to carrier excitation, photon absorption, and recovery will be presented.

The fundamental difference between XAM and the single photon excitation process is that carriers are now produced only through TPA. This is achieved by the use of a pump consisting of an ultrashort pulse sequence with high peak power at a wavelength below the band gap energy of silicon, but within the two-photon edge (i.e., in the wavelength range $1.1 - 2.2\,\mu$m). The pump source used was a 1540 nm mode-locked erbium fibre laser with 700 fs pulses at a 40 MHz repetition rate. It co-propagates with a weak CW probe centred at 1570 nm. Figure 4.4(a) shows the experimental setup where a preamplifier was used after the CW probe to provide enough power to overcome the losses of the a-Si:H fibre and other external factors such as coupling losses and Fresnel reflections. The focussing and collection lenses employed were antireflection coated fused silica achromatics with 0.4 NA and a 4.6 mm focal length. This arrangement typically provides 0.3 dB of coupling loss and 3 dB of end face reflections due to the high Fresnel reflection coefficients of silicon [123]. The output from the a-Si:H fibre now contains both the pump and the probe waves. The probe wavelength is filtered by using a conventional Bragg grating and circulator configuration. The grating consists of a reflection peak at 1570 nm with a FWHM of approximately 1.5 nm. This bandwidth was chosen such that the increased spectral width due to amplitude modulation of the CW signal is able to be reflected without any form of pulse broadening or filtering. It may appear that the chosen bandwidth of 1.5 nm appears too narrow, since the transform-limited 700 fs pump pulses have a spectral width of 4 nm ($\Delta f \Delta t \approx 0.315$), hence the modulated probe should exhibit a similar bandwidth. However, the relaxation tails due to carrier recovery on the CW probe are elongated over a nanosecond interval, and the amplitude extinction is small enough that the narrow linewidth probe broadened by less than 0.1 nm after

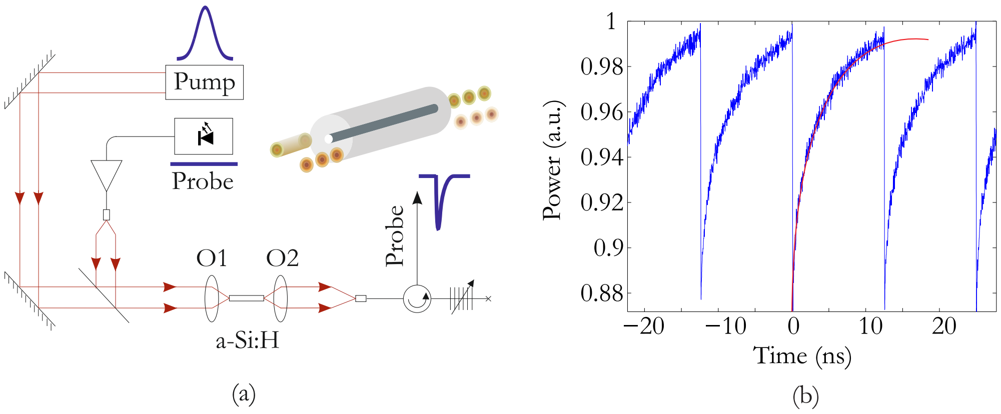

Figure 4.4: (a) XAM experiment for the measurements of the carrier lifetimes. (b) Free carrier absorbed probe pulses as viewed on an oscilloscope.

modulation, as observed on an optical spectrum analyser. The filtered probe is then viewed on a 30 GHz sampling oscilloscope.

When viewed on the oscilloscope, the probe pulses appear as inverted impulse functions. Figure 4.4(b) shows an example of a train of dark pulses imprinted on the probe from XAM. The fibre used in this measurement was a a-Si:H fibre fabricated with a He carrier at $300 - 400\,^{\circ}$C, with a transmission loss of 4 dB/cm. The red line corresponds to the exponentially decaying free carrier tail of interest. Fitting this exponential decay reveals the decay constant τ. However, before fitting, the data is cropped to only expose this tail, and a prebuilt regression analysis tool from Matlab is used to evaluate the decay constant by functional minimisation of Equation 4.1.

Figure 4.5 are plots of the lifetimes measured for four different fibres fabricated under different conditions, extracted at arbitrary sampling times. Fibre related parameters are listed in the caption with the form *"Sample-Type/Carrier Core-Diameter Max-Deposition-Temperature"*. The differences in the carrier lifetimes can be explained as follows. In Figures 4.5(a), (b), and (c), are all 6 μm core diameter a-Si:H fibres which are fabricated at different temperatures. Figure (a) represents typical data for a-Si since the deposition temperature was high enough to minimize the incorporation of hydrogen. By increasing the hydrogen content to decrease the number of dangling bonds, the recombination time will be reduced since the distribution of SRH based recombination sites are further spaced, giving free carriers a larger spatial degree of freedom within the material. The fibres fabricated with He as the carrier gas i.e., (a) and (b) show a much shorter lifetime than that of the H_2 carrier (c). In particular, the decay observed in Figure 4.5(c) was of a much longer duration than the repetition rate of the source laser, therefore the lifetime remains inconclusive at this stage but it is predicted to be on the order of 200 ns.

In Chapter 3, the H_2 carrier based fibres and the effects of hydrogenation were shown to produce fibres with dramatically higher transmission. Hence it is expected that the optical transmission associated with (a), (b), and (c), will decrease inversely with the carrier lifetime. Extracting the transmission measurements from Table 3.1 and Table 3.2 for these fibres, it can be seen that the results do indeed exhibit this trend (i.e., increasing loss for decreasing τ). Presented in Figure 4.5(e) are the carrier lifetimes plotted against the optical absorption, where an additional measurement of a a-Si:H/H 6 μm fabricated at 394 °C fibre is also shown ($\sim$ 3 dB/cm). It is evident that SRH based recombination is dominant in these fibres as the trend in lifetime and absorption imply that high losses correspond to smaller lifetimes.

An important feature that also dictates the carrier lifetime is the physical dimensions of the semiconductor fibre. The surfaces of all materials regardless of their physical form always exhibit the highest number of defects due to an imperfect cleave or cut. Since the deposited semiconductor material in these fibres assume the same surface conditions as the inner walls of the silica capillary, the surface of the semiconductor will produce defected sites in order to form a perfect adhesion (since there is a lattice mismatch between silica and silicon). Therefore a high number of defects are located at the surrounding surface in contrast to the inner volume of the semiconductor. By decreasing the core diameter, the surface to volume ratio is increased thereby circumventing the need to introduce volume defects to achieve shorter lifetime semiconductors. Figure 4.5(d) highlights this point through measurements of the lifetime in a 2 μm core diameter a-Si:H fibre, where τ is 4 ns. More impressively, the loss of this fibre is only 4 dB/cm. The 6 μm core a-Si:H fibre with a comparable loss had a measured lifetime that was more than 20× larger for a 3× difference in cross-sectional area.

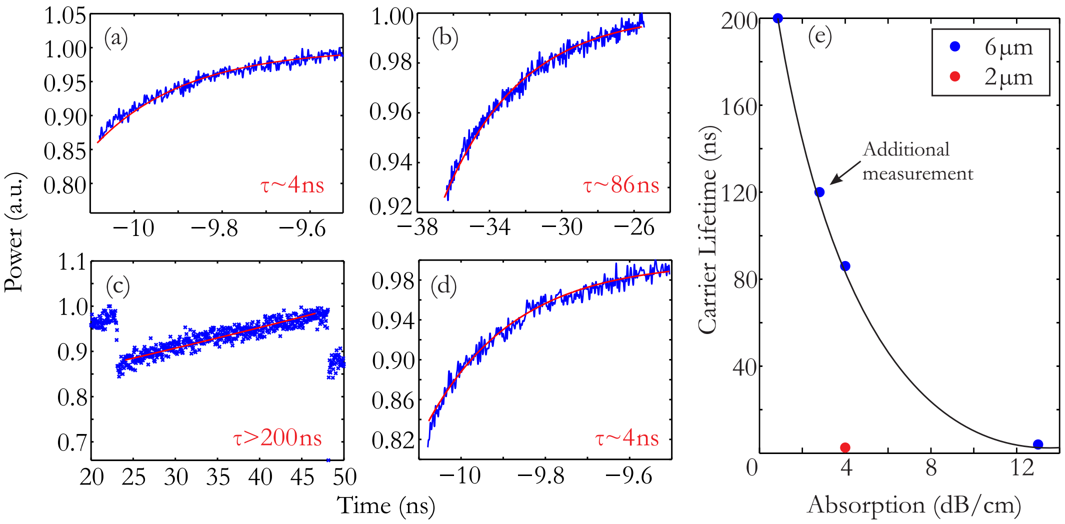

Figure 4.5: Measured carrier lifetimes for fibres described by their *Sample-Type/Carrier Core-Diameter Max-Deposition-Temperature*: (a) a-Si/He 6 μm 500 °C, (b) a-Si:H/He 6 μm 400 °C, (c) a-Si:H/H_2 6 μm 384 °C, (d) a-Si:H/H_2 2 μm 372 °C. (e) Lifetimes and fibre loss relation.

It is apparent that a-Si:H fibres can present a limitation to the repetition rate of the pump source used, which will ultimately limit the operation speed of devices utilising XAM. For high bit rate applications, the lifetime can be reduced by scaling down the core size which is an area of ongoing investigation. Alternatively, previous experiments in nanoscale waveguides have shown that it is possible to reduce the lifetime to a suitable level by using lower pump powers, thereby reducing the density of SRH recombination and allowing thermalisation to contribute more significantly [124]. Thermalisation however, is not considered in this analysis as the recovery occurs on a much shorter time scale and for a much smaller concentration of carriers. Section 4.6 will show this in greater depth where a technique will be described and analysed for recovering the femtosecond dark pulses.

4.4 Simplified Coupled-Mode Equations

a-Si:H optical fibres are a platform for which nonlinear loss coefficients have not been well established. The theory presented in this section describes the model(s) used in obtaining these material specific coefficients such as the TPA and FCA coefficients of a-Si:H optical fibres. The equations and theory already presented in Sections 2.3.2 and 2.3.4 for degenerate TPA, non-degenerate TPA, and FCA, describe the individual processes. However, to accurately model the propagation of light in semiconductors like silicon, a description involving all three processes, the linear optical absorption, and the inclusion of the carrier density's rate of change is required. Effects such as amplitude modulation, carrier decay, and pulse shaping are observable in the temporal domain with strong characteristics. Hence, this chapter is primarily concerned with the temporal characteristics induced on an optical field through nonlinear absorption. The equations presented neglect the effects of spectral modulation which will be introduced in Chapter 5.

For semiconductor fibres where the dispersion length (Equation 2.50) is much longer than the propagation length, it is possible to describe the temporal evolution of a high peak power optical pulse by the following coupled rate equations:

$$\begin{aligned}\frac{dI(z,t)}{dz} &= -\alpha_l I(z,t) - \beta_{\mathrm{TPA}} I^2(z,t) - \sigma_{\mathrm{FCA}} N(z,t) I(z,t) \\ \frac{dN}{dt} &= \frac{\beta_{\mathrm{TPA}}}{2\hbar\omega} I^2(z,t) - \frac{N(z,t)}{\tau}.\end{aligned} \tag{4.2}$$

The TPA coefficient β_{TPA} corresponds to the degenerate case, i.e., $\beta_{\mathrm{TPA}} \equiv \beta_{\mathrm{TPA}p,p}$.

An extension can similarly be applied to the non-degenerate TPA case. In this situation, the three coupled-mode equations that describe the behaviour of the pump field $A_p(z,t)$, signal (or probe) field $A_s(z,t)$, and the carrier density $N(z,t)$ are [54]:

$$\begin{aligned}
\frac{\partial A_p}{\partial z} &= -\frac{\alpha_l}{2}A_p(z,t) - \frac{\sigma_{\text{FCA}}}{2}N(z,t)A_p(z,t) - \frac{\beta_{\text{TPA}p,p}}{2}I_p(z,t)A_p(z,t), \\
\frac{\partial A_s}{\partial z} &= -\frac{\alpha_l}{2}A_s(z,t) - \frac{\sigma_{\text{FCA}}}{2}N(z,t)A_s(z,t) - \beta_{\text{TPA}p,s}I_p(z,t)A_s(z,t), \\
\frac{dN}{dt} &= \frac{\beta_{\text{TPA}p,p}}{2\hbar\omega}I_p^2(z,t) - \frac{N(z,t)}{\tau}.
\end{aligned} \tag{4.3}$$

An important feature of these equations can be seen through the non-degenerate two-photon based absorption term, which shows that the absorption due to this form of TPA is 2× stronger than that of degenerate TPA. Though it should be noted that degenerate TPA is influenced by the product of the pump intensity and amplitude $I_p(z,t)A_p(z,t)$, which is significantly stronger than the product $I_p(z,t)A_s(z,t)$. If however, the fields were of equally high intensity, then these equations are no longer suitable as the approximation assumes that the probe field is much weaker than the pump and is therefore not strong enough to induce FCA through TPA. This is shown in the carrier rate equation where only the degenerate TPA term is included.

These assumptions are specific to the conditions of the experiments conducted in the following sections. Equations 4.2 will be used to fit experimentally measured nonlinear absorption measurements of several silicon optical fibres, with the TPA and FCA coefficients as fitting parameters. Functional minimisation of this 2-parameter fit will yield the best coefficients corresponding to a particular fibre. Equations 4.3 will be used to demonstrate non-degenerate TPA in a similar manner to that already described in Section 4.3, with the addition of ultrafast measurements to reveal the high speed nature of TPA.

4.5 Nonlinear Absorption Strength and Cross-Sections

This section focuses on the experimental and associated numerical work performed in establishing the TPA and FCA coefficients for a-Si:H core fibres. The analysis is based on numerical fitting of the experimental measurements via Equation 4.2 with β_{TPA} and σ_{FCA} left as free parameters. The experimental setup is based on Figure 4.4(a), without the requirement of a probe signal or output filter.

A pulsed pump source is launched into a a-Si:H fibre where the input power is varied and the output power is correspondingly recorded. The relationship between the two measured parameters produces a nonlinear curve as the input power is increased. From Equation 4.2, the input optical field envelope needs to be known precisely in order to simulate the extent of linear absorption, TPA, and FCA. The high power pulses were generated by an erbium fibre laser mode-locked to produce 720 fs (FWHM) pulse

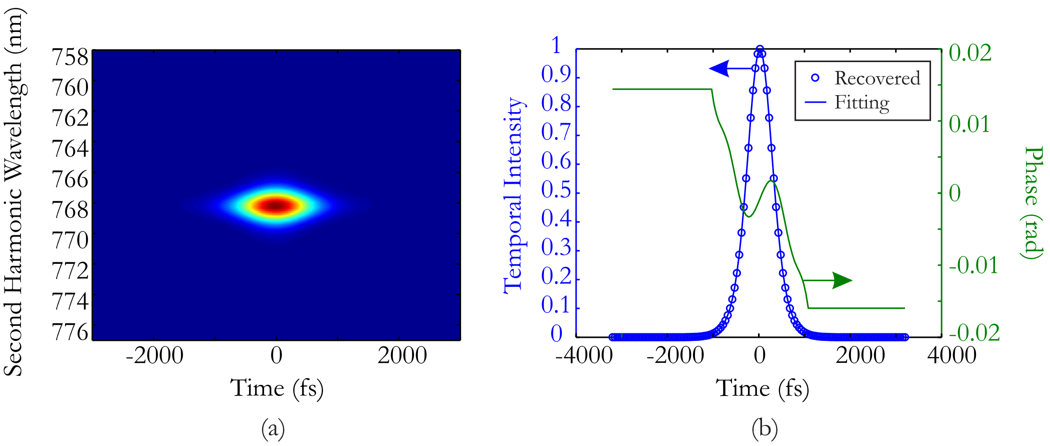

(a) (b)

Figure 4.6: (a) Raw spectrogram of pump source. (b) Recovered temporal pulse and phase of pump.

durations, operating at 1540 nm with a repetition rate of 40 MHz. Since the ultra-short nature of the pulse operates at a time scale far beyond current radio frequency (RF) instruments, the pulse characteristics such as the FWHM, envelope shape, and time-bandwidth product (TBP) were measured using a commercial Southern Photonics (HR150) frequency-resolved optical gating (FROG) system. The FROG instrument uses the pulsed source to 'measure itself' by manually delaying it through an identical reference arm. The two arms are used to produce a second harmonic spectra (using a frequency doubling crystal) as a function of delay. A spectrogram is produced showing the spectra for each temporal delay as shown in Figure 4.6(a). Using a sophisticated iterative phase retrieval algorithm, the software processes the spectrogram, and attempts to construct the shape and phase of the optical pulses. Due to the numerical nature of the recovery process, a retrieval error is also produced which indicates a 'goodness of fit'. The retrieval error defined by the Southern Photonics software is the RMS difference between the measured spectrogram and the retrieved spectrogram. Any value below 1×10^{-5} is considered a reliable recovery. Figure 4.6(b) is the recovered envelope and phase of the pulses from the erbium fibre laser. The pulse width is revealed to be $\sim$ 720 fs, with a TBP of $\sim$ 0.331. This is close to the TBP for a bandwidth-limited sech^2-shaped pulse, and the solid blue line indicates a near perfect fit of the recorded envelope to a sech^2 pulse. The retrieval error is 1.04×10^{-6} indicating good convergence of the recovery with respect to the raw spectrogram. By using this pulse information in the numerical fitting of the experimental measurements, the errors in the solutions to the nonlinear absorption coefficients are minimized.

In the experimental setup, microscope objective lenses used for input coupling and collection are the same as that shown in Figure 4.4(a). Two cameras were used in this experiment. One images the back-reflection from the input a-Si:H fibre facet, and the other images the output end face of the fibre. The cameras assisted in optimising the

Fibre	Core Diameter (μm)	Furnace Type	Carrier	SiH_4 Pressure (MPa)	Temperature (°C)	α_{dB} (dB/cm)	Carrier Lifetime (ns)
A	6	B	He	0.100	300 – 400	4.00	86
B	6	O	H_2	1.310	320 – 395	1.72	120
C	6	O	H_2	2.647	350 – 360	0.80	200
D	2	B	H_2	0.447	350 – 370	2.90	4

Table 4.1: a-Si:H fibre specifications.

launch into the core. The input power was varied using a conventional graded neutral density silica attenuator, and the optical powers were measured using a calibrated Newport germanium photodetector (model 818-IR).

Four particular a-Si:H fibres were investigated. Three of which have 6 μm core diameters (with one fabricated using a He carrier), and the fourth has a 2 μm core diameter. For simplicity, each fibre is labeled *Fibre A*, *Fibre B*, *Fibre C*, and *Fibre D*. The details of the corresponding fibre fabrication parameters and characteristics are shown in Table 4.1.

The process of numerically fitting a set of partial differential equations to raw experimental measurements is, in most cases, cumbersome and inaccurate due to poor convergence. Amongst many reasons, these problems arise due to the simplifications made in the theory and the spread of experimental measurements result in scaling problems. However, numerically determining the exact output power after certain propagation parameters is not the intention. Nonlinear absorption is predominantly seen as a modification to the rate of change of the output power with respect to the input power. Therefore, by normalising the experimental and numerical output powers the issues of prolonged and inaccurate convergence can be mitigated. After the normalisation, the functional form of the data and resulting goodness of fit statistics do not change [125]. Figure 4.7(a) shows the nonlinear absorption measurements of Fibre A numerically fitted to Equation 4.2. This fibre measured 1.2 cm in length and the normalisation factor of the output power is 32 W, hence the maximum output peak power is 32 W. This results in a maximum attenuation of $\sim$ 10 dB (at 300 W input peak power). Since the linear loss from Table 4.1 is 4.8 dB, the amount of nonlinear absorption corresponds to an additional 5.2 dB. In Figure 4.7(a) the fitted parameters were separated into the loss components of linear loss and TPA. The curvature of the total fit further confirms the deviation from linearity of the optical transmission in a-Si:H fibres. From this fitting the following two parameters were established; $\beta_{\mathrm{TPA}} \sim 8 \times 10^{-12}$ m/W and $\sigma_{\mathrm{FCA}} \sim 1 \times 10^{-20}$ m^2. The TPA coefficient is similar to values reported for a-Si:H planar waveguides [126, 127] though this varies depending on the material properties, with reports ranging from $0.8 \times 10^{-12} - 41 \times 10^{-12}$ m/W [128]. As a comparison, waveguides fabricated from c-Si typically have β_{TPA} in the range of $5 \times 10^{-12} - 9 \times 10^{-12}$ m/W [129, 130], making a-Si:H also a potential material for TPA based applications (such as optical limiters). It is also important to note that the band gap energy of a-Si:H is $\sim$ 1.7 eV corresponding to a

TPA edge of ~ 1.46 μm. Yet the results presented show significant TPA even at 1.54 μm. This is attributed to the amorphous nature of the material where we expect the band tail to be elongated, and hence leading to a smearing of the TPA edge.

When calculating the FCA coefficient from the Drude-Lorenz model Equation 2.44, this yields $\sigma_{\mathrm{FCA}} = 1.6 \times 10^{-20}\,\mathrm{m}^2$ which is slightly larger than our estimated value. The difference in this result may be attributed to the quality of the deposited material or the assumptions surrounding the idealised electron model the Drude-Lorenz theory is based on. In addition to these reasons, a margin of error in the FCA coefficient is expected, especially since we are operating in a low input power regime where the true cubic behavior of FCA is unnoticeable. In turn, this impacts the functional misfit error of σ_{FCA}.

To demonstrate how the carrier density varies as a function of the input pulse, Figure 4.7(b) shows the evolution of $N(z,t)$ as a function of the input peak power and temporal envelope. From the established coefficients, it is possible to generate a fairly accurate model of how this carrier density varies. Due to the high peak power and ultrashort nature of the input pulses, the carrier concentration rapidly reaches a saturation point at positive times corresponding to the trailing edge of the pulse. Carrier recombination or recovery is not visible here due to the chosen temporal span (picoseconds as opposed to nanoseconds).

The two lowest loss a-Si:H fibres fabricated with a hydrogen carrier gas reveal the best fits as shown in Figure 4.8(a) and (b). Fibre B measured 1.5 cm and also yields a $\beta_{\mathrm{TPA}} \sim 8 \times 10^{-12}\,\mathrm{m/W}$ and $\sigma_{\mathrm{FCA}} \sim 1 \times 10^{-20}\,\mathrm{m}^2$. The normalization factor is 40 W, hence the maximum absorption was ~ 10.8 dB, resulting in a total induced nonlinear absorption of 8.2 dB.

However, when investigating Fibre C (3 cm), a a-Si:H fibre with a dramatically lower loss, then $\beta_{\mathrm{TPA}} \sim 5 \times 10^{-12}\,\mathrm{m/W}$, while the σ_{FCA} also remains the same as the others.

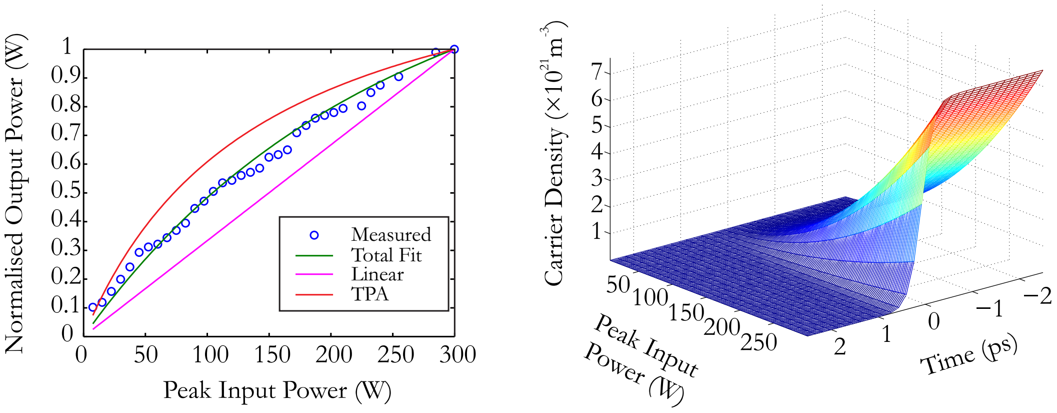

(a) (b)

Figure 4.7: Fibre A. (a) Nonlinear absorption. (b) Carrier density.

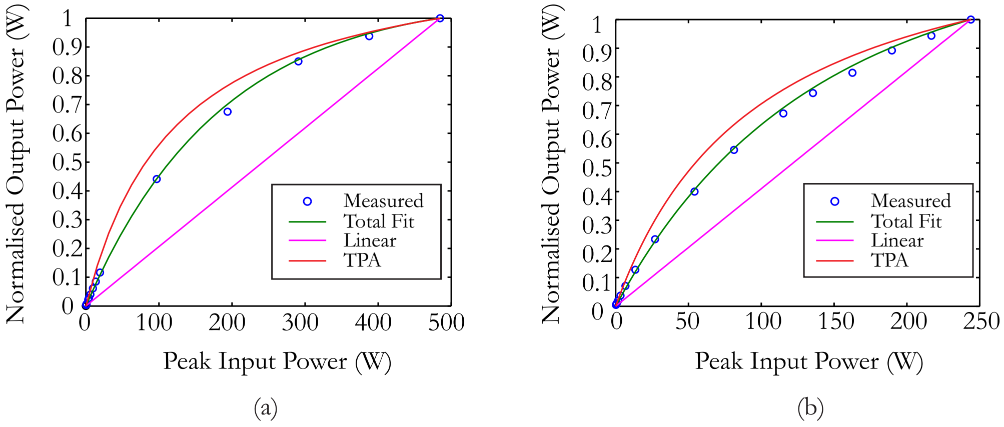

Figure 4.8: Nonlinear absorption in (a) Fibre B and (b) Fibre C.

The differences in the TPA coefficient may be attributed to the material quality, though further investigations are required since this value has not yet been repeated in other a-Si:H fibres. The maximum output peak power here is 20 W which yields a higher maximum nonlinear absorption of 11 dB. The total induced absorption is then 10.2 dB.

Fibre D of Figure 4.9 is the smaller core fibre. Owing to the high coupling losses associated with the small core fibre, a peak coupled input power of only 18 W was achievable. However, this was sufficient to observe nonlinear absorption. From Figure 4.9(a), the normalised peak output power was 3.5 W which corresponds to a maximum nonlinear absorption of 7 dB. The total induced nonlinear absorption is thus a modest 4.1 dB. The coefficients in this case were found to have a slightly larger TPA of $\beta_{\text{TPA}} \sim 8.3 \times 10^{-12}$ m/W and the FCA coefficient was again found to be the same as before with $\sigma_{\text{FCA}} \sim 1 \times 10^{-20}$ m^2. The re-occurring values obtained for the FCA is expected as the Drude-Lorenz model is described as a function of dielectric and electron-hole constants such as the electronic rest mass and carrier mobility. This material dependent

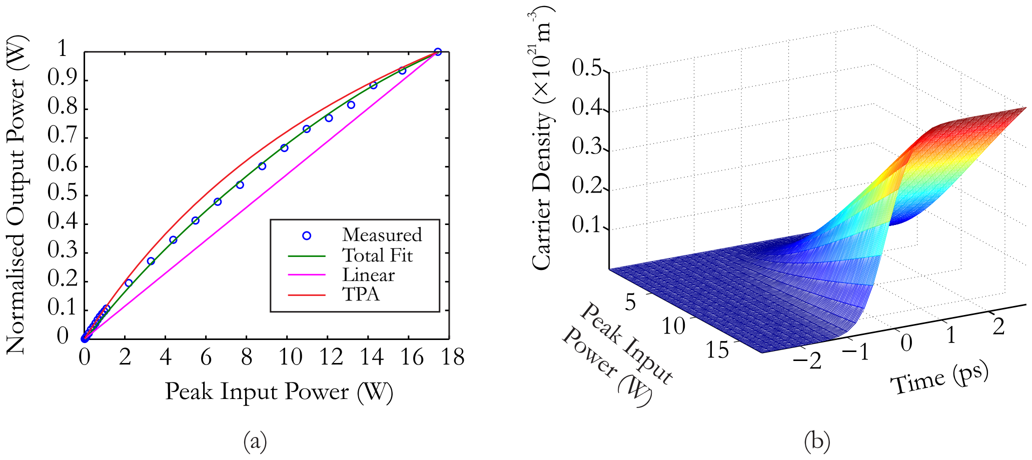

Figure 4.9: Fibre D. (a) Nonlinear absorption. (b) Carrier density.

Fibre	β_{TPA} (m/W)	σ_{FCA} (m^2)	Induced Nonlinear Absorption (dB)
A	8×10^{-12}	1×10^{-20}	5.2
B	8×10^{-12}	1×10^{-20}	8.2
C	5×10^{-12}	1×10^{-20}	10.2
D	8.3×10^{-12}	1×10^{-20}	4.1

Table 4.2: Nonlinear absorption coefficients measured for the a-Si:H fibres.

constant should be consistent in all the amorphous fibres since they are formed from the same material composition and fabrication process.

The carrier density associated with the small core fibre (Fibre D), exhibits a similar trend whereby saturation is reached at the trailing edge of the pump pulse. Though in Figure 4.9(b) the carrier density builds up to a lower saturation point owing to the lower coupled input powers.

A summary of the established coefficients for each of the four fibres, and the total induced nonlinear absorption is presented in Table 4.2. These measurements represent the first nonlinear characterisations performed in a-Si:H optical fibres. They provide additional details of parameters required for the GNLSE allowing for the nonlinear propagation model to represent a a-Si:H fibre more accurately.

From the nonlinear curves presented in Figures 4.7-4.9, it can be concluded that TPA plays a significant role in the nonlinear absorption. Since TPA can be a non-degenerate process, the nonlinear absorption can also be induced on a co-propagating wave of a different wavelength (the probe). Effectively, a pump pulse sequence can be used to induce a sequence of absorption dips on the probe, causing periodic optical power depletion. This form of absorption modulation was investigated and will be discussed in the following section.

4.6 All-Optical Modulation

One particular silicon based switching device was based on the plasma dispersion effect [131]. In this device, a pulsed pump at wavelength λ_p having a photon energy $h\nu_p$ greater than the band-gap energy E_g, was used to produce excess free carriers inside the waveguide whilst in the presence of a secondary CW probe signal λ_s whose energy was $h\nu_s < E_g$. At the peak of each pump pulse, generated free carriers absorb photons in the CW signal creating dark pulses or equivalently an inverted imprint of the pump on λ_s. This form of modulation was illustrated in Figure 4.3. However, due to the strong pump photon energy, free carriers are excited into deep conduction band states leading to additional delays in the carrier lifetimes. Unfortunately such carrier-injection modulation schemes, whether excited optically or via an external current, are limited in response speed to the effective free carrier lifetime which typically ranges from hundreds of picoseconds in nanoscale silicon wires, to hundreds of nanoseconds in micron-sized waveguides [132]. Alternatively, a more restricted excitation of free carriers to the lower conduction states can be induced by TPA, where each photon is provided by a pulsed pump and CW probe, both having energies below E_g. As in Section 4.3.2, depletion in the CW probe from photon absorption results in an inverted imprint of the pump.

Cross-absorption modulation (XAM) is an entirely passive optical process. The pump source is comprised of a predefined pulsed sequence with modest peak powers and operates at a wavelength λ_p with a photon energy E_p between the band gap and half band gap energy of the material i.e., $E_g/2 \leq E_p < E_g$. The probe is the source onto which an inverted pump sequence is imprinted. This is usually a CW laser whose wavelength λ_s should obey the same conditions as the pump λ_s (i.e., $E_g/2 \leq E_s < E_g$) with average powers typically in the order of several milliwatts. The process involves co-propagating the two waves within the silicon waveguide with the requirement that $E_p + E_s > E_g$. The high peak power of the pump pulse initiates TPA where the second photon is absorbed from the CW source λ_s. Absorption of these photons will lead to two direct consequences; power depletion in the probe during the peak of the pump pulse, and the generation of free carriers. The former is intrinsically an ultrafast process [133], while the latter is a slow process that will further attenuate both optical fields via FCA [124]. When considering the effects of XAM, attention must be paid to the temporal domain of the probe wave in order to characterise the absorption strength and profile. An experiment is designed and performed to observe XAM. A full characterisation of the experimental measurements using the coupled-mode equations of Equation 4.3 will be presented.

4.6.1 Continuous Wave Cross-Absorption Modulation (CW XAM)

The initial demonstration of XAM was performed using the experimental setup of Figure 4.4(a) in Section 4.3, where the output Bragg grating was tunable. The pump and probe pulses at the output of the a-Si:H fibre were then observed on an electronic 30 GHz sampling oscilloscope as shown in Figure 4.10(a). The pulses appear as impulse response functions of the oscilloscope's detector since the femtosecond pulses operate with a far higher bandwidth. The red line indicates the CW field in the absence of the pump such that no TPA-induced modulation is present. With the pump present (green curve), the blue curve shows the CW field being modulated with an impulse response that is inverted with respect to the pump pulse. This indicates that a dark pulse equivalent has been induced on the CW field confirming TPA modulation. As the modulated probe recovers, it can be seen that the floor is lower than the original unmodulated CW probe. This deviation is due to free carrier recombination as discussed in Section 4.3. The probe's

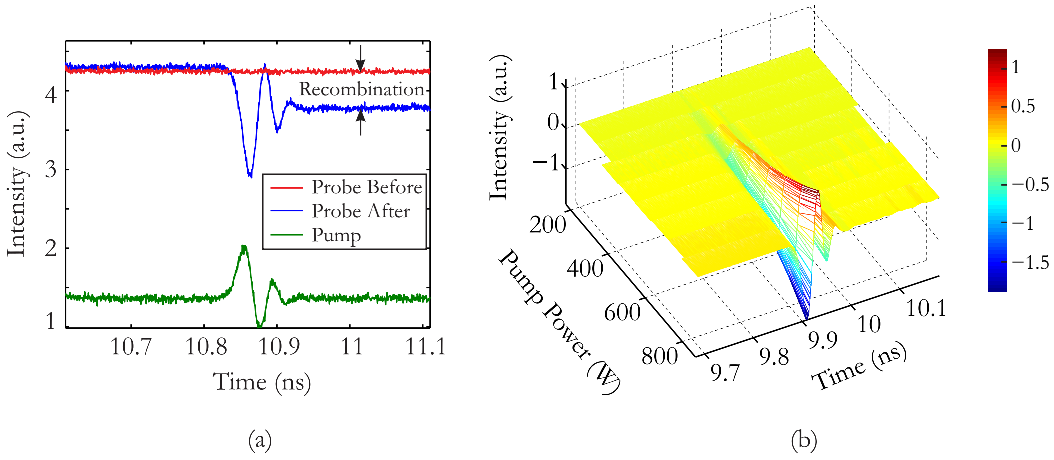

Figure 4.10: (a) Pump and probe pulses from the first XAM experiment. (b) Variation of probe modulation as a function of pump power showing a nonlinear decrease.

response was also measured as a function of the pump power. From the description in Section 2.3.2.2 of TPA effects on a CW probe, it was shown in Equation 2.42 that the output signal intensity $I_s(z,t)$ depends on a power-law relationship of the pump $I_{0p}(t)$ on the degenerate and non-degenerate TPA coefficients. This relationship can be seen in Figure 4.10(b) where the dark probe pulses follow a geometric decay in amplitude as the pump power is decreased into the a-Si:H fibre. The modest extinction of the dark pulses shown on the oscilloscope (though masked by the impulse response) is $\sim 1-2\,$dB. Extinction ratios of this order renders ultrafast pulse measurement techniques such as the FROG unfeasible, since the peak power is insufficient to induce nonlinearity. Thus, an experiment is required such that the full form of the dark pulse is recoverable.

4.6.2 Pump-Probe Technique

Nonlinear spectroscopists often use a method based on pump-probe techniques to obtain parameters of a material through the effects observed on a probe [134]. This method is capable of achieving a high temporal resolution when combined with lock-in detection. In this process a pump pulse excites the sample and triggers the process under investigation (i.e., TPA). A second delayed pulse ‘the probe’, monitors the TPA process [135–137]. By varying the time delay between the pump and probe pulses, it is possible to acquire controlled measurements of the TPA process as a function of time. The probe pulse is typically a small fraction of the pump pulse exciting the process, or may involve a different wavelength pulse (non-degenerate) of similar duration and repetition rate.

When the two beams (pump and probe) propagate in their respective arms, a method is required to view the displacement between the femtosecond pulses in order to achieve the correct delay length such that the pump and probe can be temporally aligned. This

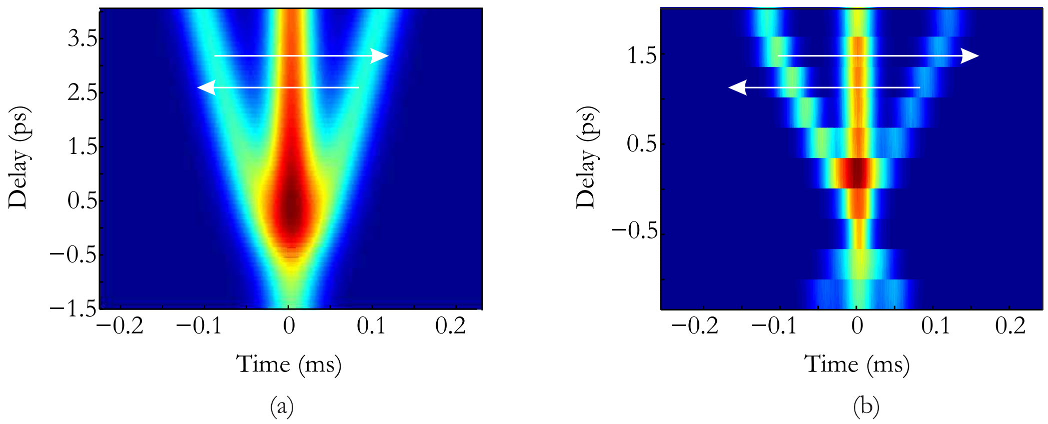

Figure 4.11: (a) Autocorrelation simulation of two secant hyperbolic pulses. (b) Experimental autocorrelation traces of the two secant hyperbolic pulses.

was best performed by use of an FR-103XL autocorrelator. An optical autocorrelator is a highly simplified form of a FROG instrument, whereby the temporal signal is detected using a time-averaged photodetector while the reference arm's delay is continually displaced by a predefined temporal window. The method allows real-time observation of an ultrafast optical pulse via a conventional oscilloscope where the pulse is magnified in time. The magnification is proportional to the repetition rate of the autocorrelator's delay line. To visualise how the optical autocorrelation of two coinciding pulses would look like on an oscilloscope, a simulation was performed on two 700 fs pulses where the second pulse was significantly weaker in intensity. Figure 4.11(a) shows the simulation result of the pulses as a function of delay. A delay of 0 ps indicates the pulses are overlapped in time. As the probe pulse is delayed in time, wings appear symmetrically about the central autocorrelation peak which continue to spread as the delay is increased. Using a retroreflector mounted on an electronic delay line, the probe was delayed through the stationary pump pulse and the autocorrelation behaviour was experimentally confirmed as shown in Figure 4.11(b). The result is produced from a 12 GHz real-time oscilloscope that was connected to the FR-103XL autocorrelator. The true (unmagnified) temporal spacing depends on the autocorrelator (and pulse shape if measuring the FWHM). For Figure 4.11(b) the unscaled time τ_r [s] is:

$$\tau_r = 32 \times 10^{-9} t_o, \tag{4.4}$$

where t_o [s] is the oscilloscope's time. Calculation of the pulse FWHM requires an additional multiplication factor known as the deconvolution factor [138].

The pump-probe technique becomes a powerful tool when combined with lock-in detection or amplification. It is a widely employed method for measuring low level optical signals by modulating the probe source then recovering the signal at that modulation frequency while all other frequency components are rejected. This provides an enhancement in sensitivity, dynamic range, resistance to background noise, and measurement

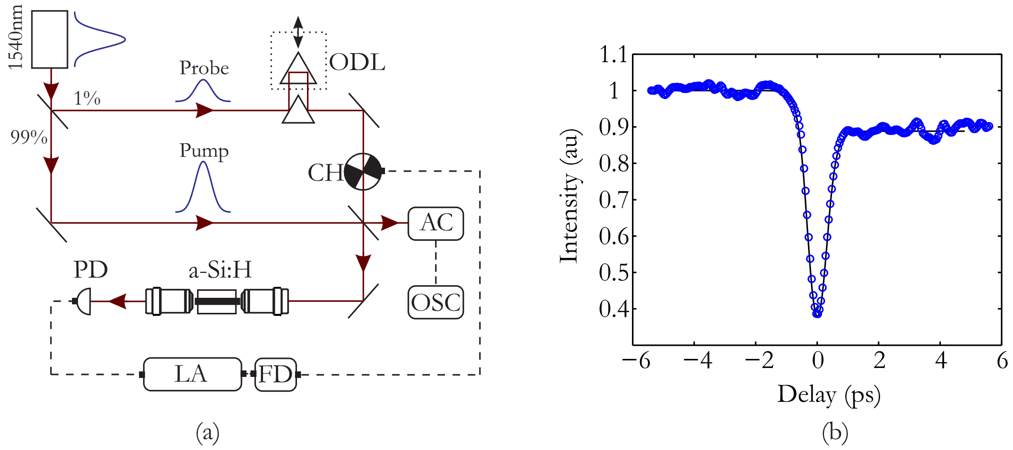

(a) (b)

Figure 4.12: (a) Pump-probe experiment for degenerate TPA based modulation. (ODL) Optical delay line, (CH) chopper, (AC) autocorrelator, (OSC) oscilloscope, (PD) photodetector, (LA) lock-in amplifier, (FD) frequency driver. (b) Recorded absorption on pump (circles) with numerical fit (solid line) from preestablished parameters.

resolution. The probe is amplitude modulated with a chopper (CH) that is driven by a highly stable closed-loop frequency driver (FD) at 130 Hz. The frequency driver simultaneously serves as a frequency reference to a Perkin Elmer 7225 lock-in amplifier (LA). The amplifier performs real time digital signal processing of a photodetector's (PD) signal, filtering frequency components outside of the reference. By measuring the average power of the chopped signal as a function of delay, the dark pulse can be obtained with a high temporal resolution. The signal-to-noise ratio and response of the recording depends on the steepness of the internal filter (dynamic for the 7225) and integration time (set to 200 ms).

The experimental configuration employing the lock-in technique is shown in Figure 4.12(a), where the 6 μm core a-Si:H fibre under investigation measured 2 cm in length and had a linear loss of 1.7 dB/cm at 1540 nm. In this experiment only a weak component (1 %) of the 1540 nm femtosecond source was used for a probe pulse. The double prism arrangement signifies the retroreflector mounted on a delay line whose speed is controlled by an injected electrical current. Both pump and probe are simultaneously viewed on the autocorrelator-oscilloscope configuration and launched into the a-Si:H fibre. The attempt to measure degenerate TPA on the probe serves as a control experiment for:

1. Ensuring the parameters of the instruments are correctly calibrated to:
    (a) The lock-in acquisition time versus the ODL scan time
    (b) Amplitude fluctuations in the probe due to vibrations induced from the motorised ODL
    (c) Stabilize the chopping frequency to the frequency driver output

   (d) Operate at a sufficient rate such that the measurements are not affected by drifts in the free-space alignment

2. Establishing a numerical fit of Equation 4.3 using the pre-established coefficients and parameters thereby justifying the original characterisation methods.

3. Demonstrating the ultrafast response of TPA.

With a peak pump power of 250 W and a peak probe power of 10 mW coupled into the a-Si:H fibre, the absorption of the probe as a function of delay is plotted in Figure 4.12(b). Negative time delay indicates the probe pulse propagating ahead of the pump and vice versa for positive time delays. The curve clearly shows an ultrafast response due to TPA followed by rapid carrier recovery (thermalisation mechanisms) before slower recombination takes place (SRH) [139, 140]. Solving Equation 4.3 with the parameters initially established for this a-Si:H fibre (Fibre B) produces an excellent agreement to the data as shown by the solid line in Figure 4.12(b). The FWHM of the absorption is ∼ 800 fs, which is slightly broader than the original 700 fs pump pulse. The exact reason for this broadening is unclear. It is clear, however, that dispersion is not a factor. This can be shown by the broadening factor of a pulse [15]:

$$\mathrm{BF} = \left[1 + \left(\frac{\pi \beta_2 L}{6\sigma_0^2}\right)^2\right]^{\frac{1}{2}} \tag{4.5}$$

where the root-mean-square (RMS) width of a sech^2 pulse is,

$$\sigma_0 = \frac{\pi T_{\mathrm{FWHM}}}{2\sqrt{12}\ln(1+\sqrt{2})}. \tag{4.6}$$

Using a calculated GVD for c-Si as an approximation ($\beta_2 \sim 0.9847\,\mathrm{ps}^2/\mathrm{m}$) over a propagation length $L = 2\,\mathrm{cm}$, then the broadening factor is $\mathrm{BF} \sim 1.0032$. Thus, this is insufficient to introduce a noticeable spread in the pulse so it is fair to conclude that the broadened measurement may be an inherent property of the TPA process.

The TPA coefficient is also a parameter that is known to strongly influence the extinction ratio of the absorption. In Figure 4.12(b) the extinction was measured at ∼ 4.5 dB. A slight margin of error exists in this quantity as the lock-in technique cannot discriminate pump and probe pulses operating at the same wavelength but only those at a particular repetition rate (130 Hz→ 8 ms). Due to the much higher repetition rate of the source (40 MHz→ 25 ns), multiple pump pulses fall within the chopping frequency causing an absorption measurement that is representative of both probe and pump.

Property	Units	Value
Length	km	0.50
Loss	dB/km	3.45
Dispersion	ps/nm/km	-0.75
Dispersion Slope	ps/nm^2/km	0.0031
A_{eff}	μm^2	9.7
γ	1/W/km	20

Table 4.3: Highly nonlinear fibre properties characterised at 1550 nm.

4.6.3 Non-Degenerate XAM

The investigation of non-degenerate XAM in the form of a pump-probe method requires two pulse trains operating at the same repetition rate but different wavelengths. OPO's would appear as an ideal source system, however, obtaining a system with high temporal pulse stability is rare or costly due to the complexity of stabilising fluctuations in the oscillator's cavity (due to thermal or vibrational effects). Instead, the method employed here uses a portion of the optical power from the 700 fs pulse source, which is launched into a highly nonlinear fibre (HNLF) to generate a continuum through optical nonlinearity. The characteristics of the HNLF are given in Table 4.3 with a nonlinear strength γ that is 20× stronger than conventional SMF28 fibre. A bandwidth-tunable variable wavelength filter (BVF) is added to the output of the HNLF to select a wavelength and pulse duration from this continuum. This pulse forms the probe and is recombined with the pump as before.

Inserting 0.5 km of optical fibre in a configuration that requires temporal alignment to an external beam (the pump) exhibits undesired effects due to changes in the environment. The thermal expansion coefficient of silica is modest, though the long length of the HNLF causes a strong response in the fibre's optical path length with minor changes in the surrounding temperature. Figure 4.13 shows three infinite-persistence oscilloscope traces that demonstrate the behaviour of the probe pulses under different thermally agitated scenarios. In Figure 4.13(a), the HNLF is placed in the vicinity of the lab's air-conditioning system. The low temperatures cause thermal contraction of the fibre, decreasing the fibre length, and hence causing the optical pulse to be negatively delayed. The red curve shows an approximate location of the initial pulse while the green area traces the pulse as it moves in the $-t$ direction indicating an earlier arrival. Figure 4.13(b) is a 10 min persistence trace of the probe pulse in an environment where the temperature is regulated to a constant level. The HNLF is still able to experience thermal expansion and contraction causing the pulse to drift by a total of 10 ps. This still poses an issue to the XAM experiment as a single acquisition point may take ~ 1 sec, resulting in a ~ 17 fs temporal drift. This 2 % error in time is accumulated over a vast number of points causing obscured measurements. Finally the HNLF was inserted into a thermally isolated expanded polystyrene container filled with packaging material ("peanuts") to restrict air flow. Figure 4.13(c) now shows the pulse measured over 30 mins where the approximate mean trace is the centred red curve, indicating good pulse stability.

After producing a stable probe pulse, the output spectra of the HNLF was measured and is shown in Figure 4.14(a), with the inset showing a picture of the HNLF buried under polystyrene peanuts. The BVF was set to a wavelength of $\sim 1572\,\text{nm}$ and the linewidth was set to the instrument's maximum limit, producing 1 ps pulses as measured on the autocorrelator. The filtered spectra can be seen in Figure 4.14(b) where it was ensured that pump pulse spectrum did not overlap with the probe to avoid contamination of pump energy in the TPA measurement.

The final experimental setup is illustrated in Figure 4.15(a). The probe arm is modified to include the HNLF and BVF and proceeds through a similar arrangement as in Figure 4.12(a). The output of the a-Si:H fibre is incident on a blazed diffraction grating (DG) followed by a pinhole so that only the probe wavelength to enter the photodetector. When linked with the lock-in system, three different pump powers were used to measure the modulation. The absorption of the probe influenced by the three pump powers is plotted in Figure 4.15(b). Reasonable fits were obtained using Equation 4.3 where $\beta_{\text{TPA}p,s}$ was a free parameter. The non-degenerate coefficient was revealed to be $\beta_{\text{TPA}p,s} \sim 4.9 \times 10^{-12}\,\text{m/W}$ for all three pump power fittings, justifying the consistency and accuracy of each absorption measurement. The absorption measurements also produced an unusual feature in the measurements. At high pump powers, an elongated carrier relaxation feature was present, that was not reproduced by simulations. The precise cause of this elongation is not currently known, though it could be due in part to the difference in the pump-probe pulse widths (and symmetry) and/or certain carrier dynamics.

The modulated absorption width in this experiment was measured to be $\sim 1.1\,\text{ps}$ for all three measurements, indicating only a minor temporal broadening relative to the

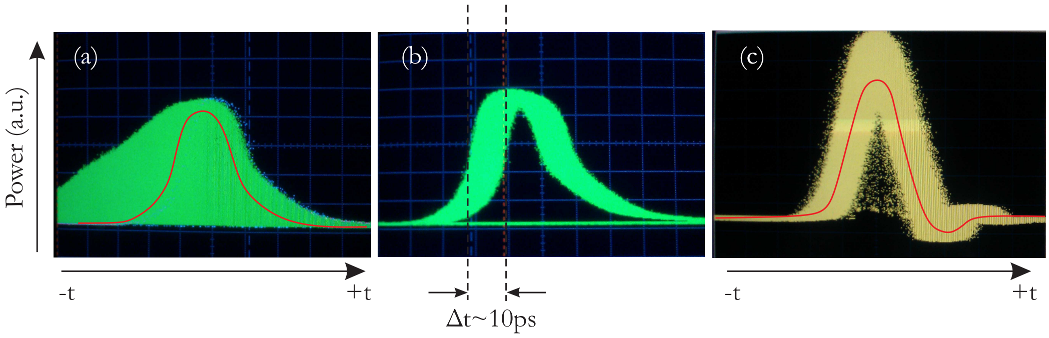

Figure 4.13: (a) Probe pulse drift and decoupling with decreasing temperature. (b) Probe pulse drift after 10 mins in a regulated temperature environment. (c) Probe pulse after 30 mins in a thermally isolated container.

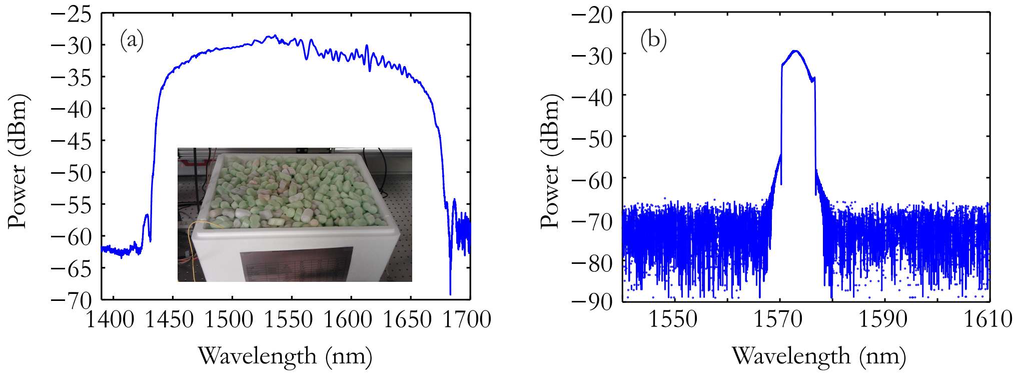

Figure 4.14: (a) Continuum produced from the HNLF. (b) Filtered probe pulse using a bandwidth-tunable variable filter.

incident probe pulse. Extinction ratio measurements for the modulated probe at pump powers of 250 W, 140 W, and 60 W are 3.5 dB, 2.3 dB, and 1 dB, respectively. Since the extinction ratio is strongly dependent on the TPA coefficients, it is expected that the highest pump power would yield an extinction ratio lower than that of the degenerate case as the non-degenerate TPA coefficient is lower. This extinction however, can be improved as $\beta_{\mathrm{TPA}p,s}$ is expected to increase with decreasing probe wavelength.

The estimated value of $\beta_{\mathrm{TPA}p,s}$ from this experiment is slightly lower than that obtained for the degenerate TPA parameter, this is predicted by the two-parabolic band model for indirect semiconductors [141] due to the lower photon energy of the probe. At this stage, it is difficult to comment on the magnitude of $\beta_{\mathrm{TPA}p,s}$ relative to c-Si or a-Si:H waveguides, as this experiment represents the first determination of the non-degenerate TPA coefficient in a-Si:H. Reports in literature have analysed these effects on liquids and biological samples, but non-degenerate TPA has yet to be characterised in bulk c-Si.

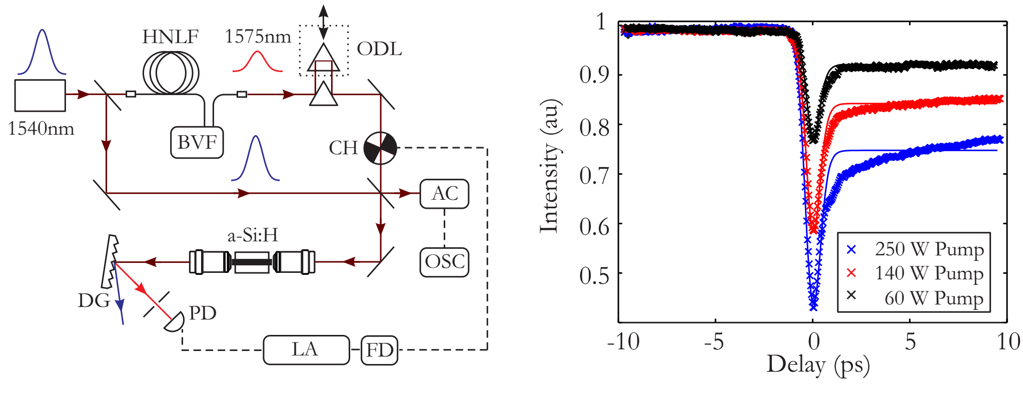

(a) (b)

Figure 4.15: (a) Non-degenerate pump-probe XAM experiment layout. (b) Probe modulation as a function of pump power.

4.7 Conclusion

This chapter introduced the concept of nonlinear absorption as an optical limiter in silicon. Many of the mechanisms such as TPA, FCA, and the outlined carrier dynamics play similar roles in a variety of semiconductors. In silicon, free carriers were shown to act as an additional nonlinear absorption mechanism that is a secondary consequence of TPA. The rate at which these carriers recover dictates the usable repetition rate of pulsed sources in these fibres. This recovery time depends strongly on the volume and surface defects of the core material as well as the value of the optical transmission losses. Nonlinear absorption could also be manipulated to amplitude modulate a CW signal by simply modulating either the free carrier concentration, or through two-photon absorption. This technique may find potential applications in optical noise suppression, where lasers subject to sudden power spikes can cause an impulse (or burst) of optical energy in a very finite time window. The ultrafast absorption response demonstrated of FCA and TPA can attenuate this impulse by several dB limiting the possible damage that it may cause to a system. This chapter has employed a number of experiments and characterisation methods to establish key nonlinear parameters of the a-Si:H fibre.

Chapter 5

Nonlinear Refraction in Silicon Fibres

5.1 Introduction

After several years of developing and optimising the silicon fibre platform, the first observation of nonlinear refraction was observed in the form of self-phase modulation (SPM) [142]. SPM is a direct consequence of the Kerr nonlinearity and from these observations it is possible to accurately estimate the n_2 coefficient for silicon fibres, thereby completing the unknown nonlinear variables of the generalized nonlinear Schrödinger equation (GNLSE) for a-Si:H. By building up a complete knowledge of the nonlinear material parameters, it is possible to obtain some insight into the characteristics and performance of nonlinear devices based on a-Si:H optical fibres. This chapter begins with a description of SPM, followed by the characterisation process to determine n_2, and then defines a figure of merit by which to measure the fibre's performance. Finally, the Kerr nonlinearity is exploited to demonstrate cross-phase modulation (XPM), an effect for which spectral modulation can be sufficiently strong to induce frequency shifting.

5.2 Self-Phase Modulation

The nonlinear time varying phase due to intense light propagation in a media was presented in Section 2.3.1.1 in the form:

$$\phi_{NL}(t) = n_2 I(t) k_0 z. \tag{5.1}$$

When an intense CW signal propagates through a nonlinear medium, the intensity and phase change can be assumed constant as a function of time. However, under ultrashort pulse operation the intensity $I(t)$ rapidly varies in time which results in a rapidly varying

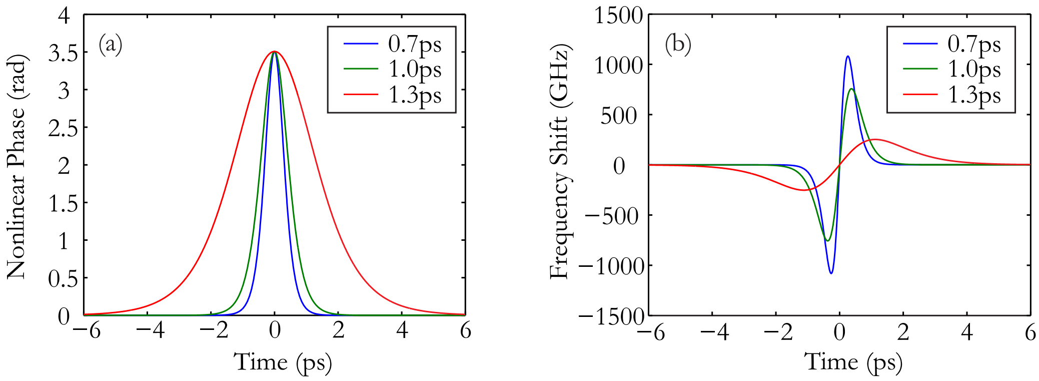

Figure 5.1: (a) Nonlinear phase shift for three sech^2 pulses. (b) Induced frequency change as a result of the nonlinear phase.

phase change [143]. Although the previous chapter has shown that the peak optical intensity and shape changes as a function of z due to nonlinear absorption, for simplicity we ignore these effects and account for the linear losses through the effective length L_{eff} parameter. The effective length is a scaled quantity of the propagation length accounting for the input power reduction and hence reduction in nonlinearity [144]. It is given by:

$$L_{\text{eff}} = \frac{1-\exp(-\alpha_l L)}{\alpha_l}. \tag{5.2}$$

Substituting this length into Equation 5.1 and re-writing,

$$\phi_{NL}(t) = \gamma L_{\text{eff}} |A(t)|^2, \tag{5.3}$$

the resulting nonlinear phase shift leads to a nonlinear frequency shift through the relation,

$$\begin{aligned} \Omega_{NL} &= -\frac{\partial \phi_{NL}(t)}{\partial t} \\ &= -\gamma L_{\text{eff}} \frac{\partial}{\partial t} |A(t)|^2 . \end{aligned} \tag{5.4}$$

Since the nonlinear effects in this thesis are predominantly investigated using a sech^2 pulse, the accumulated nonlinear phase shift and frequency shift of this pulse after propagating 2 cm in a silicon fibre is shown in Figure 5.1(a) and (b) respectively. Each figure illustrates different pulse widths but the peak powers are kept constant at 100 W. In this analysis, a pre-established n_2 of $\sim 18 \times 10^{-18}\,\text{m}^2/\text{W}$ is chosen and the sign of n_2 is always set to be positive as this is true for silicon when the optical frequencies have photon energies that are less than the band gap energy [53, 145]. Short pulse propagation can acquire a time-dependent nonlinear frequency change (or *chirp*) large enough to introduce many frequency components in the optical spectra, causing spectral broadening. Figure 5.1(b) is quite often referred to as the SPM-induced chirp. It exhibits identical frequency shifts at two distinct values of time, occurring with different phases due to the points of inflection in the excitation pulse. These two waves of identical frequency but differing phase can interfere constructively or destructively. Consequently, the broadened spectrum of the optical pulse will experience regions of high and low intensity with a fringe-like appearance. In the silicon fibres characterised in this chapter, the 6 μm core diameters result in highly multimoded fibres such that the nonlinear phase shift is a superposition of multiple propagating modes. It is therefore difficult to predict how the fringes may appear due to multimode interference [146], coupling [21, 147], and the distribution of induced phase shifts [148].

SPM, nonetheless, has enabled the realisation of a wide variety of advanced nonlinear components for performing ultrafast all-optical signal processing functions. Such applications include, wavelength conversion [149], signal regeneration [150, 151], switching [152], and format conversion [153]. To establish the suitability of the a-Si:H fibres for these applications, an evaluation of the nonlinear coefficient n_2 is required.

5.2.1 Characterising n_2

5.2.1.1 Technique

A number of measurement techniques have been developed to determine the n_2 of a fibre. The techniques rely on different nonlinear processes such as four-wave mixing (FWM) [154], modulation instability (MI) [155], XPM [156], and SPM [108]. Measurement of the Kerr nonlinearity through SPM has been the most widely used method for characterising novel waveguides (fibre and planar platforms), due to its simplicity. It is thus the focus of this section.

Observation of the spectral modulation due to SPM through an optical spectrum analyser (OSA) produces a curve which can be numerically fitted to either, a solution of the pulse's power spectral density:

$$\left|\tilde{A}(\omega)\right|^2 = \left|\int_{-\infty}^{\infty} A(t)\exp\left[i\phi_{NL}(t)\right]\exp(i\omega t)dt\right|^2, \tag{5.5}$$

or using the full simulated GNLSE. The former approach is quick and efficient when dispersion, linear absorption, multimodedness, and nonlinear absorption, can be ignored. For silicon fibres, all quantities need to be considered at near-infrared (NIR) wavelengths. Thus, a simulation of the complete GNLSE is required to obtain a fit to experimentally recorded measurements where n_2 is a free parameter. The description of the GNLSE provided here models only single-mode propagation. Spectral features due to multimode propagation are easily described and seen in a linear pulse propagation regime (i.e., low optical intensity). Figure 5.2(a) plots the effective refractive index for the first four circularly symmetric LP$_{mn}$ modes in a 6 μm core diameter silicon fibre. These particular modes are chosen as free-space coupling into silicon fibres are launched close

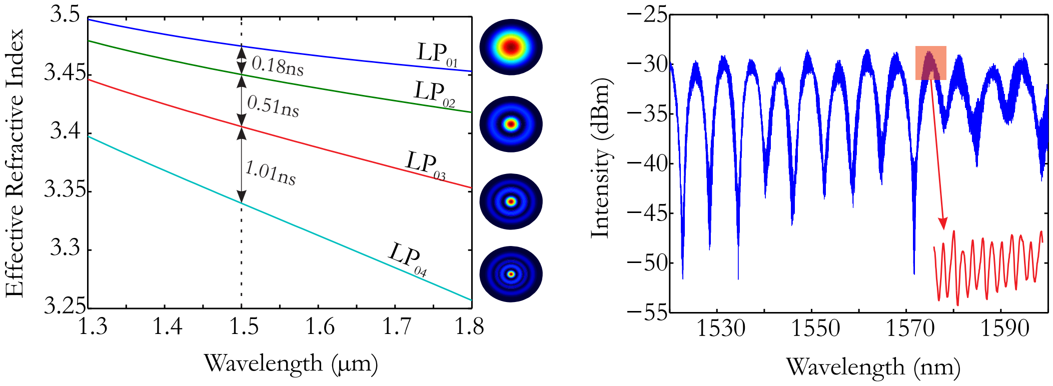

(a) (b)

Figure 5.2: (a) Effective index of circularly symmetric modes and respective group delay. (b) Multimode (blue) and Fabry-Perot (red) interference in a a-Si:H fibre.

to the optical axis of propagation, ensuring the coupling coefficients for the remaining modes are negligibly small [63]. Since the effective indices are different for each mode, it can be shown that their group velocities are also different through:

$$v_{g,mn} = \frac{c}{n_{\mathrm{eff},mn} + \omega \frac{dn_{\mathrm{eff},mn}}{d\omega}}. \tag{5.6}$$

When these modes propagate in a $L = 2\,\mathrm{cm}$ long silicon fibre the time of arrival of each mode is simply $t_{mn} = L/v_{g,mn}$. Figure 5.2(a) indicates this arrival time (at a wavelength of 1.5 μm) for each mode with respect the adjacent lower order mode. That is, the LP_{02} mode arrives 0.18 ns after the LP_{01}, the LP_{03} mode arrives 0.51 ns after the LP_{02} and so forth. The differences between group velocities of the co-propagating modes is so small that the difference in travel time of the modes in the silicon fibre is smaller than the coherence time of laser light. As a result, this creates an interference between all the present modes. An example of multimode interference (MMI) from a $\sim 1\,\mathrm{cm}$ long a-Si:H fibre is shown in Figure 5.2(b). The large MMI fringes separated by $\sim 7\,\mathrm{nm}$ are also composed of an even higher fringe periodicity that is due to the multiple reflections of each mode off the polished, high index fibre facets (a Fabry-Perot effect). The region highlighted in red is magnified to show the irregular interference pattern produced due to the multimode etalon. The MMI and etalon fringes superimpose themselves on high intensity pulse spectra. For clear spectral measurements of SPM (for example), the etalon based interference can be 'filtered' out by setting the spectral resolution of the instrument to a value at least two times larger than the fringe period, however the larger MMI spectra is not one that can be diminished without severely affecting the accuracy of the measurement. In many of the SPM measurements to be presented in this chapter, MMI contaminates parts of the spectrum. However, it has been shown that the effects of multiple modes in these specific fibres do not impair the estimation of n_2 using the single-mode GNLSE, but rather act to induce spectral modulations across the self-phase

Fibre	Core Diameter (μm)	α_{dB} (dB/cm)	Carrier Lifetime (ns)	β_{TPA} (m/W)	σ_{FCA} (m^2)
A	6	4.00	86	8.0×10^{-12}	1×10^{-20}
B	6	1.72	120	8.0×10^{-12}	1×10^{-20}
C	6	0.80	200	5.0×10^{-12}	1×10^{-20}
D	2	2.90	4	8.3×10^{-12}	1×10^{-20}

Table 5.1: a-Si:H fibres characterised for Kerr nonlinearity.

modulated envelope [157].

5.2.1.2 Measurements

Four different a-Si:H fibres are characterised. Fibres A-D from Section 4.5 are listed in Table 5.1 with the pre-established linear and nonlinear loss parameters. The experimental setup is of the same form illustrated in Figure 3.9(a) where the photodetector (PD) is replaced with an OSA. The OSA is set to a resolution of 0.1 nm and a sensitivity of −70 dBm. Each fibre's output spectrum is recorded as a function of input power and then normalised. The split-step GNLSE model of Equation 2.47 is simulated using the input pulse properties as given in Section 4.5 and shown in Figure 4.6. Since the extent of spectral broadening is primarily influenced by n_2, the simulated spectra are normalised and a difference integral of the simulated and measured spectral tails is calculated as a measure for the goodness of fit. It should be noted that the phase shifts or central spectral features due to SPM may be masked by the multimode behaviour of the fibre. It is for this reason that only the tails are fitted and the measure of variance is only used as a relative quantity between fittings in order to minimize the error in n_2. The nonlinear spectra produced from Fibres A, B, and C are shown in Figure 5.3. The raw normalised spectra are plotted in green and their respective fits are in blue. The quoted powers in each plot correspond to the experimentally recorded peak powers. The original simulation powers used were the same as that recorded experimentally though an additional fine tuning of each power was required to obtain a better fit, due to the slightly uncertainty in the coupling efficiency. A summary of the established Kerr nonlinearities is shown in Table 5.2.

Fibre A has the highest linear loss resulting in the shortest effective length. Since the nonlinear phase is directly proportional to L_{eff}, the broadened spectrum and chirp is consequently smaller than for Fibres B and C. One clear indication of the smaller nonlinearity can be seen in the central region of the simulated spectra of Fibre A, where the maximum phase shift $\phi_{\max}$ is approximated through the number of peaks M by [15]:

$$\phi_{\max} \approx \left(M - \frac{1}{2}\right)\pi \tag{5.7}$$

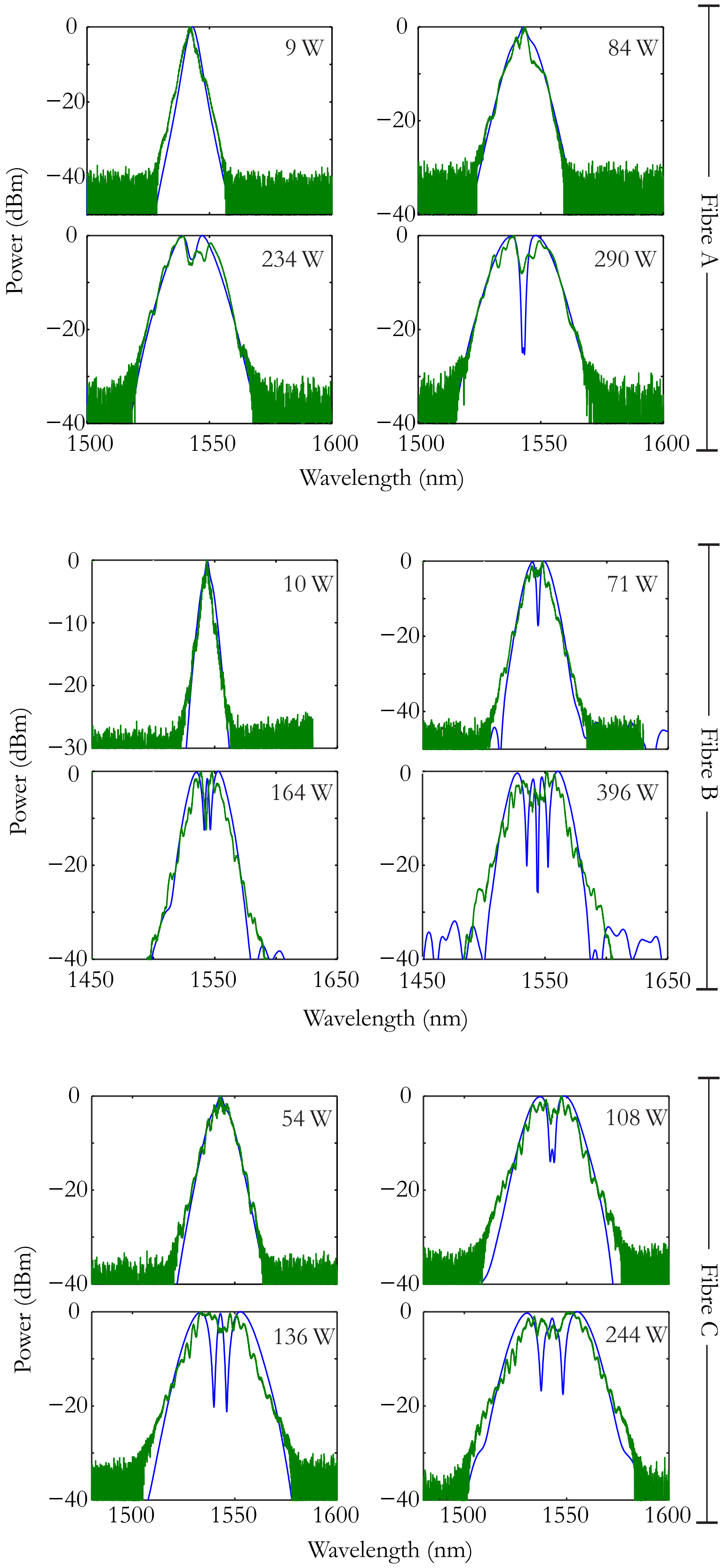

Figure 5.3: Power dependent SPM spectra of fibres A, B, and C (green) with numerical fits (blue).

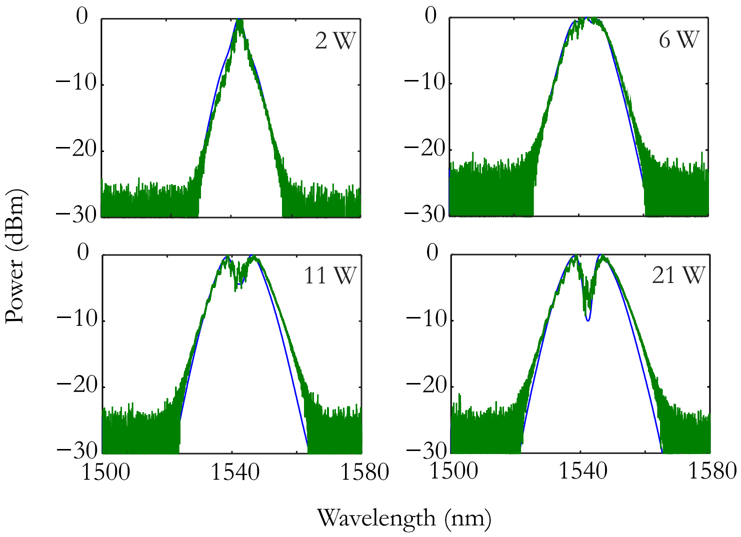

Figure 5.4: Power dependent SPM spectra of fibre D (green) with numerical fit (blue).

revealing $\phi_{\max} \approx 1.5\pi$. In comparison, Fibres B and C experience greater spectral broadening, and the simulated results correspondingly indicate a larger phase shift due to their lower transmission losses. It is also interesting to observe that due to their lower losses, there is an enhanced visibility of rippling across the spectral envelope in Fibres B and C. These features, could be due to the modes interfering for a longer propagation distance since the interaction length is enhanced with each internal reflection off the fibre facet [148]. The SPM spectra from the smaller core fibre (Fibre D) is shown in Figure 5.4. The 11 W spectrum of the small core fibre has a similar spectral broadening to that obtained with 136 W in the lowest loss 6 μm core fibre (Fibre C), at their 20 dBm widths. The oscillations of the experimentally recorded spectra appear more prominent on the blue-shifted end of the spectrum. These oscillations have been shown to correspond very closely to the MMI from the first few most likely excited circularly symmetric modes of the silicon fibre through numerical analysis [157]. In this analysis, it was shown that approximately 99% of the optical power was contained in the LP_{01} mode. This estimation was reinforced by performing a weighted least-squares misfit error on the numerical and experimental spectra.

Fibre	n_2 (m^2/W)
Fibre A	13.5×10^{-18}
Fibre B	18.5×10^{-18}
Fibre C	14.5×10^{-18}
Fibre D	18.0×10^{-18}

Table 5.2: Kerr coefficients for several a-Si:H fibres characterised at $\lambda = 1.54\,\mu$m using numerical fitting of the experimental SPM spectra.

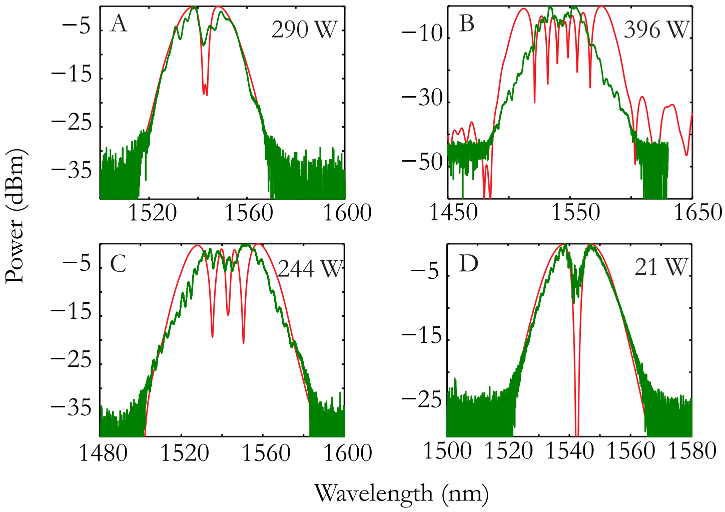

Figure 5.5: Highest power SPM spectra showing numerical fits (red) in the absence of FCA only.

A noticeable property of the SPM spectra associated with Fibres A-D is that they are quite symmetric. The TPA and FCA coefficients are wavelength dependent parameters and can begin to influence the spectral shape for considerably large linewidths ($> 100\,\mathrm{nm}$ at $20\,\mathrm{dB}$). Ignoring the minor features across the envelopes, SPM has quite commonly been observed in planar silicon waveguides with an asymmetric spectral distribution about the injected laser frequency [144]. Reports have explained its presence due to TPA and FCA shaping the red and/or blue-shifted parts of the spectrum [65, 130, 158, 159]. To observe how TPA and/or FCA affect the spectra, Figure 5.5 plots the highest coupled input power spectra for Fibres A-D, and reproduces the corresponding simulation parameters omitting the contributions of FCA. In the presence of nonlinear absorption due to only TPA, additional nonlinear phase shifts are more pronounced with slightly more spectral broadening. Fibre B exhibits the most appreciable change in the absence of FCA, whereas the lowest loss fibre (Fibre C) only sees a minor change in its nonlinear phase. This could be in part due to the carrier lifetime of Fibre B which is almost half of that of Fibre C, leading to less absorption due to excessive carrier build up, or the lower TPA coefficient of Fibre C thereby generating less carriers. It should also be noted that the simulations used do not include wavelength dependent β_{TPA} nor σ_{FCA} coefficients, since their dependence is yet to be established.

The nonlinear spectra from each of these fibres have allowed for the first estimation of the Kerr nonlinear index coefficient in a-Si:H fibres. With all critical nonlinear parameters established, it is also useful to gauge a quantitative merit that silicon fibres may have with respect to nonlinear applications. The nonlinear figure of merit was developed for this reason, whereby different nonlinear platforms such as chalcogenide fibres, semiconductor waveguides (planar), glass waveguides (planar), soft glass fibres, and silicon fibres can be compared.

5.2.2 Figure of Merit

In the late 1980s efforts were being made to develop materials with an increased nonlinearity [160–162], though it was realised that the effects of nonlinear absorption (particularly two-photon effects) varied between materials which affected the overall nonlinear performance. A nonlinear figure of merit (FOM_{NL}) was established [163] not long after, which was defined as a normalised ratio of n_2 to β_{TPA}. This ratio indicates the suitability of a material for nonlinear all-optical switching applications at a desired wavelength. The actual value needed for FOM_{NL} depends on the nature of the phase change required for the optical switch [164]. In much of the literature on nonlinear silicon photonics, the definition of the FOM is varied between two forms, each are simply the inverse of the other. The preferred definition is not important, though the definition adopted in this work is [53, 131, 165, 166]:

$$\mathrm{FOM}_{NL} = \frac{n_2}{\lambda_0 \beta_{\mathrm{TPA}}}. \tag{5.8}$$

The FOM_{NL} provides a means to establish the maximum achievable nonlinear phase shift in a particular material. From Equation 5.1, n_2 can be substituted with the FOM_{NL} to give,

$$\phi_{NL}(t) = 2\pi \mathrm{FOM}_{NL} I(t) \beta_{\mathrm{TPA}} z. \tag{5.9}$$

Assuming there is a sufficient intensity or interaction length to induce a nonlinear phase shift, then the limiting case of Equation 2.36 can be applied to produce the maximum induced nonlinear phase of:

$$\phi_{NL}(t) = 2\pi \mathrm{FOM}_{NL}. \tag{5.10}$$

Values of $\mathrm{FOM}_{NL} > 2$ are necessary for applications requiring a minimum nonlinear induced phase shift of 4π or higher. Such applications involve processes through XPM to create nonlinear directional couplers. Values where $0.5 < \mathrm{FOM}_{NL} < 2$ are suitable for applications only requiring a π phase shift, such as Mach-Zehnder interferometers.

FOM_{NL} is calculated for the a-Si:H fibres characterised previously. They are presented in Table 5.3 with a comparison of a variety of materials in bulk, rib waveguide, photonic crystal (PhC), wire, and fibre platforms. The variations of FOM_{NL} are fairly wide between materials, ranging from 0.3 to 11. The chalcogenide family of Arsenic Selenides typically possess a higher FOM_{NL} due to their lower TPA, whereas silicon heavily depends on its state of phase. For example, a-Si:H has been shown to possess a FOM_{NL} that is equal to or higher than c-Si. The a-Si:H fibres characterised in this work are all slightly higher than those of c-Si as well as several of the a-Si:H waveguides, which is possibly attributed to the novel high pressure fabrication method employed. The revealed values for the a-Si:H fibres indicate that nonlinear processes relying on wave mixing (e.g. XPM) have poor efficiencies since $\mathrm{FOM}_{NL} < 2$. However, it is evident that a minimum nonlinear phase shift of π is easily achievable, thereby showing potential in interferometric based switching applications. Many all-optical device functionalities

Platform	Material	Wavelength (μm)	n_2 $\times 10^{-18}$ (m^2/W)	β_{TPA} $\times 10^{-12}$ (m/W)	FOM$_{NL}$	Ref.
Bulk	c-Si <110>	1.54	4.5	7.9	0.40	[167]
Bulk	c-Si <111>	1.54	4.3	8.8	0.30	[131, 168]
Bulk	$As_{40}S_{60}$	1.55	5.6	0.3	12.00	[169]
Fibre	As_2Se_3	1.55	9.0	2.5	2.30	[151]
Rib	As_2Se_3	1.50	12.0	1.0	8.00	[169]
PhC	Ag-As_2Se_3	1.55	N/A	N/A	11.00	[170]
Strip	a-Si:H	1.55	0.5	0.8	0.40	[139]
Rib	a-Si:H	1.55	42.0	41.0	0.66	[126]
Rib	a-Si:H	1.55	N/A	N/A	2.20	[127]
Wire	a-Si:H	1.55	21.0	2.5	5.40	[128]
Fibre A	a-Si:H	1.54	13.5	8.0	1.10	-
Fibre B	a-Si:H	1.54	18.5	8.0	1.50	-
Fibre C	a-Si:H	1.54	14.5	5.0	1.90	-
Fibre D	a-Si:H	1.54	18.0	8.3	1.40	-

Table 5.3: Comparison of FOM$_{NL}$ for different materials.

predominantly requires the ability to switch light from an on to off state. A π shift in phase can easily achieve this through constructive (on) or destructive (off) interference.

5.3 Cross-Phase Modulation

For SPM, it was shown that a nonlinear phase shift arises due to the intensity dependent refractive index. Similarly, this analysis can be extended to a scenario in which multiple co-propagating waves (j) induce linear or nonlinear phase shifts. XPM refers the nonlinear coupling of these phase shifts and is of particular importance since it allows for the control of one pulse via a nonlinear phase shift using a second pulse at a different wavelength. The nonlinear induced phase shift of a particular wave is given by:

$$\phi_{NL,j} = n_2 k_{0j} z [I_j(t) + 2I_{3-j}(t)], \tag{5.11}$$

where $j = 1$ or 2. Following a similar analysis and simplification procedure to that presented at the start of Section 5.2, the XPM-induced chirp on fields 1 and 2 can be shown to be:

$$\Omega_{NL,1} = -\gamma_1 L_{\text{eff}} \left[\frac{\partial}{\partial t}|A_1(t)|^2 + 2\frac{\partial}{\partial t}|A_2(t)|^2 \right], \tag{5.12}$$

$$\Omega_{NL,2} = -\gamma_2 L_{\text{eff}} \left[\frac{\partial}{\partial t}|A_2(t)|^2 + 2\frac{\partial}{\partial t}|A_1(t)|^2 \right]. \tag{5.13}$$

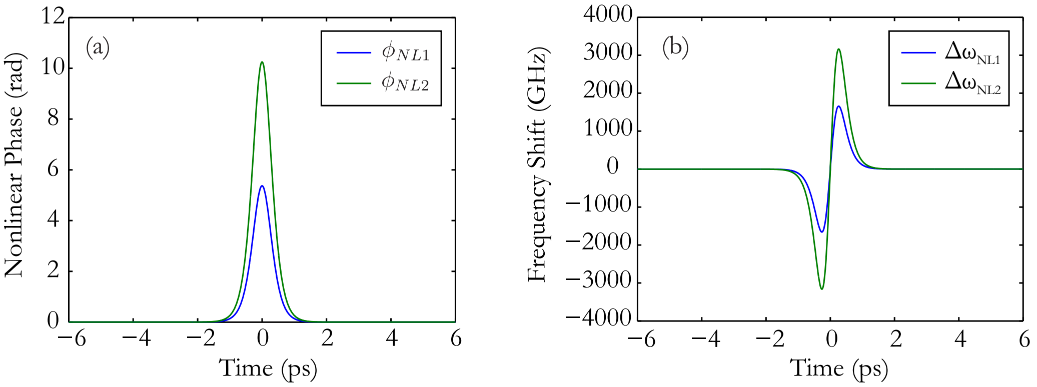

Figure 5.6: (a) XPM induced nonlinear phase shift on pump $\phi_{NL,1}$ at 1540 nm and probe $\phi_{NL,2}$ at 1590 nm. (b) XPM-induced frequency change as a result of the induced nonlinear phases.

To illustrate how the phase change and frequency shifts vary in magnitude in the case that field 1 acts as a strong pump pulse $\sim$ 100 W, and field 2 acts as a weak probe pulse $\sim$ 1 W, Figure 5.6(a) and (b) show the two quantities plotted against time. The nonlinear induced phase plots indicate that the weak probe pulse experiences a stronger nonlinear phase shift $\phi_{NL,2}$ and hence frequency change due to XPM. This effect has been widely investigated in planar c-Si waveguides, with its use being demonstrated for ultrafast all-optical switching [171], gating [172], and 3R regeneration [173], however only limited studies have been made in a-Si:H [139].

From Section 5.2.2 it was shown that in the presence of TPA, the a-Si:H fibres that have been investigated to date exhibit a FOM_{NL} that is incapable of directly inducing a phase shift larger than 4π. Consequently, the frequency change due to XPM becomes difficult to measure with a conventional pulsed pump, CW probe, and optical spectrum analyser setup due to the limited resolution. In order to investigate this phase and frequency change, a full time-resolved characterisation of the induced XPM in a a-Si:H fibre is required. To achieve this, the pump-probe technique employed in Section 4.6.2 is used as this exhibits a higher sensitivity. In addition, numerical simulations based on a set of coupled-mode nonlinear propagation equations are used to analyse the influence of the pump pulse and waveguide parameters on the spectral modulation. A brief description of these coupled equations is first presented.

5.3.1 Coupled-Mode Extended NLSE

The coupled-mode analysis used here is a full nonlinear propagation approach that includes the effects of degenerate and non-degenerate TPA on the pump, probe, and carrier density. The free carrier contributions are likewise also considered for the pump $\sigma_{\text{FCA}p}$ and probe $\sigma_{\text{FCA}s}$, as the Drude-Lorenz model suggests that FCA is wavelength dependent, though the differences are small. Hence the two FCA coefficients in this instance are the same. Unlike the numerical analysis discussed in Section 4.4, the applied fields can be of equal strength and the full temporal and spectral domain is simulated using the split-step method described in Section 2.4. A generalized scalar evolution of a single-moded pump field, probe field, and the carrier density, can be represented by [174–176]:

$$\frac{\partial A_p}{\partial z} + \beta_{1p}\frac{\partial A_p}{\partial t} + i\frac{\beta_{2p}}{2}\frac{\partial^2 A_p}{\partial t^2} = i\left(\gamma_{p,p}|A_p|^2 + 2\gamma_{p,s}|A_s|^2\right)A_p - \frac{1}{2}(\alpha_l + \sigma_{fp})A_p, \tag{5.14}$$

$$\frac{\partial A_s}{\partial z} + \beta_{1s}\frac{\partial A_s}{\partial t} + i\frac{\beta_{2s}}{2}\frac{\partial^2 A_s}{\partial t^2} = i\left(\gamma_{s,s}|A_s|^2 + 2\gamma_{s,p}|A_p|^2\right)A_s - \frac{1}{2}(\alpha_l + \sigma_{fs})A_s, \tag{5.15}$$

$$\begin{aligned}\frac{\partial N}{\partial t} = \frac{1}{2hA_{\text{eff}}^2}\Bigg[&\frac{\beta_{\text{TPA}p,p}}{\nu_p}|A_p|^4 + \frac{\beta_{\text{TPA}s,s}}{\nu_s}|A_s|^4 + \frac{2\beta_{\text{TPA}p,s}}{\nu_p}|A_pA_s|^2 + \\ &\frac{2\beta_{\text{TPA}s,p}}{\nu_s}|A_sA_p|^2\Bigg] - \frac{N}{\tau},\end{aligned} \tag{5.16}$$

where

$$\gamma_{j,l} = \frac{k_{0j}n_2}{A_{\text{eff}}} + i\frac{\beta_{\text{TPA}j,l}}{2A_{\text{eff}}}, \tag{5.17}$$

$$\sigma_{fj} = \sigma_j(1 + i\mu_j)N. \tag{5.18}$$

In these equations, we assume that the two optical fields experience a similar linear loss and have similar effective mode areas, which is valid for closely spaced wavelengths. Analytical solutions to the XPM-induced phase change and hence frequency change have been obtained for a known Gaussian input pulse, however these do not hold in the presence of TPA and FCA. As shown in the previous chapter, the nonlinear losses are non-negligible for a-Si:H fibres hence simplified solutions will not be discussed. For the simulation of the coupled-mode equations a table of all the parameters used will be presented in each of the following sections (5.3.2 and 5.3.3).

The aforementioned applications of XPM (switching, gating, and regeneration) all require the ability to induce an optically measurable shift in the carrier frequency of a probe wave. The magnitude of the induced frequency shift is dependent on the interplay between all of parameters of the coupled-mode equations. However, from Equations 5.12 and 5.13, the most influential feature can be attributed to the rate of change of the pulse envelope. For this reason, two regimes of propagation in the a-Si:H fibre are investigated. A ‘long’ pulse and ‘short’ pulse regime, where the pulse width is varied between 3 ps and 700 fs (FWHM), respectively.

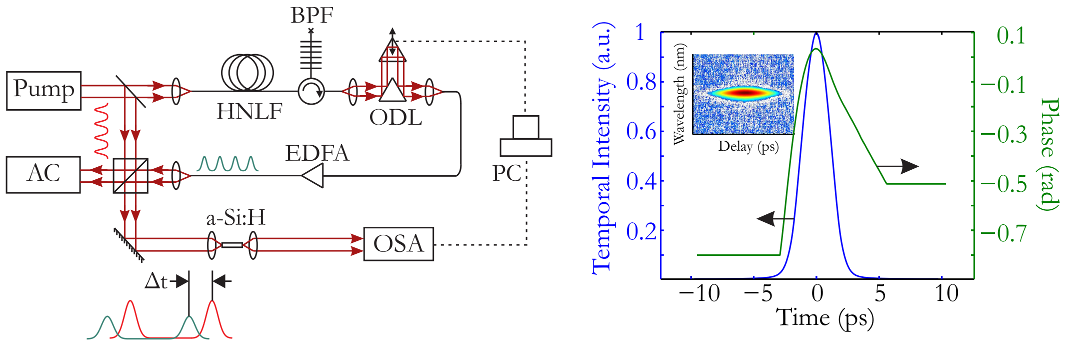

(a) (b)

Figure 5.7: (a) Experiment for the observation of XPM in the long pulse regime. Solid lines are optical paths, broken lines are electronic cables. $\Delta t = \tau_d$ is the delay between the pulse centres. (b) Recovered FROG trace of the probe pulse's intensity and phase profile. Inset shows the recorded spectrogram.

5.3.2 Long Pulse Regime

The pump-probe experiment employed in the long pulse regime for observing XPM slightly differs to that in Chapter 4. The experiment shown in Figure 5.7(a) synchronises the OSA to the optical delay line (ODL) through a PC, rather than utilising lock-in detection. The software was written in Matlab to utilise USB protocols to address the OSA and voltage controller of the ODL. This produces minimal communication delays allowing the experiment to run at a sufficient speed to avoid errors due to mechanical instability in the optics. The spectra from the HNLF is filtered with a Bragg grating to produce 3 ps pulses at 1590 nm. Due to the grating's spectral reflection profile the picosecond pulses were Gaussian as measured by the FROG, where the result is shown in Figure 5.7(b). The recovered phase profile (green) exhibits a slight parabolic profile, indicating a minor chirp, though this was shown to have a negligible effect on the results.

The 300 W peak pump and 1 W peak probe power pulses co-propagate in an 8 mm long a-Si:H fibre, whose properties are those of Fibre B. The power of the pump was chosen such that after it experiences SPM in the a-Si:H fibre, there is still no spectral overlap (until -50 dBm) with the probe wavelength. The probe is also not of sufficient power to induce SPM. The length of silicon fibre chosen here can be understood as follows; the pump pulse centred at 1540 nm exhibits an estimated inverse group velocity of $\beta_1 \sim 12016$ ps/m, and the probe exhibits $\beta_1 \sim 11979$ ps/m (assuming the dispersion of c-Si). By calculating the walk-off length of the individual pulse widths, this reveals $L_w \sim 1.9$ cm and $L_w \sim 8.8$ cm for the 700 fs and 3 ps pulses respectively. Hence a fibre length less than these walk-off lengths (< 1 cm) was chosen so that the temporal delay between each pulse is set by the ODL. After polishing each facet the resulting length was 8 mm. Aside from these walk-off lengths, it is also important to ensure that the

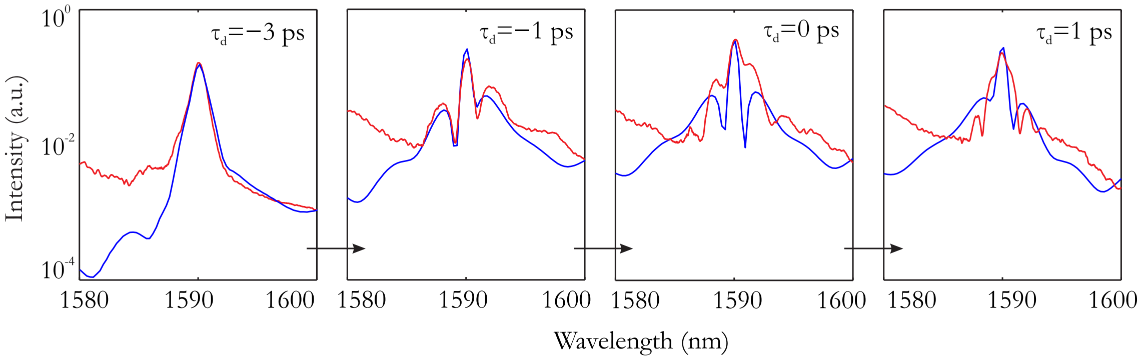

Figure 5.8: Experimental temporal evolution of XPM on the 3 ps probe pulse (red) together with the simulation results (blue). A peak pump power of 300 W was used, and the probe power was limited to 1 W. Fibre parameters are in Table 5.4.

electronic delay line is capable of transversing a temporal resolution τ_d larger than the shortest pulse length. For 3 ps, this corresponds to a motor pitch length that is less than 900 μm.

5.3.2.1 Spectral Modulation

This experiment operates by measuring an output spectrogram which then is analysed to estimate the magnitude of XPM for all-optical processing. Figure 5.8 presents four subplots of the XPM process using the picosecond probe at various time delays. In this experiment, a negative time delay corresponds to the probe pulses trailing behind the pump, and a positive time delay when the probe leads the pump. Spectral modulation is clearly observed when the pump and probe pulses are within close temporal proximity, generating sidebands symmetrically about the probe. Numerical simulations (plotted in blue) also suggest this behaviour, where each lobe varies in gain depending on the temporal delay. The simulation parameters used are given in Table 5.4.

The complete spectrogram of the results is compiled and shown in Figure 5.9(a). At close to $\tau_d = 0$, significant depletion in the optical intensity is present. This feature is largely a consequence of XAM as described in Section 4.6. It should be noted that the process does not appear symmetric about $\tau_d = 0$. This could be in part due to a slight chirp induced on either pump or probe or free carrier effects, as it should reflect a symmetric nonlinear phase shift. More importantly, the objective is to determine whether frequency shifting is measurable at this pulse width. Tracing the peak wavelength position through each temporal delay in Figure 5.9(a) reveals that the carrier wavelength is fairly consistent as shown in Figure 5.9(b). The minor fluctuations observed in this plot could not be resolved by the spectrum analyser, hence the observed shifts are merely systematic errors. Numerical simulations indicate likewise.

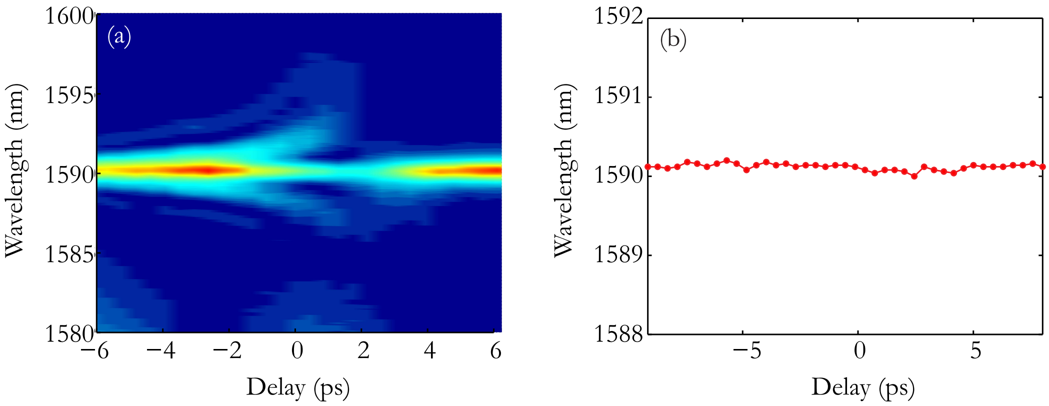

Figure 5.9: (a) Experimentally measured spectrogram of the XPM process on the probe pulse recorded over a 12 ps time window. (b) Trace of peak wavelength through the spectrogram indicating no shift in the central wavelength.

The good agreement between the simulations and experiments, produce only a modest difference in the sidebands in Figure 5.8 and some discrepancy is expected given the precision, number of variables, and sensitivity of the experiment. The analysis presented

Parameter	Units	Value	Citation
λ_p	nm	1540	
λ_s	nm	1590	
$T_{\mathrm{FWHM}p}$	fs	700	
$T_{\mathrm{FWHM}s}$	fs	3000	
P_p	W	290	
P_s	W	1	
$\Delta\beta_1$	ps/m	37.1460	[177]
β_{2p}	ps^2/m	0.9915	[177]
β_{2s}	ps^2/m	0.9399	[177]
n_2	m^2/W	14.5×10^{-18}	
A_{eff}	m^2	14×10^{-12}	
$\beta_{\mathrm{TPA}p,p}$	m/W	8×10^{-12}	
$\beta_{\mathrm{TPA}s,s}$	m/W	0.5×10^{-12}	
$\beta_{\mathrm{TPA}p,s}$	m/W	0.5×10^{-12}	
$\beta_{\mathrm{TPA}s,p}$	m/W	0.5×10^{-12}	
α_{dB}	dB/cm	3	
μ_p	–	1.102	[65]
μ_s	–	1.07	[65]
σ_p	m^2	1×10^{-20}	
σ_s	m^2	1×10^{-20}	
τ	ns	86	

Table 5.4: Simulation parameters used in the coupled-mode equations to obtain the closest spectral modulation of XPM to the picosecond probe pulses. The time frame is normalised to the pump (p) so that the dispersion term $\Delta\beta_1 = \beta_{1s} - \beta_{1p}$.

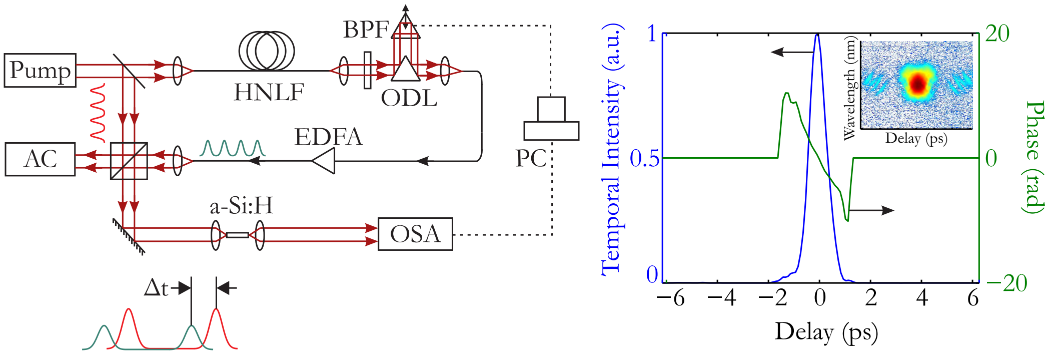

(a) (b)

Figure 5.10: (a) Experiment for the observation of XPM using femtosecond probe pulses. The BPF has a 12 nm bandwidth ensuring sub-picosecond pulses from the HNLF. Δt is again represented as τ_d. (b) Recovered FROG trace from 1587 nm filtered HNLF showing the intensity (blue) and phase (green) profile of the probe. Spectrogram from FROG shown as an inset.

here reveals that these picosecond probe durations generate modest spectral conversion, with little reduction of the central carrier, so that there is no observable wavelength shifting of the signal beam, a result also predicted by simulations. However, many of the previous investigations in the literature that demonstrate strong wavelength shifts, employ sub-picosecond pump and probe pulses. Since the pump pulses in this experiment are sub-picosecond, a filtering method of the probe pulse was then pursued to achieve a shorter probe.

5.3.3 Short Pulse Regime

In this work, the previously employed fibre grating configuration is replaced with a 1587 nm free space dielectric bandpass filter (BPF) as shown in Figure 5.10(a). Since the BPF has a considerably larger bandwidth (∼ 12 nm), it is able to support pulses as short as the 700 fs pump pulse. Though this pulse experiences slight temporal (and large spectral) broadening due to the HNLF. The filtered probe pulses were again analysed on the FROG. The intensity and phase profile is plotted in Figure 5.10(b) showing an 800 fs probe pulse. It is also clear that a linear phase is present across the pulse indicating a near zero chirp. This is expected as the HNLF has a very low dispersion. The pulses are then launched into the a-Si:H fibre and the XPM spectra are recorded in the same procedure as that described in the picosecond experiment.

Spectral modulation due to XPM was stronger than anticipated. For this reason, several subplots are presented in Figure 5.11 that show time delays in which the highest nonlinear activity was present. The dynamics of the XPM process show strong modulation as a function of the temporal overlap despite the fact that XAM causes power depletion due to nonlinear absorption. To some degree, this can be attributed to the

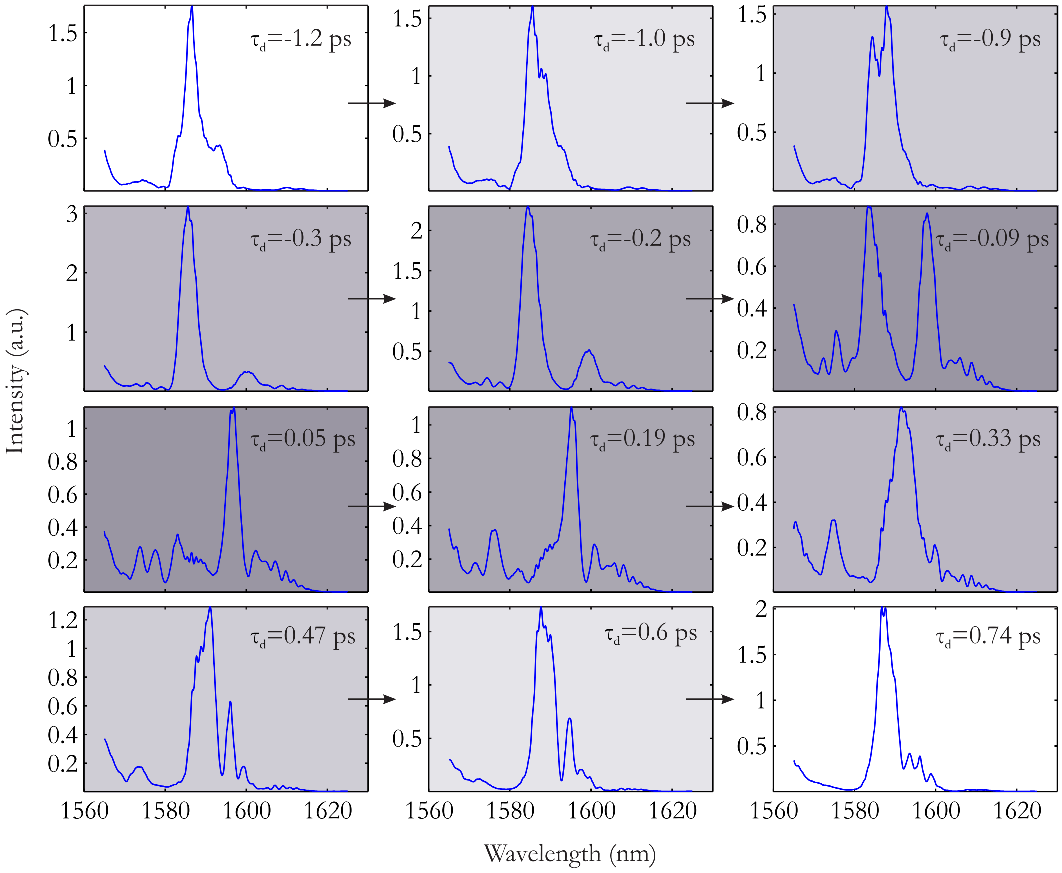

Figure 5.11: Temporal evolution from negative to positive time delays of the XPM process using an 800 fs probe pulse. Spectral modulation and wavelength shifting is significantly more pronounced.

FOM$_{NL}$ of the a-Si:H fibre where n_2 is high enough to avoid β_{TPA} being dominant. The subplots also indicate that each spectral variation evolves to an extent where the gain of the generated sidebands competes against one another. For example, in the plots of $\tau_d = -0.3$ ps and $\tau_d = -0.09$ ps, the minor red-shifted secondary peak at -0.3 ps immediately grows within the 0.21 ps delay to become the dominant carrier. Shorter pulses are expected to acquire a larger chirp within the a-Si:H fibre, hence the asymmetry of the XPM process about $\tau_d = 0$ is again understandable. It is quite clear from these plots that the position of the highest peak power in wavelength varies quite strongly with delay. Due to the complex spectral profile of the probe and the nonlinear modulations present, it was difficult to produce similar results through simulations. However, when a complete spectrogram of the process is viewed, it can be simulated to match the observed frequency shifting of XPM more clearly.

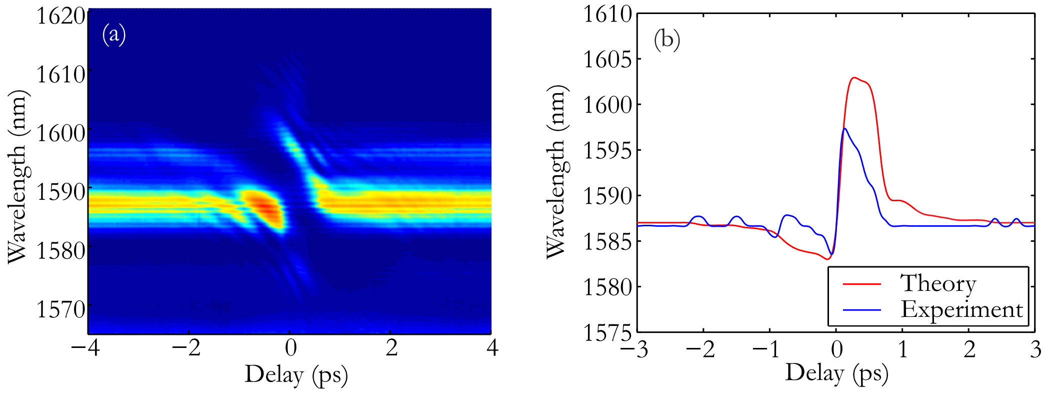

Figure 5.12: (a) Recorded spectrogram of the short pulse XPM process. (b) Measured (blue) and numerically fitted (red) peak wavelength shift of the sub-picosecond probe pulse.

5.3.3.1 Frequency Shifting

The spectrogram of the sub-picosecond XPM experiment is shown in Figure 5.12(a). Comparing this result with the earlier picosecond spectrogram, it can be seen that there has been a much stronger depletion of the central probe wavelength close the zero delay point. This depletion is clearly XPM dominated as opposed to XAM since new spectral components appear around 1597 nm. The extent of wavelength shifting is more clearly seen by tracing the peak of the wavelengths as a function of delay. Figure 5.12(b) reveals the experimentally recorded XPM-induced frequency shift (blue) which is comprised of an initial blue-shift of $\sim$ 4 nm, followed by a large red-shift of $\sim$ 10 nm. The largest shift recorded in nanoscale c-Si waveguides has been reported at 15 nm [171], making the a-Si:H fibre shift quite significant given the larger effective mode area of the 6 μm core fibre. The frequency shift plot confirms a distinctive feature of the XPM-induced shift, in that the timescale at which the process is able to shift between blue and red wavelengths is on the order of 100 fs, indicating truly ultrafast switching ability. In an attempt to verify the observed wavelength shift, simulations were performed to closely match that of Figure 5.12(b). The simulation parameters used are given in Table 5.5. The numerically calculated curve plotted in red suggests the process could have induced a larger red-shift over a range of delays.

The discrepancies between the experimental and numerical data curves, are similar to the differences observed by other groups. Specifically, they have attributed the differences in the wavelength shift and shape of the numerical results to uncertainties in the exact waveguide dispersion [171], and the asymmetric envelope in the probe's spectral profile at the input [174]. In this experiment, it is likely that both of these aspects play a role. Firstly, there is uncertainty of the fibre's dispersion as the material dispersion for c-Si is used for the numerical simulations as discussed in Section 5.3.2. Secondly, it can also be see in the first subplot of Figure 5.11 that the filtered probe spectrum contains a

Parameter	Units	Value	Citation
λ_p	nm	1540	
λ_s	nm	1587	
$T_{\mathrm{FWHM}p}$	fs	700	
$T_{\mathrm{FWHM}s}$	fs	800	
P_p	W	280	
P_s	W	1	
$\Delta\beta_1$	ps/m	37.1460	[177]
β_{2p}	ps^2/m	0.9915	[177]
β_{2s}	ps^2/m	0.9399	[177]
n_2	m^2/W	15×10^{-18}	
A_{eff}	m^2	14×10^{-12}	
$\beta_{\mathrm{TPA}p,p}$	m/W	8×10^{-12}	
$\beta_{\mathrm{TPA}s,s}$	m/W	0.5×10^{-12}	
$\beta_{\mathrm{TPA}p,s}$	m/W	0.5×10^{-12}	
$\beta_{\mathrm{TPA}s,p}$	m/W	0.5×10^{-12}	
α_{dB}	dB/cm	3	
μ_p	–	1.102	[65]
μ_s	–	1.07	[65]
σ_p	m^2	1×10^{-20}	
σ_s	m^2	1×10^{-20}	
τ	ns	86	

Table 5.5: Simulation parameters used in the coupled-mode equations to obtain the closest XPM-induced frequency shift relative to the experimentally measured shift.

small pedestal at 1595 nm, which is due to the BPF's profile. However, simulating the coupled-mode equations with a probe pulse containing a similar pedestal showed little noticeable difference in the XPM-induced shift. Thus, the differences arising due to the complex interplay of linear and nonlinear parameters in the modeling are more difficult to interpret, and greatly alter the comparison between theory and experiment. However, the time-dependent frequency shift can be interpreted from a different perspective to reveal subtle information behind the physics of the XPM process such as the induced refractive index changes.

The measured frequency shift plot of λ_s vs τ_d can easily be converted to a Ω_s vs τ_d plot. Since the nonlinear phase is a time varying quantity, a running integral is performed over the numerical fit of Figure 5.12(b) as shown in Figure 5.13(a). That is,

$$\phi_{NL} = -\int_{-\infty}^{\infty} \Omega_s \, d\tau_d. \tag{5.19}$$

The numerical method chosen uses a simple trapezoidal rule of integration to estimate the nonlinear phase. In Section 2.3.1.1 the description of a material's refractive index was shown in Equation 2.25. This form neglected the contribution of the free carrier

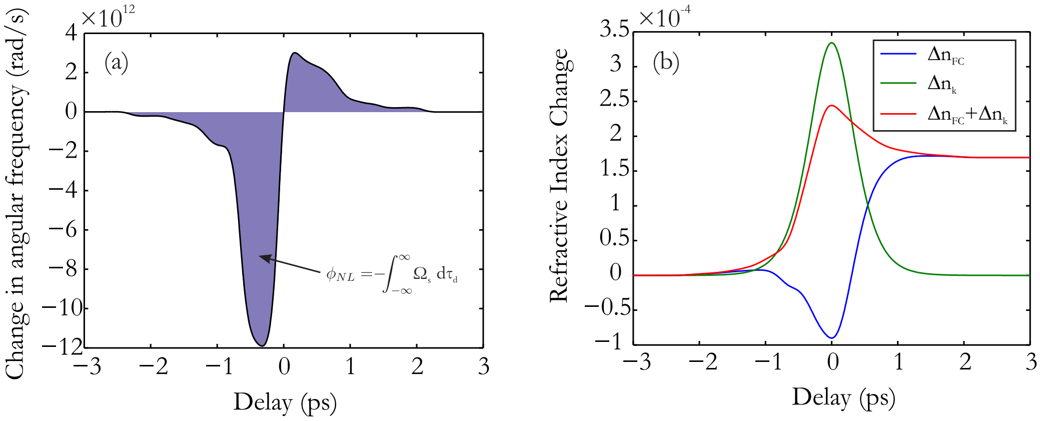

Figure 5.13: (a) Integral of the frequency change to obtain the nonlinear phase shift. (b) Contributions of the Kerr and free carrier induced refractive index changes.

induced index changes. It is more accurate to represent the total index as:

$$\tilde{n}(\omega, \tau_d) = n(\omega) + \Delta n_k(\tau_d) + \Delta n_{\mathrm{FC}}(\tau_d), \tag{5.20}$$

where $\Delta n_k(\tau_d) = n_2 I_1(\tau_d)$ is the nonlinear Kerr induced index change, and $\Delta n_{\mathrm{FC}}(\tau_d)$ the nonlinear index change due to free carriers. From this, the nonlinear phase shift on the probe can easily be shown to be:

$$\phi_{NL,2}(\tau_d) = k_{02} L_{\mathrm{eff}} [\Delta n_{k1}(\tau_d) + \Delta n_{\mathrm{FC}}(\tau_d)]. \tag{5.21}$$

Since $I_1(\tau_d)$ has been accurately characterised (from $I_1(t)$), and $\phi_{NL,2}(\tau_d)$ established by performing a numerical integral, the induced refractive index changes can be decoupled. Figure 5.13(b) shows the final quantities separated into their individual components. The Kerr nonlinearity appears to slightly dominate the index change, where the free carrier changes vary from negative to positive depending on the temporal delay. At $\tau_d = 0$ the nonlinear absorption and hence free carriers is highest. The refractive index change due to excessive free carriers has long been known to induce a negative change in the index [32]. One can attest to the relative accuracy of these curves by noting that the rapid 100 fs change in wavelength occurs at the point of inflection for the total refractive index curve. Since the inflection point represents the region of highest rate of change, and the wavelength depends on its derivative, it is thereby conclusive that the use of shorter pulses would reveal larger wavelength shifts.

5.3.3.2 Frequency Depletion

From a nonlinear applications point of view, the achievable wavelength shift is only one unit of measure. A critical parameter that determines the 'extent' of energy transfer is

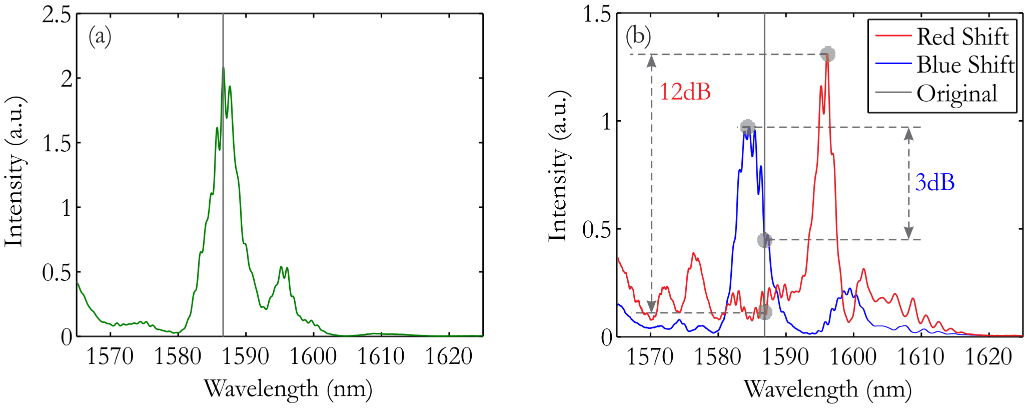

Figure 5.14: (a) Probe spectrum at the output of the a-Si:H fibre in the absence of the pump pulse (i.e., no XPM). (b) Largest red and blue shifts observed from the XPM process. Grey line indicates original centre of probe pulse. Extinction ratios are calculated with respect to the original probe's centre wavelength.

the extinction ratio. By analysing the spectral power density of the probe wavelength, a calculation can be made between the spectral peak at the largest wavelength shift relative to the 1587 nm unshifted probe peak.

Figure 5.14(a) shows the measured spectral profile taken at the output of the a-Si:H fibre in the absence of a pump. The solid grey line marks the peak wavelength of the probe. Figure 5.14(b) plots the spectra for delays corresponding to the largest blue and red-shifts. The solid grey line again represents the point in each spectrum that corresponds to the original probe. From this spectral data, the contrast of the 10 nm red-shift at 1597 nm yields a spectral extinction of ~ 12 dB while the smaller blue-shift at 1583 nm yields a reduced extinction of 3 dB. The red-shift represents more than 90 % conversion of the original probe's power which is comparable (if not higher) to many nonlinear optical switching techniques [178].

Simulations suggest that in the absence of nonlinear absorption, more symmetric conversion can be achieved which is apparent from Figure 5.6. The extinction ratio can also be improved through the use of shorter optical pulses, though the presence of free carriers and their long lifetimes can restrict the use of this switching mechanism to low data rates as seen in Chapter 4. Higher data rates could be employed though it will depend on how much extinction one is willing to sacrifice.

5.4 Conclusion

Two fundamental nonlinear refraction mechanisms were investigated in a-Si:H fibres. SPM and XPM. Through SPM, the Kerr nonlinear coefficient and figure of merit for these fibres were established. The n_2 values obtained were of similar magnitude to those reported in literature on c-Si and a-Si:H planar waveguides. From the FOM$_{NL}$ it was shown that a-Si:H fibres operate better than many of the current a-Si:H planar platforms. With many of the nonlinear parameters established, XPM was investigated to show spectral modulation and ultrafast wavelength conversion with high extinction. The process revealed detailed insight into the relative magnitudes of Kerr based processes competing against free carrier based processes. Even with the large nanosecond carrier lifetimes of these fibres, the Kerr nonlinearity was not hindered and instead displayed a delicate interplay of Kerr and free carrier mechanisms, ultimately demonstrating high speed and modest conversion for nonlinear switching through XPM.

Chapter 6

Towards Mid-Infrared Applications

6.1 Introduction

The ability to impregnate optical fibres with silicon and the associated applications in the near-infrared (NIR) wavelength region have been discussed in the previous chapters. Benefits of silicon in NIR signal processing are well known and have attracted great interest [179], however operation in the mid-infrared (MIR) is starting to receive more attention due to the potential applications. With a range of MIR possibilities including gas detection, environmental monitoring and industrial process control, silicon offers the prospect of optical components exploiting an inherent transparency from $\sim 1-9\,\mu$m [180] satisfying these applications. However, materials that supersede the MIR transparency and nonlinear strength of silicon, e.g., germanium are also of growing interest in the research community. This chapter focuses on the preliminary characterisation of hydrogenated amorphous silicon (a-Si:H) and germanium (a-Ge:H) fibres for applications in the MIR.

6.2 Motivation

MIR transmission in optical fibres commonly refers to wavelengths beyond $2\,\mu$m. Several applications exist that specifically utilise the atmospheric transmission windows from $3-5\,\mu$m and $8-12\,\mu$m. These applications include free-space communications, biomedical or chemical sensing, military applications, and thermal imaging [17]. A number of optical fibre platforms are able to transmit in the mentioned MIR windows. Such fibres include soft glasses (e.g., fluorides, chalcogenides), and hollow core silica fibres [41]. Soft glasses have low melting or softening points leading to optically and mechanically more

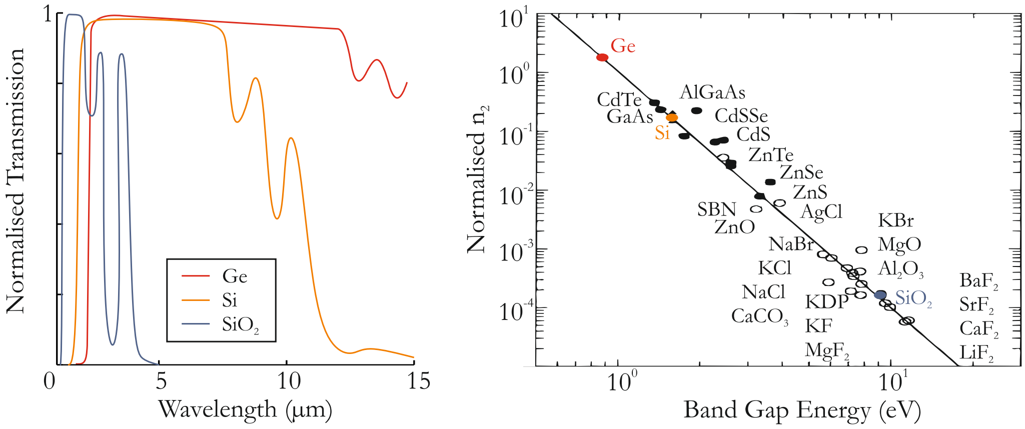

(a) (b)

Figure 6.1: (a) Transmission profiles of silicon, germanium, and silica. (b) Material nonlinearities from [11].

delicate fibres than those which are silica based [181]. Furthermore, many silica fibre compositions require large (metres to kilometres) interaction lengths for their nonlinear strength to be appreciable. An ideal fibre material would exhibit properties such as high optical damage thresholds, strong mechanical strength, and high optical nonlinearity to reduced the device footprint. Silicon and germanium are two semiconductors that possess these features, in addition to extended transmission windows relative to silica and several soft glasses.

Figure 6.1(a) is a comparison of the optical transmission in these semiconductors with silica shown as a reference. It can be seen that the broadest window of transparency occurs in germanium, though lasers in this broad transparency region of $2 - 14\,\mu$m are scarcely available due to cost and complexity. A promising method for easily overcoming the generation of coherent MIR light is to utilise nonlinear optical effects in fibres such as parametric amplifiers [182], oscillators [183], and Raman lasing [184]. For these effects to operate efficiently, a high nonlinear coefficient n_2 is required. Figure 6.1(b) represents theoretical and experimental indications of how the relative n_2 varies with respect to the band gap energies of a material.

6.2.1 Silicon

Silicon has a high n_2 as indicated in Figure 6.1(b). The strong nonlinearity allows for the potential of nonlinear optical devices to be highly efficient assuming negligible nonlinear absorption. Yet undesired nonlinear absorption such as two-photon absorption (TPA) is only negligible beyond 2200 nm as the energy of two-photons is not enough for a band-to-band transition [185]. Detailed investigations have been performed by a number of research groups to understand the limits in which nonlinear absorption mechanisms can begin to be ignored. The variation in the two-photon absorption (TPA) strength β_{TPA},

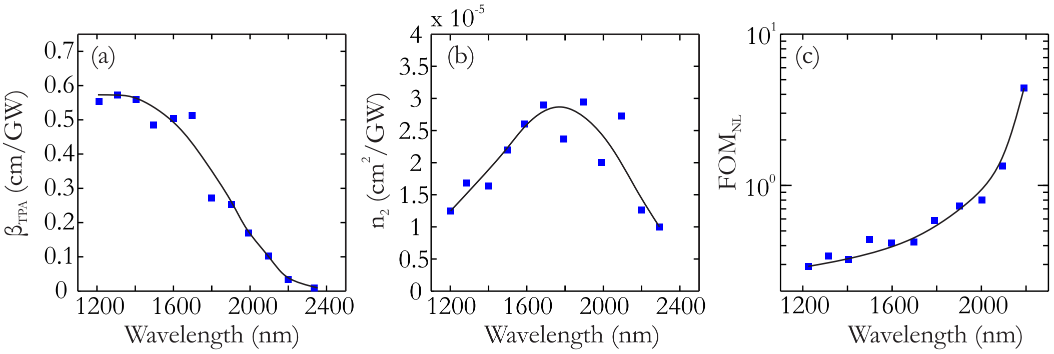

Figure 6.2: Dispersion of nonlinearities in single crystal silicon by Q. Lin *et al.* [116]. The blue squares are experimental measurements and the solid blacks lines are theoretical trends. (a) TPA dispersion. (b) Kerr nonlinearity dispersion. (c) FOM_{NL} dispersion.

Kerr nonlinearity n_2, and figure of merit as a function of wavelength were characterised. The wavelength variation (or dispersion) of these nonlinear properties were characterised in detail by Q. Lin *et al.* in a single crystal silicon (c-Si) wafer [116] using the well known Z-scan technique [186]. Figure 6.2(a) presents the dispersion of the dominant nonlinear absorption mechanism, TPA, which in turn induces free carrier absorption. As expected, TPA dramatically reduces to near zero for wavelengths beyond half the band gap energy ($\lambda \sim 2200\,\mathrm{nm}$ for c-Si). However, the Kerr nonlinearity in Figure 6.2(b) peaks at 1900 nm and decreases with a further increase in wavelength. While it may appear that the nonlinearity diminishes at MIR wavelengths, it is important to re-introduce the nonlinear figure of merit FOM_{NL} defined in Equation 5.10 which facilitates the comparison between nonlinear materials. By this analysis, Figure 6.2(c) clearly illustrates that the c-Si has an order of magnitude larger FOM_{NL} beyond the TPA edge for a low n_2 as opposed to where n_2 is relatively modest at shorter wavelengths, thereby justifying a significant motivation to investigate silicon in the MIR for nonlinear device applications.

6.2.2 Germanium

Germanium on the other hand has a usable transmission window extending even further from $2-14\,\mu\mathrm{m}$ as shown in Figure 6.1(a). This material thus presents a rare opportunity to explore a whole host of devices in unexplored regions of the MIR. The spectral region of $2-20\,\mu\mathrm{m}$ is a domain of particular interest due to the large number of molecules that undergo strong characteristic vibrational transitions, thus MIR spectroscopy serves as a definitive tool in identifying and quantifying molecular species [187]. In addition, germanium covers both the atmospheric transmission windows of $3-5\,\mu\mathrm{m}$ and $8-12\,\mu\mathrm{m}$ (mentioned earlier), in which Rayleigh scattering losses are lower. For this reason, important applications in security related spectroscopy and communications can benefit

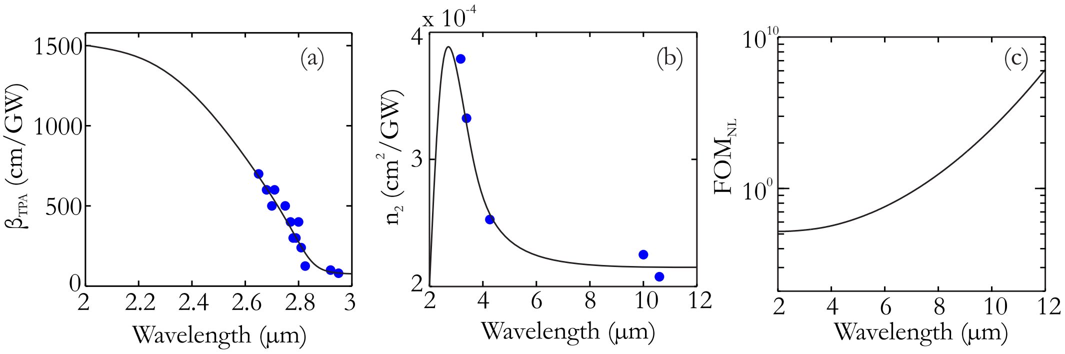

Figure 6.3: Dispersion of nonlinearities in single crystal germanium. (a) TPA dispersion from [185, 188]. (b) Kerr nonlinearity dispersion gathered from [185, 189–191]. (c) Theoretical FOM_{NL} dispersion.

from these transparency windows of the Earth's atmosphere. Use of spectroscopic and free space communication applications may require nonlinear media to play an important role for the development of MIR tunable laser sources and signal processing. It has been determined that the nonlinear coefficients of germanium exceeds those of most of the semiconductor alloys as well as the glasses, and thus is ideal for compact nonlinear devices. Furthermore, the higher refractive index of $n \sim 4.1$ leads to stronger light confinement, reducing the effective mode area and hence amplifying the nonlinear strength γ (Equation 2.48). Figure 6.1(b) emphasizes the magnitude of n_2 of germanium by the inversely proportional relationship with respect to the band gap energies in a number of materials. From the Z-scan technique, early measurements were used to confirm this significantly stronger nonlinearity in germanium. Theoretical and experimental results of germanium's nonlinear coefficients, β_{TPA} and n_2, gathered from multiple sources of literature, are shown in Figure 6.3(a) and (b). The TPA strength of germanium in its transparent regime is much stronger than that of silicon, although a sharp drop is observed in its strength before the TPA band edge of $\sim 3.8\,\mu$m. Similar to the silicon measurements of Figure 6.2(b), germanium experiences a peak in its Kerr nonlinearity near the TPA edge. For germanium, this occurs in the vicinity of $3\,\mu$m. Due to the nonlinear dispersion results of β_{TPA} and n_2 being at different wavelengths, an FOM_{NL} cannot be calculated. However, theoretical solutions (plotted by the solid black lines) obtained by N. K. Hon *et al.*, can be used to estimate the FOM_{NL} as shown in Figure 6.3(c). Similar to silicon, germanium is expected to show a dramatic increase in the FOM_{NL} as it extends beyond the TPA edge with a much higher order of magnitude increase relative to silicon.

The pursuit for highly nonlinear optical devices first requires a detailed understanding of a material's linear optical performance. However, due to the fabrication challenges of germanium waveguides [192], minimal reports on its transmission capabilities can be found in the literature. In this chapter, fabrication and material characterisation is performed on two germanium optical fibres with different core sizes. While still at an early stage in its development, the first comprehensive optical transmission loss measurements were able to be made from $2 - 10.6\,\mu$m in a germanium waveguide. A similar analysis is performed for silicon optical fibres deposited at different temperatures but for a limited range of MIR wavelengths.

6.3 Silicon Optical Fibres

The wide band gap of amorphous silicon (1.7 eV) implies a modest TPA strength in the c-band. However, it was shown earlier (Chapter 4) that this was not the case, and TPA strengths were of similar magnitude to single crystal silicon. By operating at longer MIR wavelengths the regime of minimal TPA can be found for a-Si:H, it is then possible to determine whether a larger FOM_{NL} as predicted by Figure 6.2(c) exists in a-Si:H. In order to see nonlinear effects we must have low linear losses. Thus the first step is to characterise the linear transmission properties of the fibres in this new wavelength regime.

To characterise the MIR transmission loss, a Cr^{2+}:ZnSe $(2 - 2.6\,\mu\mathrm{m})$ continuous wave (CW) laser, an Aculight Argos CW OPO $(2.7 - 3.3\,\mu\mathrm{m})$, and 25.4 mm focal length ZnSe objectives were used in a standard launch-in launch-out configuration, like that of Figure 3.9. The input (set at 1 mW) and output powers were measured using a PbSe preamplified photo detector. Two different a-Si:H samples were characterised with the cut-back technique (Section 3.5.3), each deposited at peak temperatures of 450 °C and 394 °C. The losses are plotted in Figure 6.4 along with selected mode images at the output of the a-Si:H fibre imaged using a Spricon Pyrocam III Series camera. Interestingly there did not appear to be a significant difference in the MIR losses, however the associated NIR transmission (from Figure 3.12(b) for the 394 °C fibre) were significantly different ($\Delta\alpha_{\mathrm{dB}} \sim 5\,\mathrm{dB/cm}$ at $1.6\,\mu$m). Hence, two different scattering fits are presented. Each fit corresponds to the best NIR and MIR fit for the 450 °C and 394 °C samples. It is unclear how the influence of the deposition temperature affects the NIR transmission specifically. From the multiple fits of absorption mechanisms highlighted in Section 3.5.3, it was however shown that high losses in the NIR are a result of a higher Urbach energy, hence defect states cause a larger space-charge environment for dangling bond absorption to occur [110]. This is further confirmed by the higher deposition temperature fibre resulting in a higher NIR loss, leading to a higher portion of hydrogen diffusion from the core material. Comprehensive transmission investigations $(1.3 - 4\,\mu\mathrm{m})$ of samples with differing deposition temperatures are thus required in order to establish regions over which Rayleigh trends depart from one another, thereby indicating contribution to the losses from alternative mechanisms.

The output mode images in Figure 6.4 show the spot size noticeably decreasing as the input wavelength is increased. This could be due to the fibre supporting less modes

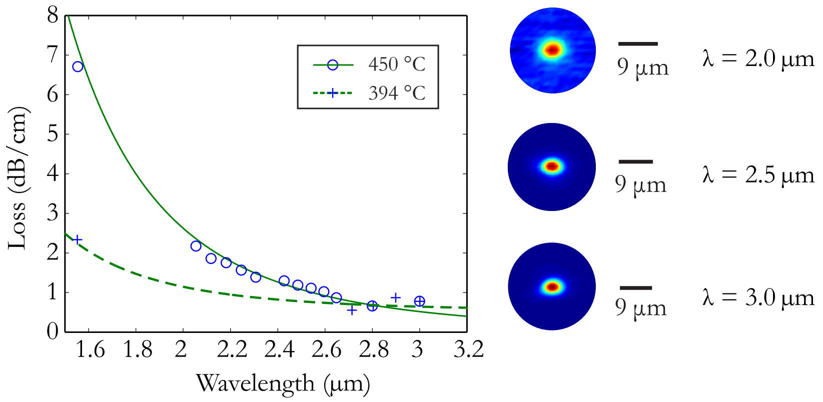

Figure 6.4: a-Si:H MIR loss results and measured output mode images. Green lines represent Rayleigh fitting to the NIR and MIR loss measurements.

consequently leading to the output spot focussing to the fundamental mode's diffraction limit, or simply that less power is coupled into the higher order circularly symmetric modes so that they are not detected.

This discovery of low linear transmission loss in the a-Si:H fibres in the MIR have led to ongoing investigations of nonlinear characterisation in the MIR. Currently, wavelength dependent TPA and Kerr coefficients are being characterised to demonstrate how much the FOM_{NL} benefits in these fibres.

6.4 Germanium Optical Fibres

6.4.1 Fabrication

The fabrication of germanium fibres follows the process described in Section 3.3. A mixture of germane diluted in a helium carrier gas ($\mathrm{GeH_4/He}$) is forced to flow through the central hole of a 125 μm outer diameter fused silica capillary at pressures of ~ 35 MPa. Germanium is deposited at a relatively low temperature of $\sim 300\,^{\circ}$C so that the material grows in an amorphous state. Similar to the silicon depositions, the low deposition temperature suppresses the out diffusion of hydrogen, so that a percentage will remain in the semiconductor core material to passivate the dangling bonds. Furthermore, it was mentioned in Section 3.5.2.3 that the Si-H bond-dissociation energy is ~ 314 kJ/mole. For the Ge-H bond, the dissociation energy is even lower at ~ 285 kJ/mole [193], thus lower temperature (and hence lower energy) deposition aids in the minimisation of hydrogen diffusion from Ge-H. Though it should be noted that lower deposition temperatures (with respect to a-Si:H) in turn reduces the rate of precursor decomposition, so that the deposition times are longer.

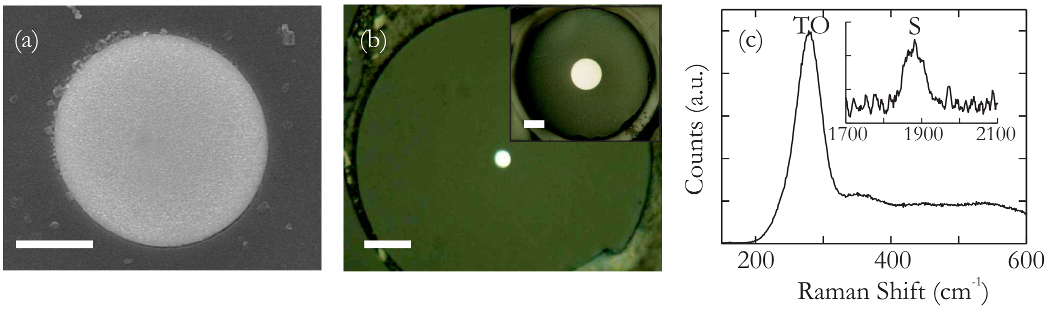

Figure 6.5: (a) SEM of a 6 μm germanium core; scale bar is 2 μm. (b) Microscope images of a 6 μm and 30 μm (inset) germanium core; both scale bars are 20 μm. (c) Raman spectra of a-Ge:H

6.4.2 Material Characterisation

Two germanium fibres were fabricated with core diameters of 6 μm and 30 μm. A scanning electron microscope (SEM) image of the 6 μm fibre confirmed complete filling of the capillary templates, as shown in Figure 6.5(a). In addition, Figure 6.5(b) shows an optical microscope image of the polished and completely filled 6 μm core fibre, with the 30 μm core fibre shown in the inset. Both fibres had a filled length of $\sim$ 3 cm. The core materials were characterised using micro-Raman spectroscopy on a Renishaw inVia system with a 633 nm HeNe laser source. A 100× objective was used to focus 250 μW of power in a 0.4 μm spot directly onto the polished germanium cores with a 10 s acquisition time, producing a spectrum of the backscattered radiation as shown in Figure 6.5(c). This Raman spectrum shows a broad peak, indicative of an amorphous material, around 280 cm^{-1}, which is slightly shifted from the transverse optical Raman resonance of 278 cm^{-1} for amorphous germanium [194, 195]. This observed shift is due to a difference in thermal expansion coefficients of silica and germanium, so that cooling from the elevated deposition temperatures will induce thermal mismatch stresses. The shift can quite often go unnoticed depending on the level of material disorder. At high detunings, evidence of hydrogenation is indicated by the peak at $\sim$ 1890 cm^{-1} [195], as shown in the inset of Figure 6.5(c), which is associated with the Ge–H stretching mode. This stretch mode can also be split with a second vibration (of Ge–H_2) appearing at $\sim$ 2000 cm^{-1} when higher levels of hydrogen are incorporated, though preliminary observations only show a single peak suggesting that the hydrogen content is low [194].

6.4.3 Mid-Infrared Transmission

In the fabrication of semiconductor optical fibres, a thermal gradient exists across the furnace during deposition. Consequently, a variation in the hydrogen content over the fibre length leads to dangling bond absorption varying in strength across the fibre length.

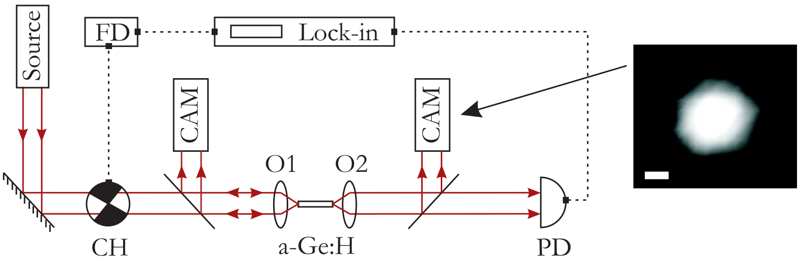

Figure 6.6: Experimental layout for transmission measurements of the germanium core fibre. Output mode image has a scale bar of 4 μm. (Source) is either a CO_2 laser, HeNe laser, or the Radiantis OPIUM OPO, (FD) Frequency driver, (CH) chopper, (CAM) camera, (PD) photodetector.

Since the cut-back method described in Section 3.5.3.1 isolates the fibre loss of a particular fibre section, the method thus produces variations in the fibre loss for every section of fibre measured. In silicon the variation is typically negligible, however, in the deposition of germanium the fabrication process is much more sensitive leading to large differences in the longitudinal material quality. Therefore in all cases of the germanium fibre, the single pass measurement technique was deemed to be the most appropriate in determining the average loss value at a given wavelength, where each loss was corrected for the respective Fresnel reflection coefficients of germanium and coupling efficiency.

The optical transmission properties of the germanium fibres were measured using various laser sources over the wavelength range $2 - 11\,\mu$m using an arrangement illustrated in Figure 6.6. Wavelengths below 2 μm were not considered as band edge absorption is too large. The wavelength range of $2-2.4\,\mu$m was accessed with a Radiantis OPIUM optical parametric oscillator (OPO) pumped via a Spectra-Physics Mai Tai laser operating at 80 MHz. The short 250 fs pulses delivered by this OPO system were limited to low average input powers of $\sim 100\,\mu$W to avoid nonlinear absorption associated with two-photon effects. Due to the high transmission loss of the germanium fibres, the 3 cm long fibre was shortened to 5 mm. The light was then launched into the core of the 5 mm long germanium fibre via free-space coupling using the ZnSe microscope objective lenses (O1 and O2) from the silicon transmission experiment. Piezo controlled nano-positioning stages were used to ensure precision coupling into and out of the fibre. The input and output faces of the fibre were imaged using a Spricon Pyrocam III Series camera (CAM) from which it could be easily identified when the light was well confined to the high refractive index ($n \sim 4.1$) core (due to the high reflection) [196]. The beam profile image in Figure 6.6 is taken at the output of the 6 μm a-Ge:H fibre at 2 μm where a broad distribution of intense light is shown to cover a large area. The image confirms the multimode nature of the waveguide since a single-mode beam would focus to a diffraction limited spot size. The input and output powers were measured again using the PbSe photo detector (PD), though implemented in a lock-in detection circuit

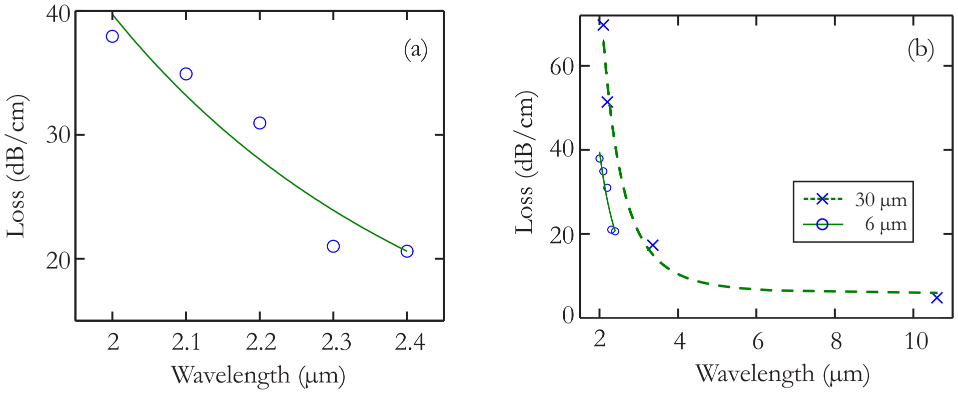

Figure 6.7: Linear transmission loss for (a) 6 μm core diameter a-Ge:H fibre, and (b) 30 μm core diameter a-Ge:H fibre.

as described in Section 4.6.2. This was necessary as the losses for the a-Ge:H fibre were significantly higher than the a-Si:H fibres.

The transmission losses of the 6 μm core fibre are presented in Figure 6.7(a). The trend from the data points alone do not exhibit any clear features indicative of the Urbach tail or Rayleigh scattering. However, the overall decrease in loss for increasing wavelength is fitted well with a λ^{-4} dependence associated with Rayleigh scattering. It provides a reasonable agreement considering the band edge proximity $\lambda_{bg} \sim 1.9\,\mu$m (0.67 eV) and the difficulty in achieving very high sensitivity measurements for the high losses in this particular wavelength regime. Nevertheless, these loss values are comparable to those of the early amorphous silicon optical fibres measured at $\sim 1.55\,\mu$m, and these losses have since been reduced by increasing the amount of hydrogen incorporation as described in Section 3.5.3 and 3.5.3.4. Further transmission investigations are required on a number of 6 μm core germanium fibres to establish the true contributions of loss in this wavelength region. Loss measurements at the longer wavelengths of 3.39 μm and 10.6 μm were conducted on the 30 μm diameter core fibre owing to the difficulty in coupling into the smaller core structure. The laser sources used at these wavelengths were both continuous wave (CW), where at 3.39 μm a HeNe laser was used with an input power of $\sim$ 12 mW and at 10.6 μm a CO_2 laser was used with an input of $\sim$ 30 mW. In both cases the output light was focussed onto a Laser Probe Inc. RK-5720 thermal power meter, with a RKP-575 detector head. The losses measured at these two wavelengths were 17.3 dB/cm at 3.39 μm and a much reduced value of 4.8 dB/cm at 10.6 μm. To compare this large core fibre the losses of the smaller core fibre, measurements were also conducted around 2 μm using the OPO and the results obtained over the entire wavelength range are plotted in Figure 6.7(b) (crosses) together with the results of the 6 μm core fibre from Figure 6.7(a) (circles). The good agreement between the results for the 30 μm core fibre and the λ^{-4} fit (dashed line) provides further evidence that the losses in these fibres are dominated by scattering mechanisms [197]. By comparing the results for the two fibres it is clear that, in this case, the smaller core fibre exhibits the lower material loss. At this stage, it is unclear exactly whether the difference is due to an increase in hydrogen content or a higher uniformity in the deposited material. Further investigations which involve detailed Raman spectroscopy combined with characterisations of the optical transmission properties are required to better understand the origins of the losses.

It should be noted that nonlinear absorption measurements in the 6 μm fibre were attempted using the pulsed femtosecond OPO, though the high losses hindered the ability for an input pulse to induce two-photon absorption. Nonlinear measurements in the 30 μm fibre were not attempted due to the lack of high peak power sources within the low loss wavelength region ($> 6\,\mu$m). Furthermore, the much larger mode field area in the 30 μm core diameter would require an impractical level of peak power to induce nonlinear effects.

6.5 Conclusion

A loss of 0.7 dB/cm at 2.7 μm marks the lowest recorded loss to date in a a-Si:H fibre. a-Si:H fibres have also very recently been able to demonstrate nonlinear transmission in the MIR such as nonlinear absorption and refraction [198]. The first demonstration of hydrogenated germanium core optical fibres were investigated. Fabrication, material characterisation, and optical characterisations were performed on two different a-Ge:H core diameters. Rayleigh scattering has been identified as the dominant loss mechanism for germanium fibres, suggesting that uniformity in the material composition and density is still to be optimized. From a comparative perspective, the MIR losses presented for a-Si:H are considerably lower than that for a-Ge:H, though it should be noted that considerable effort in the past few years have been dedicated to improving the fabrication parameters to achieve low loss in a-Si:H.

Chapter 7

Conclusions

Standard 125 μm silica cladding optical fibres with semiconductor core materials were fabricated using a novel high pressure chemical deposition technique. 6 μm and 2 μm silicon core diameter fibres were the focus of this work. In Chapter 3, the four different material phases c-Si, p-Si, a-Si, and a-Si:H showed very different optical properties. From the Raman emission spectra, the p-Si fibres exhibited a narrow linewidth resonance which is also characteristic of c-Si material, though it is clear that the material does not represent c-Si as the linewidth and resonance position was slightly broader and shifted to bulk c-Si. The optical transmission revealed a loss at 1.55 μm to be $\sim$ 7 dB/cm, a value that was strongly dependent on the annealing temperature. a-Si fibres however, exhibited broad Raman resonances that are a superposition of multiple vibrational modes as expected of an amorphous material. Since the optical losses are very poor for a-Si (50 dB/cm at 1.55 μm), wavelength dependent measurements were not conducted. However, by lowering the deposition temperature used to fabricate the a-Si fibres, it is possible to leave much of the hydrogen content from the silane precursor within the deposited material. The resulting composition known as a-Si:H exhibited a far superior performance for both linear and nonlinear optical propagation. While it was inconclusive to determine whether the strength of the Si-H resonances from the Raman spectra could be correlated to the optical transmission, the lowest loss of the 6 μm core diameter fibre was 0.8 dB/cm at 1.54 μm, which is much lower than the 2 μm core fibre measuring 2.9 dB/cm.

Several a-Si:H fibres that exhibited a long effective length were able to exhibit nonlinear behaviour. Effects such as nonlinear absorption and refraction revealed information about the strength of coefficients related to each process. In nonlinear absorption, the TPA and FCA coefficients were very similar between four different a-Si:H fibres fabricated with different precursor pressures. The average value of $\beta_{\mathrm{TPA}} \sim 8 \times 10^{-12}$ m/W for the a-Si:H fibres is very similar to that of a-Si:H and c-Si materials investigated by other groups on planar substrates. Furthermore, $\sigma_{\mathrm{FCA}} \sim 1 \times 10^{-20}\,\mathrm{m}^2$ is in good agreement with that predicted via the Drude-Lorenz model for an ideal semiconductor ($\sigma_{\mathrm{FCA}} \sim 1.6 \times 10^{-20}\,\mathrm{m}^2$).

A strong correlation was observed between the quality of the material and the carrier lifetime. Low loss a-Si:H fibres exhibited a large carrier lifetime in excess of 200 ns whilst higher loss fibres or alternatively, smaller core fibres, showed shorter lifetimes where the lowest recorded was ~ 4 ns. From these investigations, it can be concluded that it is more efficient to develop $2\,\mu$m (or smaller) core fibres and optimize the deposition conditions to produce lower transmission losses, since the significant reduction in carrier lifetime and the addition of an enhanced nonlinearity (via a smaller A_{eff}), is a more beneficial route for all-optical device applications. One example in which all-optical modulation was shown, was using a $6\,\mu$m core a-Si:H fibre. Extinctions of up to 4 dB were demonstrated, which is a factor of more than 2.5× reduction in the incident optical probe power. This extinction is largely determined by the degenerate and non-degenerate TPA parameters, and these coefficients are also material dependent. While a slight improvement in this extinction could also be demonstrated by employing a fibre with a smaller core, it may be more powerful to develop a route to incorporate higher TPA materials such as direct band-gap semiconductors [199].

The a-Si:H fibres that were characterised for their nonlinear absorption were again investigated with the aim to determine the strength of their Kerr nonlinearity n_2. The Kerr effect is responsible for many all-optical signal processing applications as already mentioned in Chapter 1. By knowing all of the loss coefficients related to the GNLSE, it was shown that the optical spectrum at the output of the a-Si:H fibre is sufficient to accurately estimate n_2 provided strong SPM is present. Through numerical fitting of multiple SPM spectra, the highest Kerr nonlinearity estimated was $18.5 \times 10^{-18}\,\mathrm{m}^2/\mathrm{W}$ in a fibre with a loss of 1.7 dB/cm. In comparison to other a-Si:H and c-Si platforms this value is at the upper range, though not significant enough to show potential for large phase shift ($> 4\pi$) applications as suggested by the nonlinear figure of merit. An attempt to exploit the ultrafast behaviour of the Kerr nonlinearity was shown through XPM. Two different probe pulse regimes were implemented. The most notable results were for the short 800 fs probe pulse. In this experiment, it was shown that the a-Si:H fibre under test was able to shift an optical carrier 6 nm within 100 fs. This behaviour demonstrates the potential for ultrafast all-optical signal processing introduced at the start of this thesis. Despite the presence of nonlinear absorption, the high Kerr nonlinearity was sufficient to demonstrate a spectral extinction as high as 12 dB of the shifted carrier.

Magnitude, speed, and efficiency, were the three most important attributes characterised relative to specific nonlinear optical processes. These characterisations were performed at conventional telecommunication wavelengths since a plethora of low and high power sources and/or detectors are readily available. Silicon has more recently been gaining interest at transmission wavelengths beyond $2\,\mu$m owing to its large nonlinear figure of merit. For this reason, a preliminary MIR characterisation was performed using currently available laser sources. Two 6 μm a-Si:H fibres had demonstrated very similar optical losses of < 1 dB at 2.8 μm showing that a Rayleigh scattering like dependence was the fundamental limiting factor in the MIR. It is anticipated that MIR nonlinearities should likewise be enhanced not only due to the lower optical losses, but also because the TPA strength diminishes due to insufficient photon energies.

An alternative material that has been shown to possess one of the highest nonlinearities amongst many semiconductors is germanium. This material has been studied by few groups with the aim to achieve low optical loss planar waveguides and is still an ongoing field of research. The final focus of this thesis was the fabrication of an a-Ge:H fibre using a germane precursor. The Ge-H Raman resonance was very weak which could indicate a poor concentration of hydrogen. The initial transmission measurements of a 6 μm core diameter fibre revealed high optical losses of ~ 20 dB/cm at 2.4 μm, though this type of fibre is still in the early stages of its development. For a 30 μm core diameter fibre, the predicted loss through Rayleigh fitting at 2.4 μm is much larger at > 40 dB/cm. This work however, requires a large amount of a-Ge:H samples to be fabricated and optically characterised in order to gauge an understanding of how the material quality varies, similar to what was done for the silicon optical fibres.

The research performed in this thesis provides the first comprehensive linear and nonlinear evaluation of several key optical parameters in a-Si:H fibres. The nonlinear strength γ between the different silicon fibres was found to be in the range of $4000 - 5000\,\mathrm{W^{-1}km^{-1}}$. This is 4000× larger than conventional silica core fibres. Many nonlinear applications currently employing silica fibres could also be realised with silicon fibres, potentially demonstrating higher efficiencies in a more compact form. Apart from nonlinear applications, many challenges still need to be addressed. The semiconductor fibre platform could dramatically benefit through features such as being single-moded, having the flexibility to perform dispersion engineering, and seamless integration with conventional silica fibres. These features are currently ongoing areas of research.

Appendix A

Non-Degenerate TPA Solution

The solution to Equation 2.41 is found using the prescribed methods; separation of variables, integration by substitution, evaluation of the integration constants, and finally obtaining the optical intensity from the amplitude using Equation 2.31:

$$\frac{dA_s(z,t)}{dz} = -\beta_{\mathrm{TPA}p,s} I_p(z,t) A_s(z,t) \tag{A.1}$$

$$\int \frac{1}{A_s(z,t)} dA_s = -\beta_{\mathrm{TPA}p,s} \int I_p(z,t) dz. \tag{A.2}$$

Using the solution for the pump pulse in Equation 2.34 yields

$$\int \frac{1}{A_s(z,t)} dA_s = -\beta_{\mathrm{TPA}p,s} \int \frac{I_{0p}(t)}{I_{0p}(t)\beta_{\mathrm{TPA}p,p} z + 1} dz \tag{A.3}$$

$$\ln[A_s(z,t)] + C = -\beta_{\mathrm{TPA}p,s} I_{0p}(t) \int \frac{1}{u} \frac{1}{I_{0p}(t)\beta_{\mathrm{TPA}p,p}} du \tag{A.4}$$

where the following substitutions were made:

$$u = I_{0p}(t)\beta_{\mathrm{TPA}p,p} z + 1 \tag{A.5}$$

$$\frac{du}{dz} = I_{0p}(t)\beta_{\mathrm{TPA}p,p} \tag{A.6}$$

$$\therefore dz = \frac{du}{I_{0p}(t)\beta_{\mathrm{TPA}p,p}}. \tag{A.7}$$

Simplifying and evaluating the RHS integral:

$$\begin{aligned}
\ln[A_s(z,t)] + C &= -\frac{\beta_{\mathrm{TPA}p,s}}{\beta_{\mathrm{TPA}p,p}} \int \frac{1}{u} du \\
&= -\frac{\beta_{\mathrm{TPA}p,s}}{\beta_{\mathrm{TPA}p,p}} \ln[u] \\
&= -\frac{\beta_{\mathrm{TPA}p,s}}{\beta_{\mathrm{TPA}p,p}} \ln[I_{0p}(t)\beta_{\mathrm{TPA}p,p} z + 1] \\
&= \ln\left[(I_{0p}(t)\beta_{\mathrm{TPA}p,p} z + 1)^{-\frac{\beta_{\mathrm{TPA}p,s}}{\beta_{\mathrm{TPA}p,p}}} \right].
\end{aligned} \tag{A.8}$$

Taking the exponential of both sides and re-assigning the integration constant $\exp(C) \equiv D$:

$$A_s(z,t)\exp(C) = [I_{0p}(t)\beta_{\mathrm{TPA}p,p} z + 1]^{-\frac{\beta_{\mathrm{TPA}p,s}}{\beta_{\mathrm{TPA}p,p}}} \tag{A.9}$$

$$A_s(z,t) = \frac{D}{[I_{0p}(t)\beta_{\mathrm{TPA}p,p} z + 1]^{\frac{\beta_{\mathrm{TPA}p,s}}{\beta_{\mathrm{TPA}p,p}}}}. \tag{A.10}$$

Introducing the initial condition that at $z = 0$ then $A_s(0,t) = A_{0s}(t)$:

$$A_{0s}(t) = \frac{D}{1^{\frac{\beta_{\mathrm{TPA}p,s}}{\beta_{\mathrm{TPA}p,p}}}} \tag{A.11}$$

$$A_{0s}(t) = D. \tag{A.12}$$

Substituting D and using Equation 2.31 gives:

$$A_s(z,t) = \frac{A_{0s}(t)}{[I_{0p}(t)\beta_{\mathrm{TPA}p,p} z + 1]^{\frac{\beta_{\mathrm{TPA}p,s}}{\beta_{\mathrm{TPA}p,p}}}} \tag{A.13}$$

$$\frac{A_s^2(z,t)}{A_{\mathrm{eff}}} = \frac{A_{0s}^2(t)/A_{\mathrm{eff}}}{[I_{0p}(t)\beta_{\mathrm{TPA}p,p} z + 1]^{\frac{2\beta_{\mathrm{TPA}p,s}}{\beta_{\mathrm{TPA}p,p}}}} \tag{A.14}$$

$$I_s(z,t) = \frac{I_{0s}(t)}{[I_{0p}(t)\beta_{\mathrm{TPA}p,p} z + 1]^{\frac{2\beta_{\mathrm{TPA}p,s}}{\beta_{\mathrm{TPA}p,p}}}}. \tag{A.15}$$

Appendix B

Free Carrier Density Rate Equation

The carrier density is assumed to be directly related to the number of photons absorbed by a material, hence a treatment of Equation 2.30 is then required in terms of a photon flux φ [$\mathrm{s^{-1}m^{-2}}$] (or photons absorbed per unit area):

$$\varphi = \frac{I(z,t)}{\hbar\omega}. \tag{B.1}$$

Since the rate of absorption due to TPA was shown to be proportional to $-\beta_{\mathrm{TPA}} I^2(z,t)$, it follows that the rate of absorption of the number of photons n_{ph} is then [200],

$$\begin{aligned} n_{\mathrm{ph}} &= -\frac{d\varphi}{dz} \\ &= -\frac{1}{\hbar\omega}\frac{dI}{dz} \\ &= \frac{\beta_{\mathrm{TPA}}}{\hbar\omega} I^2(z,t). \end{aligned} \tag{B.2}$$

The rate of carriers excited due to TPA will be half the number of absorbed photons since two-photons are required to generate one carrier:

$$\begin{aligned} \frac{dN}{dt} &= \frac{1}{2} n_{\mathrm{ph}} \\ &= \frac{\beta_{\mathrm{TPA}}}{2\hbar\omega} I^2(z,t). \end{aligned} \tag{B.3}$$

Generated carriers will exist in an excited state for a limited temporal lifetime τ. The rate of recombination is inversely proportional to the rate of change of the carrier density, so that Equation B.3 can be re-expressed as:

$$\frac{dN}{dt} = \frac{\beta_{\mathrm{TPA}}}{2\hbar\omega} I^2(z,t) - \frac{N(z,t)}{\tau}. \tag{B.4}$$

List of Publications

Journal Papers

1. **P.Mehta**, N.Healy, T.D.Day, J.V.Badding, A.C.Peacock, “Ultrafast wavelength conversion via cross-phase modulation in hydrogenated amorphous silicon optical fibers”, *Optics Express*, Vol.20 (24), 26110-26116(2012).
2. A.C.Peacock, **P.Mehta**, P.Horak, N.Healy, “Nonlinear pulse dynamics in multimode silicon core optical fibers”, *Optics Letters*, Vol.37 (16), 3351-3353 (2012).
3. N.Vukovic, N.Healy, **P.Mehta**, T.D.Day, P.J.A.Sazio, J.V.Badding, A.C.Peacock, “Thermal nonlinearity in silicon microcylindrical resonators”, *Applied Physics Letters*, Vol.100 (18), 181101 (2012).
4. **P.Mehta**, N.Healy, T.D.Day, J.R.Sparks, P.J.A.Sazio, J.V.Badding, A.C.Peacock, “All-optical modulation using two-photon absorption in silicon core optical fibers”, *Optics Express*, Vol.19 (20), 19078-19083 (2011).
5. **P.Mehta**, M.Krishnamurthi, N.Healy, N.F.Baril, J.R.Sparks, P.J.A.Sazio, V.Gopalan, J.V.Badding, A.C.Peacock, “Mid-infrared transmission properties of amorphous germanium optical fibers”, *Applied Physics Letters*, Vol.97, 071117 (2010).
6. **P.Mehta**, N.Healy, N.F.Baril, P.J.A.Sazio, J.V.Badding, A.C.Peacock, “Nonlinear transmission properties of hydrogenated amorphous silicon core optical fibers”, *Optics Express,* Vol.18 (16), 16826-16831 (2010).

Conference Papers

1. A.C.Peacock, **P.Mehta**, L. Shen, T.D.Day, J.R.Sparks, J.V.Badding, N.Healy, “Nonlinear properties of silicon optical fibers from telecoms to the mid-infrared”, *Photonics North*, Ottawa Canada, (Invited), 3 Jun (2013).
2. A.C.Peacock, **P.Mehta**, T.D.Day, J.R.Sparks, J.V.Badding, N.Healy, “Nonlinear optics in silicon core fibers”, *POEM/IONT*, Wuhan China, Session: Special Fiber and Its Applications, IF5B.3 (Invited), 2 Nov (2012).

3. **P.Mehta**, N.Healy, T.D.Day, P.J.A.Sazio, J.V.Badding, A.C.Peacock, "Cross-phase modulation induced frequency shifting in silicon optical fibers", *POEM*, Wuhan China, 1-2 Nov (2012).

4. **P.Mehta**, N.Healy, T.D.Day, P.J.A.Sazio, J.V.Badding, A.C.Peacock, "Characterisation of cross-phase modulation in a hydrogenated silicon optical fibre", *Photon 12*, Durham, 3-6 Sept (2012).

5. A.C.Peacock, **P.Mehta**, T.D.Day, J.R.Sparks, P.J.A.Sazio, J.V.Badding, N.Healy, "Nonlinear properties of silicon optical fibers", *FiO/LS XXVIII*, Rochester NY, FM4H.1 (Invited), 14-18 Oct (2012).

6. L.Shen, N.Healy, **P.Mehta**, T.D.Day, J.R.Sparks, J.V.Badding, A.C.Peacock, "Transmission properties of hydrogenated amorphous silicon optical fibers into the mid-infrared regime", *FiO/LS XXVIII*, Rochester NY, FM3H, 14-18 Oct (2012).

7. A.C.Peacock, **P.Mehta**, T.D.Day, J.R.Sparks, P.J.A.Sparks, J.V.Badding, N.Healy, "Nonlinear properties of silicon optical fibers", *Advanced Photonics Congress (SOF)*, Colorado, (Invited), 17-21 Jun (2012).

8. N.Vukovic, N.Healy, **P.Mehta**, A.C.Peacock, "Demonstration of Kerr nonlinearity in silicon microcylindrical resonators", *Advanced Photonics Congress (NP)*, Colorado, 17-21 Jun (2012).

9. **P.Mehta**, N.Healy, T.D.Day, P.J.A.Sazio, J.V.Badding, A.C.Peacock, "Cross-phase modulation in a hydrogenated amorphous silicon optical fiber", *Advanced Photonics Congress (NP)*, Colorado, 17-21 Jun (2012).

10. **P.Mehta**, N.Healy, T.D.Day, P.J.A.Sazio, J.V.Badding, A.C.Peacock, "Effect of core size on nonlinear transmission in silicon optical fibers", *CLEO/QELS*, San Jose, 6-11 May (2012).

11. **P.Mehta**, N.Healy, J.R.Sparks, T.D.Day, P.J.A.Sazio, J.V.Badding, A.C.Peacock, "Ultrafast all-optical modulation in silicon optical fibers", *FiO/LS XXVII*, San Jose CA, FMG2, 16-20 Oct (2011).

12. **P.Mehta**, N.Healy, J.R.Sparks, T.D.Day, P.J.A.Sazio, J.V.Badding, A.C.Peacock, "Nonlinear absorption and self-phase modulation in silicon optical fibres", *CLEO /Europe-EQEC*, Munich, CE4.4, 22-26 May (2011).

13. **P.Mehta**, N.Healy, R.Slavík, R.T.Watts, J.R.Sparks, T.D.Day, P.J.A.Sazio, J.V.Badding, A.C.Peacock, "Nonlinearities in silicon optical fibers", *OFC/NFOEC*, Los Angeles, 6-10 Mar (2011).

14. **P.Mehta**, N.Healy, N.F.Baril, M.Krishnamurthi, P.J.A.Sazio, V.Gopalan, J.V.Badding, A.C.Peacock, "Optical characterisation of germanium optical fibres", *Photon 10*, Southampton, 23-26 Aug (2010).

References

[1] J. Hecht, *City of light the story of fiber optics*. Oxford University Press, 2004.

[2] T. M. Monro and H. Ebendorff-Heidepriem, "Progress in microstructured optical fibers," *Annual Review of Materials Research*, vol. 36, pp. 467–495, 2006.

[3] M. A. Schmidt, N. Granzow, N. Da, M. Y. Peng, L. Wondraczek, and P. S. J. Russell, "All-solid bandgap guiding in tellurite-filled silica photonic crystal fibers," *Optics Letters*, vol. 34, no. 13, pp. 1946–1948, 2009.

[4] C. Kerbage, A. Hale, A. Yablon, R. S. Windeler, and B. J. Eggleton, "Integrated all-fiber variable attenuator based on hybrid microstructure fiber," *Applied Physics Letters*, vol. 79, no. 19, pp. 3191–3193, 2001.

[5] F. Benabid, J. C. Knight, G. Antonopoulos, and P. S. J. Russell, "Stimulated Raman scattering in hydrogen-filled hollow-core photonic crystal fiber," *Science*, vol. 298, no. 5592, pp. 399–402, 2002.

[6] T. T. Alkeskjold, J. Laegsgaard, A. Bjarklev, D. S. Hermann, Anawati, J. Broeng, J. Li, and S. T. Wu, "All-optical modulation in dye-doped nematic liquid crystal photonic bandgap fibers," *Optics Express*, vol. 12, no. 24, pp. 5857–5871, 2004.

[7] M. Fokine, L. E. Nilsson, A. Claesson, D. Berlemont, L. Kjellberg, L. Krummenacher, and W. Margulis, "Integrated fiber mach-zehnder interferometer for electro-optic switching," *Optics Letters*, vol. 27, no. 18, pp. 1643–1645, 2002.

[8] P. J. A. Sazio, A. Amezcua-Correa, C. E. Finlayson, J. R. Hayes, T. J. Scheidemantel, N. F. Baril, B. R. Jackson, D. J. Won, F. Zhang, E. R. Margine, V. Gopalan, V. H. Crespi, and J. V. Badding, "Microstructured optical fibers as high-pressure microfluidic reactors," *Science*, vol. 311, no. 5767, pp. 1583–1586, 2006.

[9] G. P. Agrawal, "Nonlinear fiber optics: its history and recent progress [invited]," *Journal of the Optical Society of America B-Optical Physics*, vol. 28, no. 12, pp. A1–A10, 2011.

[10] R. L. Sutherland, *Handbook of nonlinear optics*. Optical Engineering, New York: Marcel Dekker, 1996.

[11] R. W. Boyd, *Nonlinear optics.* Academic Press, 3rd ed., 2008.

[12] J. Leuthold, C. Koos, and W. Freude, "Nonlinear silicon photonics," *Nature Photonics*, vol. 4, no. 8, pp. 535–544, 2010.

[13] M. A. Foster, A. C. Turner, M. Lipson, and A. L. Gaeta, "Nonlinear optics in photonic nanowires," *Optics Express*, vol. 16, no. 2, pp. 1300–1320, 2008.

[14] D. Gloge, *Weakly Guiding Fibers*, vol. 10 of *Applied Optics.* 1971.

[15] G. P. Agrawal, *Nonlinear fiber optics.* Quantum electronics–principles and applications, Elsevier / Academic Press, 4th ed., 2007.

[16] G. P. Agrawal, *Fiber-optic communication systems.* Wiley series in microwave and optical engineering, Wiley-Interscience, 3rd ed., 2002.

[17] A. Mendez and T. F. Morse, *Specialty optical fibers handbook.* Academic Press, 2007.

[18] A. W. Snyder and J. D. Love, *Optical waveguide theory.* Science paperbacks, Chapman and Hall, 1983.

[19] W. v. Etten and J. v. d. Plaats, *Fundamentals of optical fiber communications.* Prentice Hall international series in optoelectronics, New York: Prentice Hall, 1991.

[20] A. W. Snyder and W. R. Young, "Modes of optical-waveguides," *Journal of the Optical Society of America*, vol. 68, no. 3, pp. 297–309, 1978.

[21] R. J. Black and L. Gagnon, *Optical waveguide modes : polarization, coupling, and symmetry.* New York: McGraw-Hill, 2010.

[22] R. S. Quimby, *Photonics and lasers : an introduction.* Wiley-Interscience, 2006.

[23] L. Brillouin, *Wave propagation and group velocity.* Academic Press, 1960.

[24] B. J. Frey, D. B. Leviton, and T. J. Madison, "Temperature-dependent refractive index of silicon and germanium," *Optomechanical Technologies for Astronomy, Pts 1 and 2*, vol. 6273, pp. J2732–J2732 1178, 2006.

[25] M. C. Gupta and J. Ballato, *The handbook of photonics.* Boca Raton: CRC/Taylor and Francis, 2nd ed., 2007.

[26] N. P. Barnes and M. S. Piltch, "Temperature-dependent sellmeier coefficients and non-linear optics average power limit for germanium," *Journal of the Optical Society of America*, vol. 69, no. 1, pp. 178–180, 1979.

[27] G. T. Reed and A. P. Knights, *Silicon photonics : an introduction.* Chichester ; Hoboken, NJ: John Wiley, 2004.

[28] J. Chu and A. Sher, *Physics and properties of narrow gap semiconductors.* Microdevices, Springer, 2008.

[29] R. A. Street, *Hydrogenated amorphous silicon.* Cambridge solid state science series, Cambridge University Press, 1991.

[30] J. I. Pankove, *Optical processes in semiconductors.* Prentice-Hall electrical engineering series Solid state physical electronics series, Englewood Cliffs, N.J.,: Prentice-Hall, 1971.

[31] T. S. Moss, G. J. Burrell, and B. Ellis, *Semiconductor opto-electronics.* London,: Butterworths, 1973.

[32] R. A. Soref and B. R. Bennett, "Electrooptical effects in silicon," *Ieee Journal of Quantum Electronics*, vol. 23, no. 1, pp. 123–129, 1987.

[33] M. Nedeljkovic, R. Soref, and G. Z. Mashanovich, "Free-carrier electrorefraction and electroabsorption modulation predictions for silicon over the 1-14um infrared wavelength range," *Ieee Photonics Journal*, vol. 3, no. 6, pp. 1171–1180, 2011.

[34] H. S. Rong, A. S. Liu, R. Jones, O. Cohen, D. Hak, R. Nicolaescu, A. Fang, and M. Paniccia, "An all-silicon Raman laser," *Nature*, vol. 433, no. 7023, pp. 292–294, 2005.

[35] Q. F. Xu, B. Schmidt, S. Pradhan, and M. Lipson, "Micrometre-scale silicon electro-optic modulator," *Nature*, vol. 435, no. 7040, pp. 325–327, 2005.

[36] A. C. Turner-Foster, M. A. Foster, J. S. Levy, C. B. Poitras, R. Salem, A. L. Gaeta, and M. Lipson, "Ultrashort free-carrier lifetime in low-loss silicon nanowaveguides," *Optics Express*, vol. 18, no. 4, pp. 3582–3591, 2010.

[37] M. Waldow, T. Plotzing, M. Gottheil, M. Forst, J. Bolten, T. Wahlbrink, and H. Kurz, "25ps all-optical switching in oxygen implanted silicon-on-insulator microring resonator," *Optics Express*, vol. 16, no. 11, pp. 7693–7702, 2008.

[38] T. J. Johnson and O. Painter, "Passive modification of free carrier lifetime in high-q silicon-on-insulator optics," *CLEO/QELS*, vol. 1-5, no. 2009, pp. 72–73 3405, 2009.

[39] W. H. P. Pernice, C. Schuck, M. Li, and H. X. Tang, "Carrier and thermal dynamics of silicon photonic resonators at cryogenic temperatures," *Optics Express*, vol. 19, no. 4, pp. 3290–3296, 2011.

[40] F. L. Pedrotti, L. M. Pedrotti, and L. S. Pedrotti, *Introduction to optics.* Upper Saddle River, N.J.: Pearson/Prentice Hall, 3rd ed., 2007.

[41] J. A. Harrington, *Infrared fibers and their applications.* Bellingham, Wash.: SPIE Optical Engineering Press, 2004.

[42] R. A. Serway, C. J. Moses, and C. A. Moyer, *Modern physics.* Belmont, CA: Thomson Brooks/Cole, 3rd ed., 2005.

[43] J. Graybeal, *Molecular Spectroscopy*, vol. 1. Mcgraw-Hill College, 1993.

[44] G. I. Stegeman and R. A. Stegeman, *Nonlinear optics : phenomena, materials, and devices.* Wiley series in pure and applied optics, Hoboken, N.J.: Wiley, 2012.

[45] P. A. Franken, G. Weinreich, C. W. Peters, and A. E. Hill, "Generation of optical harmonics," *Physical Review Letters*, vol. 7, no. 4, p. 118, 1961.

[46] M. Bass, A. E. Hill, P. A. Franken, C. W. Peters, and G. Weinreich, "Optical mixing," *Physical Review Letters*, vol. 8, no. 1, p. 18, 1962.

[47] R. M. Osgood, N. C. Panoiu, J. I. Dadap, X. Liu, X. Chen, I. W. Hsieh, E. Dulkeith, W. Green, and Y. Vlasov, "Engineering nonlinearities in nanoscale optical systems: physics and applications in dispersion-engineered silicon nanophotonic wires," *Advances in Optics and Photonics*, vol. 1, pp. 162–235, 2009.

[48] M. N. Islam, L. F. Mollenauer, R. H. Stolen, J. R. Simpson, and H. T. Shang, "Cross-phase modulation in optical fibers," *Optics Letters*, vol. 12, no. 8, pp. 625–627, 1987.

[49] G. S. He, Q. D. Zheng, K. T. Yong, A. I. Ryasnyanskiy, P. N. Prasad, and A. Urbas, "Two-photon absorption based optical limiting and stabilization by using a cdte quantum dot solution excited at optical communication wavelength of similar to 1300 nm," *Applied Physics Letters*, vol. 90, no. 18, 2007.

[50] E. K. Tien, N. S. Yuksek, F. Qian, and O. Boyraz, "Pulse compression and modelocking by using tpa in silicon waveguides," *Optics Express*, vol. 15, no. 10, pp. 6500–6506, 2007.

[51] A. Y. Hamad, J. P. Wicksted, S. Y. Wang, and G. Cantwell, "Spatial and temporal beam reshaping effects using bulk cdte," *Journal of Applied Physics*, vol. 78, no. 5, pp. 2932–2939, 1995.

[52] S. Fathpour and B. Jalali, *Silicon photonics for telecommunications and biomedicine.* Boca Raton, FL: CRC Press, 2012.

[53] Q. Lin, O. J. Painter, and G. P. Agrawal, "Nonlinear optical phenomena in silicon waveguides: Modeling and applications," *Optics Express*, vol. 15, no. 25, pp. 16604–16644, 2007.

[54] P. Mehta, N. Healy, T. D. Day, J. R. Sparks, P. J. A. Sazio, J. V. Badding, and A. C. Peacock, "All-optical modulation using two-photon absorption in silicon core optical fibers," *Optics Express*, vol. 19, no. 20, pp. 19078–19083, 2011.

[55] E. Garmire, “Nonlinear optics in semiconductors,” *Physics Today*, vol. 47, no. 5, pp. 42–48, 1994.

[56] M. Kira and S. W. Koch, *Semiconductor quantum optics.* Cambridge ; New York: Cambridge University Press, 2012.

[57] L. H. Yin, Q. Lin, and G. P. Agrawal, “Soliton fission and supercontinuum generation in silicon waveguides,” *Optics Letters*, vol. 32, no. 4, pp. 391–393, 2007.

[58] L. Banyai and S. W. Koch, “A simple theory for the effects of plasma screening on the optical-spectra of highly excited semiconductors,” *Zeitschrift Fur Physik B-Condensed Matter*, vol. 63, no. 3, pp. 283–291, 1986.

[59] A. Yariv, *Optical electronics in modern communications.* The Oxford series in electrical and computer engineering, New York: Oxford University Press, 5th ed., 1997.

[60] W. W. Chow and S. W. Koch, *Semiconductor-laser fundamentals : physics of the gain materials.* New York: Springer, 1999.

[61] R. W. Eason and A. Miller, *Nonlinear optics in signal processing.* Engineering aspects of lasers series, London: Chapman and Hall, 1st ed., 1993.

[62] D. K. Schroder, *Semiconductor material and device characterization.* Hoboken, N.J.: Wiley, 3rd ed., 2006.

[63] R. G. Hunsperger, *Integrated optics : theory and technology.* Advanced texts in physics, Springer, 6th ed., 2009.

[64] V. Raghunathan, *Raman-based silicon photonic devices.* PhD Thesis, University of California Los Angeles, USA, 2008.

[65] L. H. Yin and G. P. Agrawal, “Impact of two-photon absorption on self-phase modulation in silicon waveguides,” *Optics Letters*, vol. 32, no. 14, pp. 2031–2033, 2007.

[66] W. Yang, *Applied numerical methods using MATLAB.* Hoboken, N.J.: Wiley-Interscience, 2005.

[67] A. R. Hilton, *Chalcogenide glasses for infrared optics.* McGraw-Hill, 2010.

[68] S. A. Cerqueira, “Recent progress and novel applications of photonic crystal fibers,” *Reports on Progress in Physics*, vol. 73, no. 2, 2010.

[69] D. Graham-Rowe, “Fibres get functional,” *Nature Photonics*, vol. 5, no. 2, pp. 66–67, 2011.

[70] A. F. Abouraddy, M. Bayindir, G. Benoit, S. D. Hart, K. Kuriki, N. Orf, O. Shapira, F. Sorin, B. Temelkuran, and Y. Fink, "Towards multimaterial multifunctional fibres that see, hear, sense and communicate," *Nature Materials*, vol. 6, no. 5, pp. 336–347, 2007.

[71] N. D. Orf, O. Shapira, F. Sorin, S. Danto, M. A. Baldo, J. D. Joannopoulos, and Y. Fink, "Fiber draw synthesis," *Proceedings of the National Academy of Sciences of the United States of America*, vol. 108, no. 12, pp. 4743–4747, 2011.

[72] B. T. Kuhlmey, B. J. Eggleton, and D. K. C. Wu, "Fluid-filled solid-core photonic bandgap fibers," *Journal of Lightwave Technology*, vol. 27, no. 11, pp. 1617–1630, 2009.

[73] H. K. Tyagi, M. A. Schmidt, L. P. Sempere, and P. S. J. Russell, "Optical properties of photonic crystal fiber with integral micron-sized ge wire," *Optics Express*, vol. 16, no. 22, pp. 17227–17236, 2008.

[74] J. Ballato, T. Hawkins, P. Foy, R. Stolen, B. Kokuoz, M. Ellison, C. McMillen, J. Reppert, A. M. Rao, M. Daw, S. Sharma, R. Shori, O. Stafsudd, R. R. Rice, and D. R. Powers, "Silicon optical fiber," *Optics Express*, vol. 16, no. 23, pp. 18675–18683, 2008.

[75] J. Ballato, T. Hawkins, P. Foy, B. Yazgan-Kokuoz, R. Stolen, C. McMillen, N. K. Hon, B. Jalali, and R. Rice, "Glass-clad single-crystal germanium optical fiber," *Optics Express*, vol. 17, no. 10, pp. 8029–8035, 2009.

[76] J. Ballato, T. Hawkins, P. Foy, S. Morris, N. K. Hon, B. Jalali, and R. Rice, "Silica-clad crystalline germanium core optical fibers," *Optics Letters*, vol. 36, no. 5, pp. 687–688, 2011.

[77] J. Ballato, T. Hawkins, P. Foy, C. McMillen, L. Burka, J. Reppert, R. Podila, A. M. Rao, and R. R. Rice, "Binary iii-v semiconductor core optical fiber," *Optics Express*, vol. 18, no. 5, pp. 4972–4979, 2010.

[78] J. Ballato, T. Hawkins, P. Foy, B. Yazgan-Kokuoz, C. McMillen, L. Burka, S. Morris, R. Stolen, and R. Rice, "Advancements in semiconductor core optical fiber," *Optical Fiber Technology*, vol. 16, no. 6, pp. 399–408, 2010.

[79] J. Ballato, T. Hawkins, P. Foy, C. McMillen, R. Stolen, and R. R. Rice, "Optical materials: Semiconductor-core fiber promises novel nonlinear fiber-based devices," *OptoIQ, LaserFocusWorld*, vol. 47, no. 1, 2011.

[80] B. Scott, K. Wang, V. Caluori, and G. Pickrell, "Fabrication of silicon optical fiber," *Optical Engineering*, vol. 48, no. 10, pp. –, 2009.

[81] B. L. Scott, K. Wang, and G. Pickrell, "Fabrication of n-type silicon optical fibers," *Ieee Photonics Technology Letters*, vol. 21, no. 24, pp. 1798–1800, 2009.

[82] N. F. Baril, R. R. He, T. D. Day, J. R. Sparks, B. Keshavarzi, M. Krishnamurthi, A. Borhan, V. Gopalan, A. C. Peacock, N. Healy, P. J. A. Sazio, and J. V. Badding, "Confined high-pressure chemical deposition of hydrogenated amorphous silicon," *Journal of the American Chemical Society*, vol. 134, no. 1, pp. 19–22, 2012.

[83] J. Jang, J. Y. Oh, S. K. Kim, Y. J. Choi, S. Y. Yoon, and C. O. Kim, "Electric-field-enhanced crystallization of amorphous silicon," *Nature*, vol. 395, no. 6701, pp. 481–483, 1998.

[84] V. G. Erkov and S. F. Devyatova, "Polycrystalline-silicon lpcvd by silane pyrolysis: the effect of hydrogen injection," *Russian Microelectronics*, vol. 36, no. 2, pp. 120–126, 2007.

[85] T. N. Bell, K. A. Perkins, and P. G. Perkins, "Kinetics and mechanism of silane decomposition - silanes and disilanes containing si-h bonds," *Journal of Physical Chemistry*, vol. 88, no. 1, pp. 116–118, 1984.

[86] M. S. Gordon, D. R. Gano, J. S. Binkley, and M. J. Frisch, "Thermal-decomposition of silane," *Journal of the American Chemical Society*, vol. 108, no. 9, pp. 2191–2195, 1986.

[87] J. R. Sparks, H. Rongrui, N. Healy, S. Chaudhuri, T. C. Fitzgibbons, A. C. Peacock, P. Sazio, and J. V. Badding, "Conformal coating by high pressure chemical deposition for patterned microwires of iivi semiconductors," *Advanced Functional Materials*, vol. 10.1002, pp. 1–8, 2012.

[88] J. R. Sparks, R. R. He, N. Healy, M. Krishnamurthi, A. C. Peacock, P. J. A. Sazio, V. Gopalan, and J. V. Badding, "Zinc selenide optical fibers," *Advanced Materials*, vol. 23, no. 14, p. 1647, 2011.

[89] J. R. Sparks, J. L. Esbenshade, R. R. He, N. Healy, T. D. Day, D. W. Keefer, P. J. A. Sazio, A. C. Peacock, and J. V. Badding, "Selective semiconductor filling of microstructured optical fibers," *Journal of Lightwave Technology*, vol. 29, no. 13, pp. 2005–2008, 2011.

[90] N. Healy, J. R. Sparks, R. R. He, P. J. A. Sazio, J. V. Badding, and A. C. Peacock, "High index contrast semiconductor arrow and hybrid arrow fibers," *Optics Express*, vol. 19, no. 11, pp. 10979–10985, 2011.

[91] R. R. He, P. J. A. Sazio, A. C. Peacock, N. Healy, J. R. Sparks, M. Krishnamurthi, V. Gopalan, and J. V. Badding, "Integration of gigahertz-bandwidth semiconductor devices inside microstructured optical fibres," *Nature Photonics*, vol. 6, no. 3, pp. 174–179, 2012.

[92] M. K. Ghosh and K. L. Mittal, *Polyimides : fundamentals and applications*. Plastics engineering, New York: Marcel Dekker, 1996.

[93] N. H. Nickel, *Laser crystallization of silicon.* Semiconductors and Semimetals, Elsevier, 2003.

[94] K. Okamoto, *Fundamentals of optical waveguides.* Boston: Elsevier, 2nd ed., 2006.

[95] J. R. Ferraro, K. Nakamoto, and C. W. Brown, *Introductory Raman spectroscopy.* Boston: Academic Press, 2nd ed., 2003.

[96] D. A. Long, *The Raman effect : a unified treatment of the theory of Raman scattering by molecules.* Chichester: Wiley, 2002.

[97] P. Siffert and E. F. Krimmel, *Silicon : evolution and future of a technology.* Springer, 2004.

[98] M. H. Brodsky, M. Cardona, and J. J. Cuomo, "Infrared and Raman-spectra of silicon-hydrogen bonds in amorphous silicon prepared by glow-discharge and sputtering," *Physical Review B*, vol. 16, no. 8, pp. 3556–3571, 1977.

[99] L. Lagonigro, N. Healy, J. R. Sparks, N. F. Baril, P. J. A. Sazio, J. V. Badding, and A. C. Peacock, "Low loss silicon fibers for photonics applications," *Applied Physics Letters*, vol. 96, no. 4, 2010.

[100] R. A. Street and N. F. Mott, "States in gap in glassy semiconductors," *Physical Review Letters*, vol. 35, no. 19, pp. 1293–1296, 1975.

[101] R. T. Sanderson, *Chemical bonds and bond energy.* Physical chemistry, a series of monographs, Academic Press, 2d ed., 1976.

[102] K. Morigaki, *Physics of Amorphous Semiconductors.* World Scientific Pub Co Inc, 1999.

[103] E. F. Schubert, *Light-emitting diodes.* Cambridge: Cambridge University Press, 2nd ed., 2006.

[104] G. Wilfried, L. Korte, and F. Roca, *Physics and technology of amorphous-crystalline heterostructure silicon solar cells.* New York: Springer, 1st ed., 2011.

[105] I. A. Weinstein, A. F. Zatsepin, and V. S. Kortov, "Effects of structural disorder and urbach's rule in binary lead silicate glasses," *Journal of Non-Crystalline Solids*, vol. 279, no. 1, pp. 77–87, 2001.

[106] E. D. Palik and G. Ghosh, *Handbook of optical constants of solids.* San Diego: Academic Press, 1998.

[107] G. T. Reed, *Silicon photonics : the state of the art.* Chichester: John Wiley and Sons, 2008.

[108] R. Hui and M. S. O'Sullivan, *Fiber optic measurement techniques.* Amsterdam ; London: Elsevier/Academic Press, 2009.

[109] L. Liao, D. R. Lim, A. M. Agarwal, X. M. Duan, K. K. Lee, and L. C. Kimerling, "Optical transmission losses in polycrystalline silicon strip waveguides: Effects of waveguide dimensions, thermal treatment, hydrogen passivation, and wavelength," *Journal of Electronic Materials*, vol. 29, no. 12, pp. 1380–1386, 2000.

[110] D. K. Sparacin, *Process and design techniques for low loss integrated silicon photonics.* Ph d, 2006.

[111] R. K. Willardson and A. C. Beer, *Semiconductors and semimetals*, vol. 21. Academic Press, 1966.

[112] A. Harke, M. Krause, and J. Mueller, "Low-loss singlemode amorphous silicon waveguides," *Electronics Letters*, vol. 41, no. 25, pp. 1377–1379, 2005.

[113] S. Y. Zhu, G. Q. Lo, and D. L. Kwong, "Low-loss amorphous silicon wire waveguide for integrated photonics: effect of fabrication process and the thermal stability," *Optics Express*, vol. 18, no. 24, pp. 25283–25291, 2010.

[114] A. Neogi and Z. M. Wang, *Nanoscale photonics and optoelectronics.* Lecture notes in nanoscale science and technology, New York: Springer Science, 2010.

[115] G. He and S. H. Liu, *Physics of nonlinear optics.* Singapore: World Scientific, 1999.

[116] Q. Lin, J. Zhang, G. Piredda, R. W. Boyd, P. M. Fauchet, and G. P. Agrawal, "Dispersion of silicon nonlinearities in the near infrared region," *Applied Physics Letters*, vol. 91, no. 2, 2007.

[117] S. Pearl, N. Rotenberg, and H. M. van Driel, "Three photon absorption in silicon for 2300-3300 nm," *Applied Physics Letters*, vol. 93, no. 13, 2008.

[118] A. J. McEvoy, T. Markvart, and L. Castaer, *Practical handbook of photovoltaics : fundamentals and applications.* Waltham, MA: Academic Press, 2nd ed., 2012.

[119] S. J. Fonash, *Solar cell device physics.* Burlington, MA: Academic Press, 2nd ed., 2010.

[120] S. K. Sundaram and E. Mazur, "Inducing and probing non-thermal transitions in semiconductors using femtosecond laser pulses," *Nature Materials*, vol. 1, no. 4, pp. 217–224, 2002.

[121] L. A. Coldren, S. W. Corzine, and M. Mashanovitch, *Diode lasers and photonic integrated circuits.* Wiley series in microwave and optical engineering, Hoboken, N.J.: Wiley, 2nd ed., 2012.

[122] D. J. Won, M. O. Ramirez, H. Kang, V. Gopalan, N. F. Baril, J. Calkins, J. V. Badding, and P. J. A. Sazio, "All-optical modulation of laser light in amorphous silicon-filled microstructured optical fibers," *Applied Physics Letters*, vol. 91, no. 16, 2007.

[123] M. J. Weber, *Handbook of optical materials.* The CRC Press laser and optical science and technology series, Boca Raton, Flor.: CRC Press, 2003.

[124] T. K. Liang, L. R. Nunes, T. Sakamoto, K. Sasagawa, T. Kawanishi, M. Tsuchiya, G. R. A. Priem, D. Van Thourhout, P. Dumon, R. Baets, and H. K. Tsang, "Ultrafast all-optical switching by cross-absorption modulation in silicon wire waveguides," *Optics Express*, vol. 13, no. 19, pp. 7298–7303, 2005.

[125] MathWorks, *Curve fitting toolbox 1: users guide.* Natick, MA., 2006.

[126] K. Narayanan and S. F. Preble, "Optical nonlinearities in hydrogenated-amorphous silicon waveguides," *Optics Express*, vol. 18, no. 9, pp. 8998–9005, 2010.

[127] B. Kuyken, H. Ji, S. Clemmen, S. K. Selvaraja, H. Hu, M. Pu, M. Galili, P. Jeppesen, G. Morthier, S. Massar, L. K. Oxenlowe, G. Roelkens, and R. Baets, "Nonlinear properties of and nonlinear processing in hydrogenated amorphous silicon waveguides," *Optics Express*, vol. 19, no. 26, pp. 146–153, 2011.

[128] C. Grillet, L. Carletti, C. Monat, P. Grosse, B. Ben Bakir, S. Menezo, J. M. Fedeli, and D. J. Moss, "Amorphous silicon nanowires combining high nonlinearity, fom and optical stability," *Optics Express*, vol. 20, no. 20, pp. 22609–22615, 2012.

[129] H. K. Tsang, C. S. Wong, T. K. Liang, I. E. Day, S. W. Roberts, A. Harpin, J. Drake, and M. Asghari, "Optical dispersion, two-photon absorption and self-phase modulation in silicon waveguides at 1.5um wavelength," *Applied Physics Letters*, vol. 80, no. 3, pp. 416–418, 2002.

[130] G. W. Rieger, K. S. Virk, and J. F. Young, "Nonlinear propagation of ultrafast 1.5um pulses in high-index-contrast silicon-on-insulator waveguides," *Applied Physics Letters*, vol. 84, no. 6, pp. 900–902, 2004.

[131] P. Dumon, G. Priem, L. R. Nunes, W. Bogaerts, D. Van Thourhout, P. Bienstman, T. K. Liang, M. Tsuchiya, P. Jaenen, S. Beckx, J. Wouters, and R. Baets, "Linear and nonlinear nanophotonic devices based on silicon-on-insulator wire waveguides," *Japanese Journal of Applied Physics Part 1-Regular Papers Brief Communications and Review Papers*, vol. 45, no. 8B, pp. 6589–6602, 2006.

[132] G. T. Reed, G. Mashanovich, F. Y. Gardes, and D. J. Thomson, "Silicon optical modulators," *Nature Photonics*, vol. 4, no. 8, pp. 518–526, 2010.

[133] H. K. Tsang, P. A. Snow, I. E. Day, I. H. White, R. V. Penty, R. S. Grant, Z. Su, G. T. Kennedy, and W. Sibbett, "All-optical modulation with ultrafast recovery at low pump energies in passive ingaas/ingaasp multiquantum well wave-guides," *Applied Physics Letters*, vol. 62, no. 13, pp. 1451–1453, 1993.

[134] K. L. Hall, G. Lenz, E. P. Ippen, and G. Raybon, “Heterodyne pump probe technique for time-domain studies of optical nonlinearities in wave-guides,” *Optics Letters*, vol. 17, no. 12, pp. 874–876, 1992.

[135] A. D. McNaught, A. Wilkinson, I. U. of Pure, and A. Chemistry, *IUPAC compendium of chemical terminology.* Great Britain: Royal Society of Chemistry, 2000.

[136] N. Bloembergen, “Nonlinear optics: Past, present, and future,” *Ieee Journal of Selected Topics in Quantum Electronics*, vol. 6, no. 6, pp. 876–880, 2000.

[137] N. Bloembergen, “Nonlinear optics and spectroscopy,” *Resonances : A Volume in Honor of the 70th Birthday of Nicolaas Bloembergen*, pp. 471–499, 1990.

[138] R. Paschotta, *Field guide to laser pulse generation.* SPIE field guides, Bellingham, Wash.: SPIE Press, 2008.

[139] Y. Shoji, T. Ogasawara, T. Kamei, Y. Sakakibara, S. Suda, K. Kintaka, H. Kawashima, M. Okano, T. Hasama, H. Ishikawa, and M. Mori, “Ultrafast nonlinear effects in hydrogenated amorphous silicon wire waveguide,” *Optics Express*, vol. 18, no. 6, pp. 5668–5673, 2010.

[140] K. Narayanan, A. W. Elshaari, and S. F. Preble, “Broadband all-optical modulation in hydrogenated-amorphous silicon waveguides,” *Optics Express*, vol. 18, no. 10, pp. 9809–9814, 2010.

[141] M. Sheikbahae, J. Wang, and E. W. Van Stryland, “Nondegenerate optical kerr-effect in semiconductors,” *Ieee Journal of Quantum Electronics*, vol. 30, no. 2, pp. 249–255, 1994.

[142] P. Mehta, N. Healy, R. Slavik, R. T. Watts, J. R. Sparks, T. D. Day, P. J. A. Sazio, J. V. Badding, and A. C. Peacock, “Nonlinearities in silicon optical fibers,” *Optical Fiber Communication Conference and Exposition (OFC/NFOEC) and the National Fiber Optic Engineers Conference*, 2011.

[143] R. Dekker, N. Usechak, M. Forst, and A. Driessen, “Ultrafast nonlinear all-optical processes in silicon-on-insulator waveguides,” *Journal of Physics D-Applied Physics*, vol. 40, no. 14, pp. R249–R271, 2007.

[144] E. Dulkeith, Y. A. Vlasov, X. G. Chen, N. C. Panoiu, and R. M. Osgood, “Self-phase-modulation in submicron silicon-on-insulator photonic wires,” *Optics Express*, vol. 14, no. 12, pp. 5524–5534, 2006.

[145] M. Dinu, “Dispersion of phonon-assisted nonresonant third-order nonlinearities,” *Ieee Journal of Quantum Electronics*, vol. 39, no. 11, pp. 1498–1503, 2003.

[146] I. Turek and I. Martincek, “Interference of modes in optical fibers,” *Optical Engineering*, vol. 39, no. 5, pp. 1304–1309, 2000.

[147] F. Poletti and P. Horak, “Dynamics of femtosecond supercontinuum generation in multimode fibers,” *Optics Express*, vol. 17, no. 8, pp. 6134–6147, 2009.

[148] P. Horak and F. Poletti, *Multimode Nonlinear Fibre Optics: Theory and Applications*, vol. 1 of *Recent Progress in Optical Fiber Research.* InTech, 2012.

[149] X. P. Liu, J. B. Driscoll, J. I. Dadap, R. M. Osgood, S. Assefa, Y. A. Vlasov, and W. M. J. Green, “Self-phase modulation and nonlinear loss in silicon nanophotonic wires near the mid-infrared two-photon absorption edge,” *Optics Express*, vol. 19, no. 8, pp. 7778–7789, 2011.

[150] P. V. Mamyshev, “All-optical data regeneration based on self-phase modulation effect,” *24th European Conference on Optical Communication, Vol 1-3*, pp. 475–476, 1998.

[151] L. B. Fu, M. Rochette, V. G. Ta’eed, D. J. Moss, and B. J. Eggleton, “Investigation of self-phase modulation based optical regeneration in single mode as2se3 chalcogenide glass fiber,” *Optics Express*, vol. 13, no. 19, pp. 7637–7644, 2005.

[152] B. K. Nayar, N. Finlayson, N. J. Doran, S. T. Davey, D. L. Williams, and J. W. Arkwright, “All-optical switching in a 200-m twin-core fiber nonlinear mach-zehnder interferometer,” *Optics Letters*, vol. 16, no. 6, pp. 408–410, 1991.

[153] C. H. Kwok, S. H. Lee, K. K. Chow, and C. Lin, “Photonic crystal fibre based all-optical modulation format conversions between nrz and rz with hybrid clock recovery from a prz signal,” *Iet Optoelectronics*, vol. 1, no. 1, pp. 47–53, 2007.

[154] A. Boskovic, S. V. Chernikov, J. R. Taylor, L. GrunerNielsen, and O. A. Levring, “Direct continuous-wave measurement of n2 in various types of telecommunication fiber at 1.55um,” *Optics Letters*, vol. 21, no. 24, pp. 1966–1968, 1996.

[155] M. Artiglia, E. Ciaramella, and B. Sordo, “Using modulation instability to determine kerr coefficient in optical fibers,” *Electronics Letters*, vol. 31, no. 12, pp. 1012–1013, 1995.

[156] T. Kato, Y. Suetsugu, M. Takagi, E. Sasaoka, and M. Nishimura, “Measurement of the nonlinear refractive-index in optical-fiber by the cross-phase-modulation method with depolarized pump light,” *Optics Letters*, vol. 20, no. 9, pp. 988–990, 1995.

[157] A. C. Peacock, P. Mehta, P. Horak, and N. Healy, “Nonlinear pulse dynamics in multimode silicon core optical fibers,” *Optics Letters*, vol. 37, no. 16, pp. 3351–3353, 2012.

[158] O. Boyraz, P. Koonath, V. Raghunathan, and B. Jalali, “All optical switching and continuum generation in silicon waveguides,” *Optics Express*, vol. 12, no. 17, pp. 4094–4102, 2004.

[159] P. Koonath, D. R. Solli, and B. Jalali, “Limiting nature of continuum generation in silicon,” *Applied Physics Letters*, vol. 93, no. 9, 2008.

[160] S. R. Friberg and P. W. Smith, “Nonlinear optical-glasses for ultrafast optical switches,” *Ieee Journal of Quantum Electronics*, vol. 23, no. 12, pp. 2089–2094, 1987.

[161] P. D. Townsend, G. L. Baker, N. E. Schlotter, C. F. Klausner, and S. Etemad, “Waveguiding in spun films of soluble polydiacetylenes,” *Applied Physics Letters*, vol. 53, no. 19, pp. 1782–1784, 1988.

[162] G. I. Stegeman, C. T. Seaton, and R. Zanoni, “Organic films in nonlinear integrated-optics structures,” *Thin Solid Films*, vol. 152, no. 1-2, pp. 231–263, 1987.

[163] K. W. Delong, K. B. Rochford, and G. I. Stegeman, “Effect of 2-photon absorption on all-optical guided-wave devices,” *Applied Physics Letters*, vol. 55, no. 18, pp. 1823–1825, 1989.

[164] H. K. Tsang and Y. Liu, “Nonlinear optical properties of silicon waveguides,” *Semiconductor Science and Technology*, vol. 23, no. 6, 2008.

[165] C. Koos, L. Jacome, C. Poulton, J. Leuthold, and W. Freude, “Nonlinear silicon-on-insulator waveguides for all-optical signal processing,” *Optics Express*, vol. 15, no. 10, pp. 5976–5990, 2007.

[166] S. Zlatanovic, J. S. Park, S. Moro, J. M. C. Boggio, I. B. Divliansky, N. Alic, S. Mookherjea, and S. Radic, “Mid-infrared wavelength conversion in silicon waveguides using ultracompact telecom-band-derived pump source,” *Nature Photonics*, vol. 4, no. 8, pp. 561–564, 2010.

[167] V. G. Ta’eed, N. J. Baker, L. B. Fu, K. Finsterbusch, M. R. E. Lamont, D. J. Moss, H. C. Nguyen, B. J. Eggleton, D. Y. Choi, S. Madden, and B. Luther-Davies, “Ultrafast all-optical chalcogenide glass photonic circuits,” *Optics Express*, vol. 15, no. 15, pp. 9205–9221, 2007.

[168] M. Dinu, F. Quochi, and H. Garcia, “Third-order nonlinearities in silicon at telecom wavelengths,” *Applied Physics Letters*, vol. 82, no. 18, pp. 2954–2956, 2003.

[169] J. M. Harbold, F. O. Ilday, F. W. Wise, J. S. Sanghera, V. Q. Nguyen, L. B. Shaw, and I. D. Aggarwal, “Highly nonlinear as-s-se glasses for all-optical switching,” *Optics Letters*, vol. 27, no. 2, pp. 119–121, 2002.

[170] K. Suzuki, Y. Hamachi, and T. Baba, “Fabrication and characterization of chalcogenide glass photonic crystal waveguides,” *Optics Express*, vol. 17, no. 25, pp. 22393–22400, 2009.

[171] R. Dekker, A. Driessen, T. Wahlbrink, C. Moormann, J. Niehusmann, and M. Forst, "Ultrafast kerr-induced all-optical wavelength conversion in silicon waveguides using 1.55um femtosecond pulses," *Optics Express*, vol. 14, no. 18, pp. 8336–8346, 2006.

[172] E. K. Tien, X. Z. Sang, F. Qing, Q. Song, and O. Boyraz, "Ultrafast pulse characterization using cross phase modulation in silicon," *Applied Physics Letters*, vol. 95, no. 5, 2009.

[173] H. S. Hsieh, K. M. Feng, and M. C. M. Lee, "Study of cross-phase modulation and free-carrier dispersion in silicon photonic wires for mamyshev signal regenerators," *Optics Express*, vol. 18, no. 9, pp. 9613–9621, 2010.

[174] I. W. Hsieh, X. G. Chen, J. I. Dadap, N. C. Panoiu, R. M. Osgood, S. J. Mcnab, and Y. A. Vlasov, "Cross-phase modulation-induced spectral and temporal effects on co-propagating femtosecond pulses in silicon photonic wires," *Optics Express*, vol. 15, no. 3, pp. 1135–1146, 2007.

[175] T. D. Vo, B. Corcoran, J. Schroder, M. D. Pelusi, D. X. Xu, A. Densmore, R. B. Ma, S. Janz, D. J. Moss, and B. J. Eggleton, "Silicon-chip-based real-time dispersion monitoring for 640 gbit/s dpsk signals," *Journal of Lightwave Technology*, vol. 29, no. 12, pp. 1790–1796, 2011.

[176] J. B. Driscoll, W. Astar, X. Liu, J. I. Dadap, W. M. J. Green, Y. A. Vlasov, G. M. Carter, and R. M. Osgood, "All-optical wavelength conversion of 10 gb/s rz-ook data in a silicon nanowire via cross-phase modulation: Experiment and theoretical investigation," *Ieee Journal of Selected Topics in Quantum Electronics*, vol. 16, no. 5, pp. 1448–1459, 2010.

[177] H. H. Li, "Refractive-index of silicon and germanium and its wavelength and temperature derivatives," *Journal of Physical and Chemical Reference Data*, vol. 9, no. 3, pp. 561–658, 1980.

[178] G. P. Agrawal, *Applications of nonlinear fiber optics.* Elsevier, 2nd ed., 2008.

[179] "Simply silicon," *Nature Photonics*, vol. 4, no. 8, pp. 491–491, 2010.

[180] R. Soref, "Mid-infrared photonics in silicon and germanium," *Nature Photonics*, vol. 4, no. 8, pp. 495–497, 2010.

[181] I. D. Aggarwal and G. Lu, *Fluoride glass fiber optics.* Boston: Academic Press, 1991.

[182] X. P. Liu, R. M. Osgood, Y. A. Vlasov, and W. M. J. Green, "Mid-infrared optical parametric amplifier using silicon nanophotonic waveguides," *Nature Photonics*, vol. 4, no. 8, pp. 557–560, 2010.

[183] T. H. Allik and S. Chandra, “Recent advances in continuously tunable 8-12 mu m radiation using optical parametric oscillators,” *Electro-Optical Technology for Remote Chemical Detection and Identification Ii*, vol. 3082, pp. 54–64, 1997.

[184] V. Raghunathan, R. Shori, O. M. Stafsudd, and B. Jalali, “Nonlinear absorption in silicon and the prospects of mid-infrared silicon Raman lasers,” *Physica Status Solidi a-Applications and Materials Science*, vol. 203, no. 5, pp. R38–R40, 2006.

[185] N. K. Hon, R. Soref, and B. Jalali, “The third-order nonlinear optical coefficients of si, ge, and si1-xgex in the midwave and longwave infrared,” *Journal of Applied Physics*, vol. 110, no. 1, 2011.

[186] L. Palfalvi, B. C. Toth, G. Almasi, J. A. Fulop, and J. Hebling, “A general z-scan theory,” *Applied Physics B-Lasers and Optics*, vol. 97, no. 3, pp. 679–685, 2009.

[187] A. Schliesser, N. Picque, and T. W. Hansch, “Mid-infrared frequency combs,” *Nature Photonics*, vol. 6, no. 7, pp. 440–449, 2012.

[188] A. F. Gibson, C. B. Hatch, P. N. D. Maggs, D. R. Tilley, and A. C. Walker, “2-photon absorption in indium-antimonide and germanium,” *Journal of Physics C-Solid State Physics*, vol. 9, no. 17, pp. 3259–3275, 1976.

[189] J. J. Wynne, “Optical third-order mixing in gaas, ge, si, and inas,” *Physical Review*, vol. 178, no. 3, pp. 1295–1303, 1969.

[190] M. Sheikbahae, D. C. Hutchings, D. J. Hagan, and E. W. Van Stryland, “Dispersion of bound electronic nonlinear refraction in solids,” *Ieee Journal of Quantum Electronics*, vol. 27, no. 6, pp. 1296–1309, 1991.

[191] D. E. Watkins, C. R. Phipps, and S. J. Thomas, “Determination of the 3rd-order non-linear optical coefficients of germanium through ellipse rotation,” *Optics Letters*, vol. 5, no. 6, pp. 248–249, 1980.

[192] R. A. Soref, S. J. Emelett, and A. R. Buchwald, “Silicon waveguided components for the long-wave infrared region,” *Journal of Optics a-Pure and Applied Optics*, vol. 8, no. 10, pp. 840–848, 2006.

[193] T. L. Cottrell, *The strengths of chemical bonds.* New York,: Academic Press, 1954.

[194] D. Bermejo and M. Cardona, “Infrared-absorption in hydrogenated amorphous and crystallized germanium,” *Journal of Non-Crystalline Solids*, vol. 32, no. 1-3, pp. 421–430, 1979.

[195] D. Bermejo and M. Cardona, “Raman-scattering in pure and hydrogenated amorphous-germanium and silicon,” *Journal of Non-Crystalline Solids*, vol. 32, no. 1-3, pp. 405–419, 1979.

[196] D. Rank, H. E. Bennett, and D. C. Cronemeyer, “The index of refraction of germanium measured by an interference method,” *J. Opt. Soc. Am*, vol. 44, no. 1, pp. 13–16, 1954.

[197] J. C. Stover, *Optical scattering : measurement and analysis.* Bellingham, Wash.: SPIE Press, 3rd ed., 2012.

[198] L. Shen, N. Healy, P. Mehta, T. D. Day, J. R. Sparks, J. V. Badding, and A. C. Peacock, “Transmission properties of hydrogenated amorphous silicon optical fibers into the mid-infrared regime,” *FiO/LS XXVIII*, vol. FM3H.3, 2012.

[199] C. M. Cirloganu, L. A. Padilha, D. A. Fishman, S. Webster, D. J. Hagan, and E. W. Van Stryland, “Extremely nondegenerate two-photon absorption in direct-gap semiconductors [invited],” *Optics Express*, vol. 19, no. 23, pp. 22951–22960, 2011.

[200] M. Rumi and J. W. Perry, “Two-photon absorption: an overview of measurements and principles,” *Adv. Opt. Photon*, vol. 2, no. 4, pp. 451–518, 2010.